5-2021

Developing a Novel Neutron Spectrometer Using the Inverse Bonner Sphere Concept for International Safeguards

Mara Watson
Clemson University, marawtsn@gmail.com

Developing a Novel Neutron Spectrometer Using the Inverse Bonner Sphere Concept for International Safeguards

---

A Dissertation
Presented to
the Graduate School of
Clemson University

In Partial Fulfillment
of the Requirements for the Degree
Doctor of Philosophy
Environmental Engineering and Earth Sciences

---

by
Mara Mae Watson
May 2021

Accepted by:
Dr. Timothy A. DeVol, Committee Chair
Dr. Ramkumar Venkataraman
Dr. Nicole E. Martinez
Dr. Glenn A. Fugate

Abstract

Accurate neutron measurements in international safeguards are dependent on the knowledge of significant sources of neutrons emitted in an item, which can include neutrons from induced or spontaneous fission and (α, n) reactions. In particular, the neutron energy spectrum is needed to accurately characterize the detector response to neutrons of a range of energies. Neutron energy spectra for neutron emitters in international safeguards are typically not well-established, particularly for (α, n) reactions. A novel neutron spectrometer using the inverse Bonner sphere concept was developed in this work to experimentally establish neutron energy spectra for international safeguards purposes. Well-characterized neutron sources, namely ^{252}Cf, were heavily relied upon in this work. However, discrepancies in the fissioning characteristics between ^{252}Cf sources were discovered that needed to be addressed prior to developing the novel neutron spectrometer. Gamma-ray signatures from spontaneous fission products and odd-numbered Cf isotopes present in the ^{252}Cf spectrum were used to confirm or query source age and isotopic ratios for five ^{252}Cf sources. MCNP simulations were then employed for proof-of-concept of the inverse Bonner sphere spectrometer (iBSS) and sensitivity analyses to the response functions and *a priori* information in the input guess spectrum. Application of the iBSS was then presented as a tool for experimentally verifying neutron energy spectra in SOURCES-4C.

Dedication

To all of the women in science and engineering who paved the way for me to exist and thrive in the modern day scientific community.

Acknowledgments

Many heartfelt thanks are due to numerous people for assisting me on this journey to earn the doctoral degree. Because of limited space, however, the highlights are included here.

First and foremost I have to thank my university advisor, Dr. Timothy A. DeVol, for his academic guidance and encouragement throughout this long and trying process. His seemingly unending patience allowed me to excel when I was ready and take my time when I wasn't. I am also indebted to Tim for the numerous recommendation letters that he wrote for scholarships and fellowships that ultimately provided opportunities that paved the way for my academic success. Most importantly, I am thankful for the connection with Ram that set me on my current career path in international safeguards. Ultimately, none of this would have been possible without him.

My primary ORNL mentor, Dr. Ramkumar Venkataraman, is also owed a massive thank you—complete with confetti and balloons—for taking me in as a student, even though it was not within his job description to do so, so that I could experience research at a national lab and work with some of the greatest minds in international safeguards. Not only have his wisdom and guidance been pivotal in completing my degree, but the knowledge that I have gained has best prepared me for a successful career in international safeguards.

I also have to thank my committee members, Dr. Nicole E. Martinez and Dr. Glenn A. Fugate, for their willingness to participate in this journey and for their helpful suggestions to improve my work.

Thank you to the Safeguards and Security Technology group at Oak Ridge National Laboratory for hosting and welcoming me into your group as a graduate student. I thoroughly enjoyed my time working and chatting with each of you and look forward to future collaborations. I specifically need to thank Susan Smith for being a good friend and offering professional guidance when I needed it most. I also have to thank Dr. Stephen Croft and Dr. Robert D. McElroy for passing along their knowledge and, along with Dr. Andrea Favalli, providing the idea and groundwork for my dissertation topic.

My friends—Victoria, Andrea, and Lisa—have provided an ear for listening and a shoulder to cry on more times than I can count. I am so thankful to have each of you in my life. I could not have made it through this entire 5 year journey without all of your support. I cannot wait to see where all of our paths lead us now that we're past the doctoral program.

Dr. Eugene Wu, a dear family friend, provided support and encouragement on this journey always when I needed it most. I would not have gotten through all of my education without it.

Of course, my parents—Leesa Doster and Rick Thomas—deserve the biggest thanks of them all that I will never be able to repay. They have supported me (and continue to do so) through every single crazy endeavor I dream up without questions (well, they do ask some questions to keep me in check). These two people are my rocks and I could not imagine my life without them. Thank you for always believing in me y'all.

This research was performed under appointment to the Nuclear Nonprolifera-

tion International Safeguards Fellowship Program sponsored by the National Nuclear Security Administration's Office of International Nuclear Safeguards (NA-241).

Table of Contents

List of Tables

List of Figures

Chapter 1

Introduction

The International Atomic Energy Agency (IAEA) is an autonomous international organization that promotes the safe, secure, and peaceful use of nuclear energy. The IAEA is tasked with assuring the international community that Member States are upholding their legal obligations to international nuclear treaties, particularly the Nonproliferation Treaty (NPT) [5] and Additional Protocol (AP) [6], by confirming the presence of all declared special nuclear material (SNM) and/or the absence of undeclared SNM and illicit activities through international safeguards. International safeguards are technical measures the IAEA employs to independently verify State compliance to the NPT and to deter illicit activities to divert nuclear material throughout the nuclear fuel cycle for non-peaceful purposes [7]. Neutron counting is an established nondestructive assay (NDA) method employed by the IAEA to measure the mass of SNM in an item without changing the physical or chemical properties of the material [7]. Neutron measurements can be performed in a nuclear facility, such as a uranium enrichment facility, by an IAEA inspector without bringing a sample to a laboratory for analysis and quantification. For accurate neutron measurements, it is important to have knowledge of the significant sources of neutrons emitted from

an item, which can include neutrons from induced fission, spontaneous fission, and the (α, n) reaction. Each of these neutron sources are defined in Chapter 2.

SOURCES-4C is a computer code that generates neutron energy spectra for complex source compositions that emit spontaneous fission neutrons, delayed neutrons, and (α,n) neutrons [8, 9]. In international safeguards, SOURCES-4C is most commonly used to generate neutron energy spectra for MCNP simulations of neutron measurements for verifying declared content in enriched U storage cylinders or spent nuclear fuel. However, neutron energy spectra for (α, n) reactions important to international safeguards are not well known in many cases. An example of this is the AmLi (α, n) neutron energy spectrum, which is often debated in the literature, used to model active coincidence counting measurements.

Active neutron coincidence counting is an established non-destructive assay (NDA) method implemented by the IAEA to measure the mass of ^{235}U in an item [7]. AmLi neutron sources induce fission in ^{235}U and the resulting number of fissions registered by the neutron counter is related to the mass of ^{235}U via a system calibration. Although a system calibration has traditionally been based on the response to representative standards, simulation-based system calibrations are becoming more commonplace in international safeguards due to the difficulty of obtaining representative standards for complex geometries, such as a fuel assembly. However, biases may be introduced into the system when deriving the system calibration in this manner. An ongoing debate in the literature exists regarding an accurate representation of the neutron spectrum for AmLi [2, 3, 10–12]. Moreover, discrepancies exist between the AmLi (α, n) spectrum in SOURCES-4C and the literature [11]. A method is needed to establish an accepted neutron energy spectrum not only for the AmLi (α, n) reaction, but for other (α, n) reactions pertinent to international safeguards.

The novel inverse Bonner sphere spectrometer (iBSS) was developed to ex-

perimentally calculate neutron energy spectra from a series of measurements. The inverse Bonner sphere concept was initially proposed for a sensitivity study for AmLi sources using a large volume active well coincidence counter (LVAWCC) [13]. The standard Bonner sphere spectrometer (BSS) calculated the neutron energy spectrum from a series of measurements by placing a single thermal neutron sensor centrally inside of spherical moderators with increasing diameters to elicit a different response function with respect to energy [14]. In contrast, the inverse Bonner sphere placed the source in spherical or cylindrical moderators with incrementally increasing diameters and surrounded the source and moderator by two concentric rings of moderated ^{3}He proportional counters. Each ring consisted of 24 moderated ^{3}He proportional counters and acted as a single detector. The inverse Bonner sphere thus consisted of two rings of counters compared to the single neutron sensor of the BSS, providing twice as many data points for unfolding the neutron energy spectrum for the same number of moderators. Previous work considered which AmLi neutron energy spectrum reported in the literature most closely resembled the experimental data, but did not perform neutron energy spectrum unfolding [13]. This work presents the process of developing a novel neutron spectrometer using the inverse Bonner sphere concept for calculating the neutron energy spectrum from a series of neutron measurements for safeguards-relevant neutron emitters. Verification of (α, n) neutron energy spectra in SOURCES-4C is demonstrated as an application of the iBSS.

Chapter 2

Background

2.1 Properties of the Neutron

Neutrons ($m_n = 1.674 \cdot 10^{-27}$ kg [15]) are neutrally-charged subatomic particles with a similar, but slightly heavier, mass than the positively-charged proton ($m_p = 1.672 \cdot 10^{-27}$ kg [15]). They are typically found bound in the nucleus, but can be emitted from the nucleus as neutron radiation, which presents as free neutrons. Free neutrons ($T_{1/2} = 613.9$ s) are unstable and decay to form a proton and electron [16, 17]. However, the free neutron, referred to hereafter simply as the neutron, is treated as long-lived and stable in neutron counting for international safeguards, because only the time frame of 1-s or less is considered post-emission.

2.2 Sources of Neutron Radiation in International Safeguards

The sources of neutron radiation are diverse and those of interest are dependent on the field of application. For international safeguards, the primary sources

of neutron radiation are prompt and delayed neutrons from induced or spontaneous fission, the (α, n) reaction, and background neutron radiation.

Fission occurs when a nucleus breaks into multiple fragments—typically two smaller nuclei and two or more free neutrons—and releases energy in the form of heat or γ rays [18]. Heavy nuclei are particularly subject to fission, because the long range Coulomb repulsion from the protons increases faster ($\propto Z^2$) than short range nuclear forces holding the nucleus together ($\propto A$), causing instability in the nucleus [19]. Fission can be either a spontaneous or an induced nuclear reaction. Both spontaneous and induced fission produce a similar end result, but are differentiated by how each event is initiated. Spontaneous fission occurs when an unstable nucleus splits apart randomly and spontaneously. This phenomenon most commonly occurs in even-even isotopes—isotopes with even numbers of protons and neutrons. The even-even isotopes with high spontaneous fission yields important in international safeguards are ^{238}U, ^{238}Pu, ^{240}Pu, ^{242}Pu, ^{242}Cm, ^{244}Cm, and ^{252}Cf [20]. Induced fission, on the other hand, occurs when the nucleus absorbs a particle or photon that excites it to an unstable state, causing it to break apart [18]. Typically, a free neutron is absorbed by the nucleus, which subsequently becomes unstable and causes the nucleus to fission. Uranium-235 has an induced fission signature that is commonly used to measure the fissile mass in an item via neutron counting in international safeguards [20]. For the purposes of this discussion, a signature is defined as a unique emission or distribution of possible specific reactions from an isotope that can be used to identify the presence of the isotope the radiation was emitted from.

Neutrons released from a fission event can be prompt or delayed in origin. Prompt fission neutrons are emitted during the fission event when the parent nucleus breaks into fragments. Delayed fission neutrons are emitted following beta decay of a neutron-rich fission product [21]. Both prompt and delayed fission neutrons are used

as signatures for identifying and quantifying special nuclear material for international safeguards.

The (α, n) reaction occurs in the nuclear fuel cycle when an α-emitting actinide is in intimate contact with a light element (Z<18) [9]. The α particle is emitted via α decay from the actinide and absorbed by the light element, which subsequently emits a single neutron. This reaction is dependent on a radioisotope decaying via α particle emission, the stopping power of the α particle within the medium, and the microscopic cross section [9]. The neutron yield and neutron energy spectrum emitted of the (α, n) reaction is also of interest to improve modeling and simulation capabilities. This reaction appears throughout the fuel cycle as both an extraneous neutron source term during neutron counting, such as measuring the mass of Pu, and the dominant neutron source term, such as measuring the mass of ^{235}U. The mass of even-numbered Pu isotopes—namely ^{238}Pu, ^{240}Pu, and ^{242}Pu—can be measured by relating the number of fissions detected to the mass of the item via a calibration curve using passive neutron coincidence counting, which measures the fission rate using shift register electronics [22]. However, if the material is PuO_2, then the additional neutrons from the ^{17,18}O(α, n) reaction can induce fission in ^{239}Pu, causing additional fissions to be detected and an over estimate the mass of even-numbered Pu isotopes in an item [20]. In the case of enriched UF_6, the dominant neutron emitter is from the $^{234}UF_6$ (α, n) reaction [23]. The mass of ^{235}U in the item can be related to the total neutrons emitted from the $^{234}UF_6$ (α, n) reaction as long as the isotopic ratio is known or measured by gamma-ray spectroscopy [20].

A source of ambient neutron radiation is from cosmic ray interaction by nuclei in the atmosphere, earth, or large structures subsequently followed by free neutron emission into the surrounding environment. Cosmic rays originate from celestial objects, such as the sun or stars, and consist of 90% protons, 9% helium nuclei, and

1% other heavy elements at the top of the atmosphere [24, 25]. Because cosmic rays lose energy as they penetrate the atmosphere, the neutron background rate is larger at higher elevations compared to sea level and must be accounted for when collecting neutron measurements. Cosmic rays are also affected by the Earth's magnetic field, so the neutron background rate can also vary with latitude when moving from the equator to the poles. Solar flares can also cause a spike in the neutron background rate, so regular neutron background measurements should be conducted throughout a measurement campaign to ensure the neutron background rate remains steady [24].

2.3 Neutron Interactions with Matter

Neutrons are indirectly ionizing radiation and rely on secondary reactions for detection [26]. The probability of a particular reaction occurring between a neutron and a nucleus in the target material is represented by the microscopic cross section, hereafter referred to simply as the cross section. The cross section is the ratio of the reaction rate, R [atoms/cm^2·s], of a particular reaction to the intensity of a beam of neutrons at a given neutron energy, I [neutrons/cm^2·s], incident on a thin target with an areal density, N_A [atoms/cm^2] [18, 26]. Mathematically, this is represented as

$$\sigma = \frac{R}{N_A \cdot I} \tag{2.1}$$

with units of area [cm^2]. The cross section is usually expressed in units of barns [b], where

$$1\text{b} = 10^{-24}\text{cm}^2,$$

so that the cross section can be related to the geometrical area of the target nuclei. However, the cross section does not directly correspond to the geometrical area of the

target nuclei. Resonance effects as a result of the quantum mechanical nature of the neutron and nucleus can cause the cross section to be greater than or less than the geometrical cross sectional area of the nucleus [18].

The concept of the cross section can be applied to a diverse set of neutron-induced reactions, which are typically categorized according to Fig. 2.1 [18]. The total cross section, σ_T, represents the probability of all neutron-induced reactions occurring when a neutron is incident upon a specific nuclide. The next tier in the cross section hierarchy is comprised of scatter and absorption events. These two subtypes add together to form the total cross section, such that

$$\sigma_T(E) = \sigma_s(E) + \sigma_a(E) \tag{2.2}$$

where σ_s is the scattering cross section and σ_a is the absorption cross section [18].

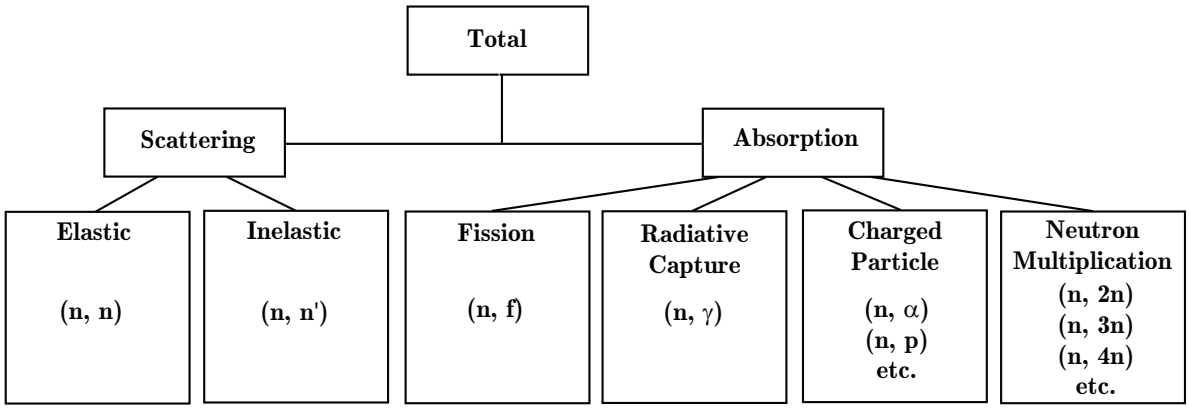

Figure 2.1: Neutron-induced reactions by category

Scatter events occur when a neutron collides with a nucleus and changes veloc-

ity but is not absorbed into the nucleus [18]. The scattering cross section has elastic and inelastic components such that

$$\sigma_s(E) = \sigma_{el}(E) + \sigma_i(E) \tag{2.3}$$

where σ_{el} is the elastic scattering cross section and σ_i is the inelastic scattering cross section. In an elastic scattering event, a fraction of the neutron's kinetic energy is transferred to the nucleus, but momentum is conserved in the system. In an inelastic scattering event, the energy transferred from the neutron during the collision causes the nucleus to enter an excited state and eventually releases radiation. Although momentum is conserved in an inelastic scattering event, the kinetic energy in the system cannot be tracked as it is converted to other types of energy during the collision [18].

Absorption events occur when a neutron collides and merges with a nucleus to form a heavier, and frequently unstable, compound nucleus [18]. Absorption events can induce fission or result in prompt emission of γ rays, charged particles, or additional neutrons. The absorption cross section is comprised of all neutron-induced absorption reactions, such as fission, and can be described mathematically as

$$\sigma_a(E) = \sigma_f(E) + \sigma_{n,\gamma}(E) + \sigma_{cp}(E) + \sigma_{n,xn}(E) \tag{2.4}$$

where σ_f is the fission cross section, $\sigma_{n,\gamma}$ is the radiative capture cross section, σ_{cp} is the charged particle reaction cross section, and $\sigma_{n,xn}$ is the neutron multiplication cross section.

Cross section magnitudes are strongly dependent on the energy of the incident neutron, which are categorized according to Table 2.1 [18, 20]. In general, the cross

section decreases with increasing energy—or, the probability of the reaction occurring decreases when the incident neutron has more energy—but can have extreme fluctuations across a broad energy range. This is demonstrated in Fig. 2.2, which plots the energy-dependent total cross sections for a heavy nucleus (^{235}U), an intermediate weight nucleus (^{113}Cd), and a light nucleus (^{10}B). Three regions are denoted in the plot: $1/v$ region, resonance region, and fast neutron region. In the $1/v$ region, where v is neutron velocity, σ decreases linearly with energy on a log-log plot between thermal and epithermal neutrons. Neutrons have a greater probability to be affected by the nuclear forces of the nucleus at these energies, because they move slower through matter and increase the probability of absorption into the nucleus. The resonance region contains a series of many resonance peaks, particularly for intermediate and heavy weight nuclei. Resonance peaks appear in the spectrum when a neutron's energy correlates to one of the quantum states in the nucleus, making it an ideal energy for the neutron to absorb into the nucleus. Light nuclei generally have few or no resonance peaks in this region [18, 20].

Table 2.1: Neutron energy classifications

Classification	Energy [MeV]
Thermal Neutrons	$2.5{\cdot}10^{-8}$
Epithermal Neutrons	$< 10^{-3}$
Intermediate Neutrons	10^{-3} – 1
Fast Neutrons	> 1

Note that the (α, n) reaction described in the previous section is not included in the neutron-induced cross section, because it is an alpha-induced reaction that produces a neutron. This reaction is, however, represented by its own microscopic cross section that can be described in a similar fashion to neutron-induced reactions. The (α, n) microscopic cross section represents the probability that an alpha particle

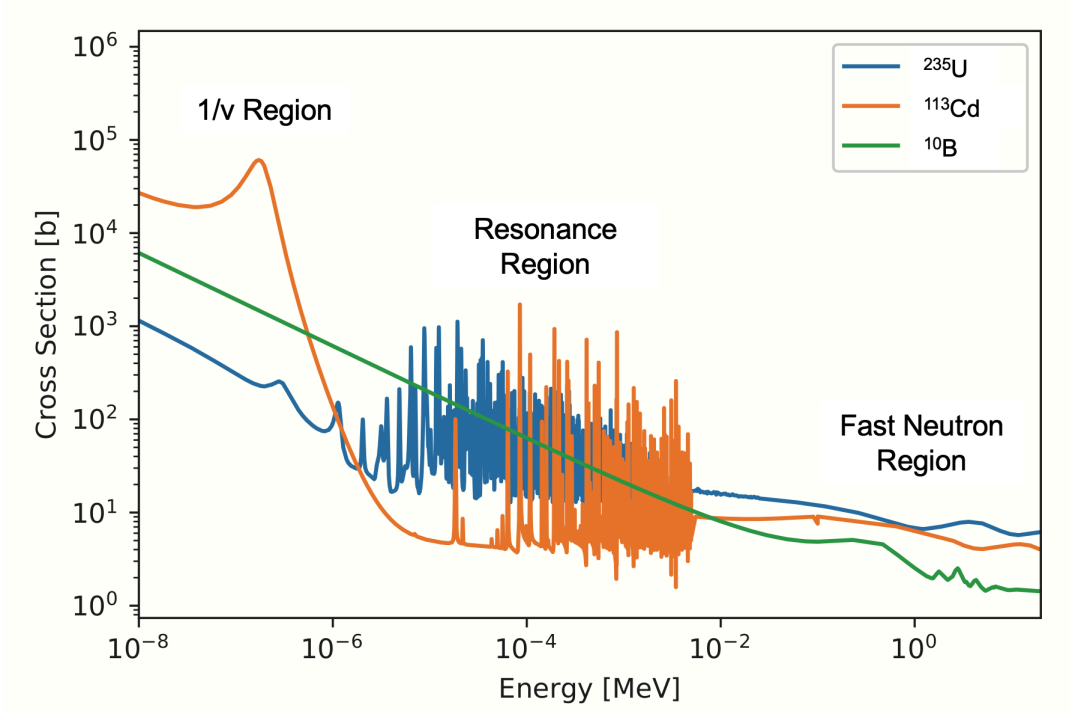

Figure 2.2: Cross section plots for ^{235}U, ^{113}Cd, and ^{10}B [1]

is absorbed by the light element and emits a single neutron.

2.4 Monte Carlo N-Particle Code

Monte Carlo N-Particle (MCNP) is a computer simulation code created to model neutron, photon, and electron transport in three-dimensional geometric cells containing specified materials using the Monte Carlo method [27, 28]. This code was developed after World War II to model nuclear physics processes and is maintained by Los Alamos National Laboratory [29]. MCNP tracks individual particle or photon histories originating from a user-defined source as each particle moves through the geometric cells. At each interaction, probabilities define the direction, energy, path length, and type of reaction to occur. This continues until the particle or photon is absorbed or travels outside of the system. If the reaction produces more particles or

photons as reaction products, then new particle or photon histories are tracked until the particles or photons are terminated. The results are then tallied in a specific cell or over a surface and averaged over all particle histories. MCNP has been benchmarked for a diverse range of nuclear fields, including nuclear criticality safety and radiation shielding [30–34]. In international safeguards, the code is most commonly used to design new radiation detection systems and characterize system performance prior to field deployment [35]. An example of this is the development of the Advanced Experimental Fuel Counter (AEFC) [36]. The AEFC combines active and passive neutron counting and gamma-ray measurement capabilities to characterize spent nuclear fuel. AmLi sources are typically used for active interrogation to determine the ^{235}U content in the item. However, a study was performed to determine if AmLi could be replaced by ^{252}Cf for active interrogation in the AEFC. MCNP simulations were critical to benchmark the AEFC performance and confirm the increase in fissions detected was from spontaneous fission of ^{252}Cf [37].

2.5 SOURCES

SOURCES is a computer code that determines neutron production rates and neutron energy spectra from spontaneous fission neutrons, (α,n), and delayed neutrons due to radionuclide decay neutrons for complex source compositions [9, 38]. Spontaneous fission spectra are calculated using half-life data, spontaneous fission branching ratios, and Watt fission spectrum parameters. The (α, n) spectra are determined by α decay from actinides in the source material, (α, n) reaction cross sections for low-Z target material, and α stopping cross sections. Delayed neutron spectra are calculated using delayed neutron branching fractions and half-lives of the parent radionuclide [38]. The code has four different problem types for the user to choose

from: homogeneous mixture problem, beam problem, two-region interface problem, three-region interface problem. The homogeneous problem has alpha emitting and spontaneous fission sources intimately mixed with low-Z target materials. The homogeneous mixture problem is most commonly used in international safeguards, because it most closely represents the source material medium. The beam problem is used solely for (α, n) reactions, and simulates the scenario where a monoenergetic beam of α particles are incident on a low-Z material. The two-region and three-region interface problems are similar. Both essentially resemble materials sandwiched together where one is a slab of alpha-emitting material and another is a low-Z target material. The main difference is that the two-region problem involves only two slabs of material and the three-region problem involves three slabs of material sandwiched together [38]. The code outputs the neutron source magnitude, neutron energy spectra from each component in the material and the total neutron energy spectrum. The binning structure of the neutron energy spectra is specified by the user and does not have to be linear [38]. The code has been benchmarked to experimental data for both the neutron source magnitude and neutron energy spectra [9, 39]. However, the spectra and magnitude calculations were accurate only to within $\pm$18% [9]. A more robust benchmarking study was performed for PuO_2, and SOURCES agreed within 12.5% with experimental results [39]. SOURCES is continually being updated as more information becomes available. The current version of the code is SOURCES-4C.

2.6 Thermal Neutron Detection

Traditional thermal neutron counters in international safeguards detect neutrons using proportional counters filled with ^{3}He gas at a pressure of 4–10 atm and surrounded by high-density polyethylene (HDPE) [20]. Proportional counters are

gas-filled detectors that use gas multiplication to create an electrical pulse [26]. Gas multiplication is initiated when electrons are freed from fill gas atoms when ionizing radiation passes through the detector volume, producing an ion pair consisting of free electrons and positive ions. In the presence of a sufficient electric field, the free electrons will accelerate and gain kinetic energy as they move towards the anode, freeing more electrons from additional fill gas atoms in the process. This process continues until the free electrons do not possess enough energy to produce another ion pair. The resultant free electrons collect at the anode to create an electrical pulse proportional to the energy deposited in the detector volume from the initial radiation event. Since neutrons are indirectly ionizing radiation, they require a secondary reaction to ionize the gas in a proportional counter.

Helium-3 is an ideal fill gas for neutron detection because it produces charged particle reaction products, has a large thermal neutron cross section, and has excellent gamma-ray discrimination abilities. The (n,p) reaction is the prevailing neutron-induced reaction for ^{3}He, as shown in Fig. 2.3, meaning this reaction is likely to occur if a neutron is in the presence of a ^{3}He nucleus. This reaction produces a proton and a triton such that

$$^3_2\mathrm{He} + ^1_0\mathrm{n} \longrightarrow ^3_1\mathrm{H} + ^1_1\mathrm{p} + 0.764 \text{ MeV}.$$

Because the proton and triton are charged particles, they are capable of ionizing the fill gas to produce an electrical signal and indicate the presence of a neutron. The thermal neutron cross section is 5330 b for the ^{3}He(n,p) reaction [20]. The pulses produced from γ rays and neutrons in ^{3}He are well-separated in energy and thus easily discriminated to eliminate the γ-ray signal when performing neutron measurements.

HDPE is a common neutron moderator used in thermal neutron detection systems. Moderation is the process of reducing a neutron's speed to increase the

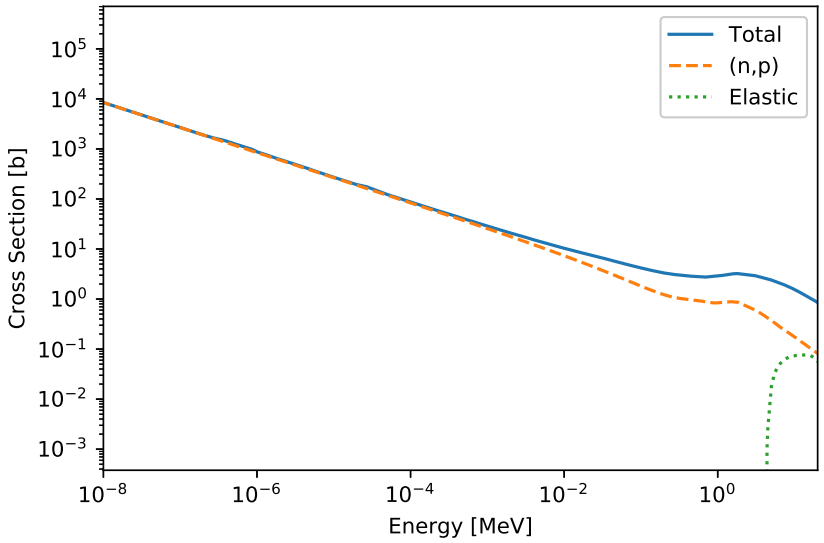

Figure 2.3: Total, elastic, and (n,p) cross section plots for ^{3}He [1]

probability of a reaction occurring in a thermal neutron detector, such as ^{3}He or BF_3 detectors [26]. Because of its neutral charge, a neutron is not subjected to Coulomb forces from atomic electrons to slow it down as it travels through matter. Scatter events are thus relied on to moderate neutrons through direct interaction with nuclei to reduce the neutron's speed and, in turn, energy. Conversion of energy and momentum dictate that light nuclei, such as H and C, are most efficient at neutron moderation because they are similar in mass to a neutron. The composition of HDPE is a series of H and C atoms, making it the ideal neutron moderator. It is also readily available in large sizes at a low cost, making it a cost effective and readily available material as well.

2.7 Multisphere Neutron Spectrometers

Multisphere spectrometers, frequently referred to as BSS, are popular because of their near isotropic response and ability to cover a wide energy range from thermal to GeV neutrons [40]. The spectrometer, first described by Bramblett et al. [14], consists of a set of a polyethylene moderating sphere with different diameters and a thermal neutron sensor that is placed in the center of each sphere for neutron measurements. With different diameters, and thus different quantities of neutron moderating material between the neutron field and detector, the detector response changes such that the peak of the response function (i.e. the optimal neutron energy for detection) shifts towards higher energies with increasing moderator diameter. Combining the detector response functions with neutron measurements collected using a set of moderating spheres allows for derivation of the neutron energy spectrum using an unfolding algorithm.

Unfolding the neutron energy spectrum for an unknown neutron emitter is a difficult task when using a thermal neutron counter, such as the ^{3}He proportional counter commonly utilized in international safeguards neutron instrumentation. A single neutron measurement can merely provide the number of neutrons detected in a given time frame with no information about the energy spectrum. Multiple neutron measurements, on the other hand, can provide insight into the neutron spectrum when varying thicknesses and types of moderator are placed between the source and neutron detector, causing a change in the response function versus initial neutron energy. The response peaks at higher neutron energies for increasing thicknesses of moderator. Mathematically, the response is related to the count rate and neutron

energy spectrum by a Fredholm integral of the first kind

$$M_d = \int_0^\infty R_d\left(E\right)\phi\left(E\right)\partial E \tag{2.5}$$

where M_d is the measured count rate [cps] for a given moderator d, $R_d(E)$ is the response function [counts/(n/cm^2)] for the given moderator, and $\phi(E)$ is the neutron fluence spectrum [n/cm^2·s] [40, 41]. Although the true response functions and spectral fluence are continuous functions, they must be discretized to numerically solve the unfolding problem. The discretized version of Eqn. 2.5 is

$$M_d = \sum_{j=1}^{n} R_{d,j}\phi_j \tag{2.6}$$

where $R_{d,j}$ is the discretized response function [counts/(n/cm^2)] for each energy bin j and ϕ_j is the discretized fluence spectrum [n/cm^2·s] [40, 41]. Because there are often fewer moderators than there are energy groups to be solved for, Eqn. 2.6 is an underdetermined problem and can only be solved through a combination of trial-and-error and additional *a priori* information [41].

2.7.1 Thermal Neutron Sensors

Most multisphere spectrometers utilize a thermal neutron detector based on a charged-particle reaction with a high thermal neutron cross section. Early multisphere spectrometers used a ^{6}LiI(Eu) scintillator, which utilized the ^{6}Li(n,α)^{3}H reaction (Q=4.78 MeV) for thermal neutron detection [14, 42, 43]. LiI(Eu) scintillators have a high mass density and can thus be small and attain close to 100% efficiency for thermal neutrons [44]. However, the iodine present in the scintillator also readily detects gamma rays within the scintillator. The gamma-ray fluence increases proportional to

the neutron fluence, so a discriminator must be set for each sphere in each unique neutron/gamma ray field [44].

An alternative to ^{6}LiI(Eu) scintillators is the $^{10}BF_3$ proportional counter, although it has mainly been used for spectral measurements [45, 46]. Thermal neutron detection is achieved using the ^{10}B(n,p)^{7}Li reaction (Q = 2.78 MeV). Neutron- and gamma ray-induced events are well separated on a pulse height spectrum for this counter. A simple low-level discriminator can thus be set to reject the gamma ray-induced pulses and remains the same for each sphere in all neutron/gamma ray fields [44].

The ^{3}He proportional counter is another alternative to LiI(Eu) scintillator with similar characteristics to the $^{10}BF_3$ proportional counter as discussed in an earlier section. Compared to the LiI(Eu) scintillator, the common SP9 spherical ^{3}He proportional counter is more sensitive with fluence responses on the order of 14 times greater than the LiI(Eu) scintillator [44, 47–49]. This makes it an excellent choice for low-level measurements [44]. Because this is the most common neutron detector for international safeguards applications, it will be used in this work for development of the inverse Bonner sphere spectrometer.

2.7.2 Response Functions

The response function relates the instrument reading to the energy-dependent neutron fluence spectrum and is analogous to intrinsic detection efficiency. However, the response function considers the fluence through the detector and not the radiation emitted from the source. The response function is defined as the ratio of the

instrument reading to the neutron fluence and is calculated as

$$R_d\left(E\right) = \epsilon_d\left(E\right) \cdot \frac{\pi d^2}{4} \tag{2.7}$$

where $\epsilon_d(E)$ is the absolute detection efficiency of neutrons with energy E [40]. A response function must be generated for each sphere and the bare source used in the unfolding. Combined, this is typically referred to as the response matrix.

Response functions were mainly experimentally determined through the 1990s prior to advances in computing and processing speed. Because most neutron sources emit neutrons over a spectrum of energies, an accelerator was required to produce most monoenergetic neutron fields for determining the detector response function [14, 44, 49, 50]. Accelerators were not readily available for calibrating each BSS individually, so characteristic detector response functions were created and used by all BSS users for a standard set of moderators.

Computational codes have been heavily relied on for characterizing the detector response functions. Discrete ordinate codes were also popular prior to computing advancements. The most popular code was ANISN [51], which solved the one-dimensional Boltzmann neutron transport equation using discrete ordinances, because it was computationally fast and reasonably reliable for a wide range of BSS with varying thermal neutron sensors [43, 45, 47, 52]. As technological advancements improved computational speed and processing power, Monte Carlo codes became the choice method to characterize the BSS detector response functions. Agreement between Monte Carlo codes and experimental results improved compared to discrete ordinance methods [40, 53, 54]. MCNP is most commonly chosen to determine the detector response functions using a detailed three dimensional model of the BSS [55–57]. Geant4, another Monte Carlo code, has recently been studied for evaluating the

BSS detector response functions [58]. Although computer simulations eliminated the need for a accelerator, the computer simulations need to be benchmarked to experimental data to confirm the model represents the physical system. Typically this is accomplished by using reference sources, such as ^{252}Cf [40].

2.7.3 Unfolding Algorithms

A number of unfolding algorithms have been developed for unfolding the neutron energy spectrum for the BSS. The algorithms vary in their background theory and include non-linear least squares regression [59, 60], the maximum entropy principle [61], genetic algorithms [62, 63], and artificial intelligence [64, 65]. Although the method to iterate through solution spectra for each algorithm may differ, the general algorithm routine to solve for Eqn. 2.6 remains the same for most BSS algorithms. The flow chart in Fig. 2.4 illustrates the general routine for a BSS algorithm. Each algorithm requires the user to input the measured data, the corresponding response functions, an input guess spectrum, and a minimum reduced chi-square value, $(\chi^2/\nu)_{min}$. The measured data, M_d, is the count rate data for each moderator, d, for the total number of moderators, D. The response functions are a discretized function for each moderator in the system. The input guess spectrum should include any *a priori* information the user has from calculations or previous measurements.

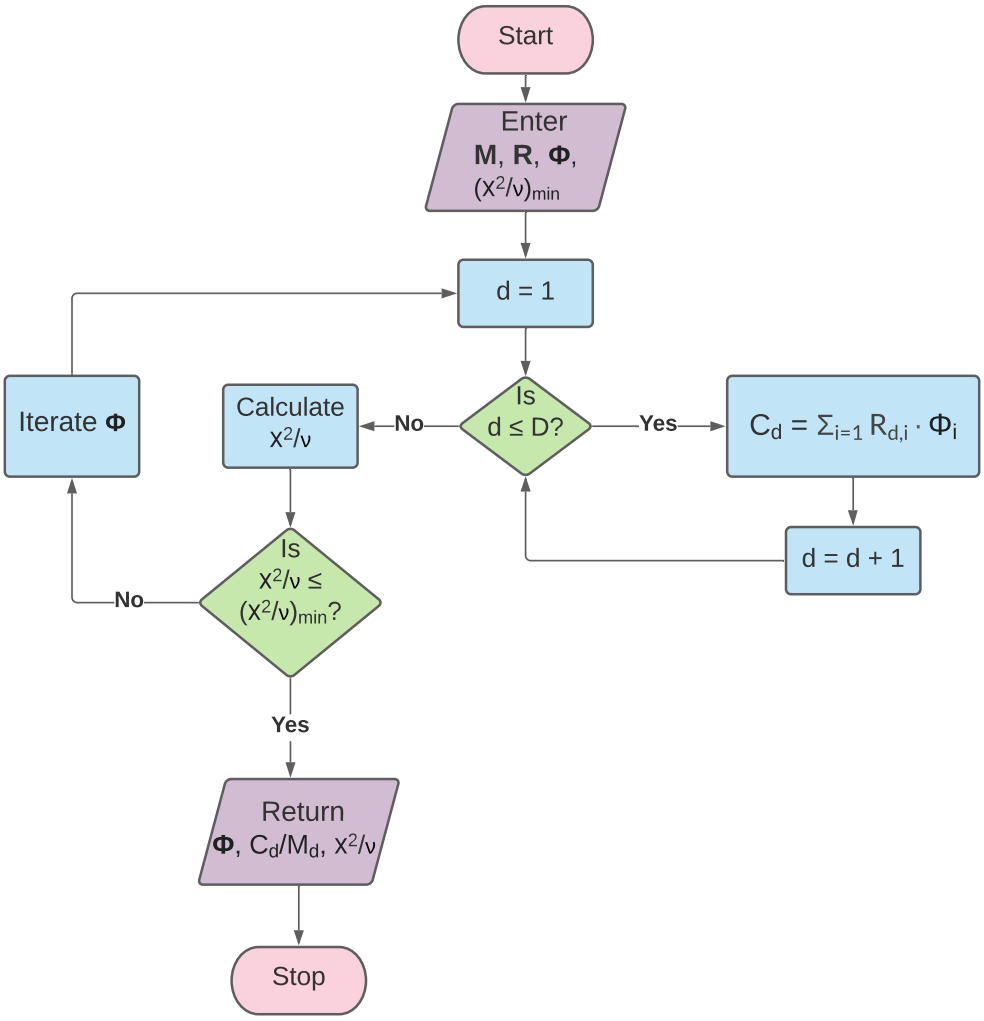

Figure 2.4: Flowchart for a general BSS unfolding algorithm

Setting $(\chi^2/\nu)_{min}$ requires an assessment of the number of degrees of freedom, ν, in the system and the significance level, α. For the standard BSS, the degrees of freedom is typically set to the number of moderators minus 1, because the number of moderators is equal to the number of measured data points entered into the algorithm. For the iBSS, this should be set to the number of moderators times the number of rings in the neutron counter minus 1 to account for the added data in the iBSS. The significance level, α, is a measure of rejecting the null hypothesis in a statistical

test. The null hypothesis for the BSS is that there is no significant difference between the measured data and the calculated data that results from folding the solution spectrum with the response functions. Essentially, it is a test to determine if the measured data could be produced by the spectrum. For development of the iBSS, the significance level was set to 1% to ensure there was a small probability of rejecting the null hypothesis and the solution spectrum not fitting the data. A two-sided chi-square test was used here due to the random nature of radioactive decay: the randomness brings a certain amount of uncertainty and thus a perfect fit (χ^2=0) cannot exist. The significance level was split in two to determine the range of admissible critical values for the two-sided chi-square test. The critical values are the limits that the χ^2 must fall within to not reject the null hypothesis and are determined such that the area under the extremes of the PDF curve are equal to the significance level. An example of setting the critical values is illustrated in Fig. 2.5 for 25 degrees of freedom and a 1% significance level. Note that the probability density function (PDF) changes with respect to the degrees of freedom, so a universal PDF cannot be used for all degrees of freedom. The admissible critical values (unshaded region) were 10.52–46.93. The admissible critical values were then divided by the degrees of freedom to determine the admissible range of critical values corresponding to the significance level and degrees of freedom set by the user. The critical value range for 25 degrees of freedom and a 1% significance level was 0.421–1.88, and $(\chi^2/\nu)_{min}$ was thus set to 0.421.

After the user enters all of the input data, the algorithm then evaluates the goodness-of-fit of the input spectrum to the measured data. The input spectrum is folded with each response function to calculate the count rate data for each moderator, C_d that would result from the input spectrum. The reduced chi-squared value, χ^2/ν,

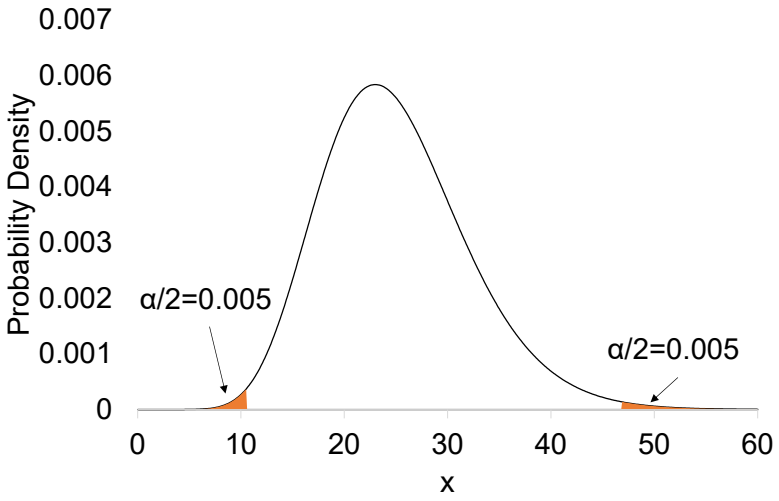

Figure 2.5: χ^2 probability density function for 25 degrees of freedom

for the spectrum is then calculated as

$$\frac{\chi^2}{\nu} = (D-1)^{-1} \sum_{d=1}^{D} \frac{(C_d - M_d)^2}{\sigma_{M_d}^2} \tag{2.8}$$

where σ_{M_d} is the standard deviation for each measured count rate [40, 41]. This value is then compared to $(\chi^2/\nu)_{min}$ to determine if the input spectrum needs to be adjusted. In most cases, the input guess spectrum is not the best match to the data, so $\mathbf{\Phi}$ undergoes adjustment to find the best fit to the measured data. The iteration process generally involves modifying the spectrum, $\mathbf{\Phi}$, calculating new C_d values and χ^2/ν for the updated spectrum, and then comparing the result to $(\chi^2/\nu)_{min}$ again to determine if the iteration process needs to continue. The procedure for iterating $\mathbf{\Phi}$ and optimizing it to fit the measured data is where most BSS unfolding algorithms differ. The algorithm generally terminates when χ^2/ν is minimized [40, 41].

MAXED and GRAVEL are among the most common codes used for unfolding the neutron energy spectrum using the BSS [60, 61, 66]. They were chosen for this work they are well-established unfolding algorithms and offer a performance compar-

ison to many BSS studies. Other codes that were considered were STAY'SL [67] and FRUIT [68]. STAY'SL and FRUIT both offer the opportunity to include uncertainty in the unfolding on a bin-by-bin basis. However, uncertainties in the input data, particularly for the response functions and input guess spectrum, are typically not well-defined or defined at all. Neither of these codes can unfold the neutron energy spectrum without inputting uncertainties for all input data. The uncertainties in the input data for developing the iBSS were not known or not well-known for all input data, limiting the functionality of these unfolding codes for this application. MAXED and GRAVEL were ultimately better suited for this work, though other unfolding codes could be considered for future work.

The MAXED (MAXimum Entropy Deconvolution) algorithm is a Bayesian code that is based on the maximum entropy principle, which requires the best solution to have the largest entropy to reduce errors and biases in the unfolding [61]. Because it is based on Bayes' theorem, MAXED requires good *a priori* information to be included in the input guess spectrum. The goal of MAXED is to produce an optimum solution spectrum with the new knowledge from the measured data while still remaining as close as possible to the input guess spectrum. To quantify how close a spectrum is to the input guess spectrum, MAXED uses entropy, S, which is quantified for each admissible spectrum, f_i, by

$$S = -\sum \left[f_i \cdot \ln\left(\frac{f_i}{f_i^{DEF}}\right) + f_i^{DEF} - f_i \right] \tag{2.9}$$

where f_i^{DEF} is the input guess spectrum. MAXED chooses the best solution based on the maximum value of S. Note that S is a negative quantity, so the largest value is the one closest to 0. Maximization of S is dependent on a potential function, $Z(\lambda_k)$,

defined as

$$Z(\lambda_k) = -\sum f_i^{DEF} \exp\left(-\sum \lambda_k R_{ki}\right) - \left[D \sum \left(\lambda_k \sigma_k\right)^2\right]^{1/2} - \sum N_k \lambda_k \qquad (2.10)$$

where λ_k is a Langrangian multiplier, R_{ki} are the discretized response functions, N_k is the measured data, and σ_k is the uncertainty in the measured data [61]. The solution spectrum is then expressed in terms of λ_k as

$$f_i = f_i^{DEF} \exp\left[-\sum_k \lambda_k \cdot R_{ki}\right]. \qquad (2.11)$$

A simulated annealing algorithm is used to find the maximum value of Z, which is a global optimization program used to find local optima [69]. Optimization of the problem involves randomly choosing a point for evaluation, evaluating the point compared to its value at the initial point, and then either accepting or rejecting that point. This continues until the algorithm reaches an optimum solution. The MAXED code terminates when Z has been optimized and S has been maximized and returns the solution spectrum and χ^2/ν for the solution spectrum [61, 66]. MAXED is not dependent on the number of iterations; the code runs until the solution is optimized through the above process.

GRAVEL is an iterative method based on non-linear least squares regression [60]. Starting from the input guess spectrum, which must be non-negative for the solution to be a non-negative answer, each iteration J of the discretized spectrum, f_i^J, is calculated according to the rule

$$f_i^{J+1} = f_i^J \cdot \exp\left[\frac{\sum_k W_{ik}^j \cdot \log\left(\frac{N_k}{R_{ki'} \cdot f_{i'}^J}\right)}{\sum_k W_{ik}^j}\right] \qquad (2.12)$$

where k is the moderator number, i is the energy bin, N_k are the measured counts, and R_{ki} are the response matrix data. The variable W_{ik}^{j} is calculated as

$$W_{ik}^{j} = \frac{R_{ki} \cdot f_i^J \cdot N_k^2}{\sigma_k^2 \sum_{i'} R_{ki} \cdot f_{i'}^J} \tag{2.13}$$

where σ_k is the estimate of the measurement error input by the user [60]. A non-linear least squares regression considers the optimal solution to be the one that minimizes the square of the difference between the measured and expected values. This is captured by minimization of the χ^2/ν value to find the optimal solution. GRAVEL thus iterates the solution spectrum until χ^2/ν is less than $(\chi^2/\nu)_{min}$ or until it reaches the set number of iterations input by the user [60]. This ensures that the null hypothesis is not rejected and that the code does not run infinitely if minimization of χ^2/ν does not reach $(\chi^2/\nu)_{min}$.

2.8 Inverse Bonner Sphere Concept

The inverse Bonner sphere concept was initially proposed as an in-situ technique to characterize AmLi sources installed in neutron collars and first demonstrated for AmLi sources, with ^{252}Cf as a monitor using a large volume active well coincidence counter (LVAWCC) [13]. The purpose of the work was to choose the best AmLi spectrum that represented physical sources. AmLi spectra that were considered were a spectrum generated in SOURCES-4C, Owen [70], Tagziria [3], Geiger and van der Zwan [2]. To determine which of these spectra most closely aligned with experimental results, AmLi sources were placed in increasing sizes of cylindrical and spherical polyethylene moderators. Neutron measurements were then collected for the inner ring, outer ring, and summed rings. The geometry was then modeled in MCNP and

simulations run with different possible AmLi spectra. The experimental and simulation results were then compared, and those with the closest results were chosen as the most suitable candidates for the AmLi spectrum. The SOURCES-4C and Owen spectra were the closest matches to the experimental results, but were not explicitly unfolded. This work will continue the previous work by expanding the inverse Bonner sphere concept to a novel neutron spectrometer for experimentally measuring neutron energy spectra from neutron emitters pertinent to international safeguards.

Chapter 3

Objectives

The aim of this work was to develop a novel neutron spectrometer using the inverse Bonner sphere concept to measure the neutron energy spectrum for safeguards-relevant neutron emitters. Well-characterized neutron sources, especially ^{252}Cf, were heavily relied upon in this work. However, discrepancies were observed in the fissioning characteristics of ^{252}Cf sources that had to be addressed prior to developing the iBSS. A method to confirm source age and isotopic ratios on the technical data sheets was developed using high-resolution gamma-ray spectroscopy. The estimated source age could then be used to determine if the neutron energy spectrum would significantly differ from the expected ^{252}Cf spontaneous fission spectrum and affect verification of the iBSS. Development of the iBSS then proceeded using MCNP simulations to demonstrate proof-of-concept for the methodology using the LVAWCC and perform sensitivity analyses. Neutron energy spectra were then experimentally unfolded using the inverse Bonner sphere spectrometer. Experimental verification of the iBSS was performed using three ^{252}Cf sources certified for use by the high-resolution gamma-ray spectroscopy method. Neutron energy spectra generated by SOURCES-4C were then compared to unfolded spectra for a high-purity $^{240}PuO_2$, AmLi, and

AmBe sources to determine if the data needed to be updated.

The specific research objectives of this work were:

1. Confirm technical data sheet information for ^{252}Cf sources necessary for verifying performance of the iBSS using high-resolution γ-ray spectroscopy,

2. Employ Monte Carlo simulations to demonstrate methodology proof-of-concept for the iBSS and perform sensitivity analyses, and

3. Experimentally unfold the neutron energy spectrum for ^{252}Cf, ^{240}Pu, AmLi, and AmBe neutron sources using the iBSS

Work performed to fulfill each objective led to a peer-reviewed publication that is published or being prepared for submission. The manuscripts for each objective are presented in order in the proceeding chapters. The work presented in Chapter 4 was published in *Applied Radiation Isotopes* with the title "Characterization of ^{252}Cf Sources Using High-Resolution Gamma Spectroscopy" [71]. Chapter 5 presents the simulation work associated with developing a method for unfolding the neutron energy spectrum using the iBSS. This work was prepared for submission to in *Nuclear Instruments and Methods in Physics Research A* with the title "Unfolding Neutron Energy Spectra Using the Inverse Bonner Sphere Concept". Chapter 6 was a continuation of chapter 5 and presents the experimental results for unfolding the neutron energy spectrum. This work was prepared for submission to *Nuclear Instruments and Methods in Physics Research A* with the title "The Inverse Bonner Sphere Spectrometer as a Verification Method for SOURCES-4C".

Chapter 4

Characterization of ^{252}Cf Sources Using High-Resolution Gamma Spectroscopy

Abstract

Californium-252 is used as a neutron calibration source for passive neutron correlation counting. Source age and isotopic information are needed to make decay corrections to the neutron emission rate due to the influence of ^{250}Cf. Gamma-ray signatures present in the spectrum from spontaneous fission products and odd-numbered Cf isotopes can be used with high accuracy to confirm or query declared values on a technical data sheet. This method is good practice for independently verifying the content of ^{252}Cf calibration sources.

4.1 Introduction

Passive neutron correlation counting is employed in nuclear safeguards to measure the mass of plutonium in bulk items [72]. This method is dependent on the detection of two or more time-correlated neutrons from a spontaneous fission event. Accidental neutron correlation events, such as those produced from the (α, n) reaction, ambient background, or overlapping uncorrelated fission events, are traditionally separated from true coincidence events in a statistical way using shift register electronics [22]. In shift register electronics, a reals-plus-accidentals (R+A) gate opens following an initial neutron trigger to detect any possible subsequent coincident neutrons. To determine the accidental rate within the R+A gate, a second gate (A gate), is opened for the same time as the R+A gate after a long delay (typically 4096 μs, which is much greater than the neutron lifetime in moderated capture-detector arrays [72]). The long delay ensures that any time correlation from the initial trigger event is removed. Subtracting the counts in the A gate from the R+A gate returns the reals rate. In the simplest approach, the background-corrected net reals rate is empirically related to the plutonium mass in an item based on a system calibration typically utilizing a ^{252}Cf source.

Californium-252 ($T_{1/2}$ = 2.645 y [73]) is an isotope used to characterize and calibrate passive neutron correlation counters. This isotope has a high spontaneous fission branching ratio (3.09%), a high neutron emission rate per unit mass ($2.31 \cdot 10^6$ s^{-1} μg^{-1}), and a prompt fission spectrum similar to other neutron emitters in the fuel cycle, namely ^{240}Pu [20, 73]. It is also the dominant neutron emitter in freshly irradiated, chemically separated californium sources, so the source resembles pure ^{252}Cf despite the inevitable presence of secondary neutron emitters, notably ^{250}Cf [74]. Californium-252 is thus a convenient isotope for fabricating compact neutron sources

that approximate to a point. Commercially available sources are readily available from several vendors and typically have recommended working lives of about 15 y, though this recommendation is based on the possibility of capsule failure rather than radiative contributions from secondary neutron emitters [74].

The two secondary neutron emitters of potential concern in a ^{252}Cf source are ^{250}Cf and ^{248}Cm. Californium-250 ($T_{1/2}$ = 13.08 y [75]) is produced from neutron capture of ^{249}Cf or beta decay of ^{250}Bk during irradiation of ^{249}Bk to produce ^{252}Cf. This isotope is elementally the same as ^{252}Cf and cannot be chemically separated post-irradiation. Consequently, isotopic composition must be accurately noted on the technical data sheet (TDS) so that the quantity of ^{250}Cf contributing to the overall neutron emission rate can be accounted for as the source ages. Curium-248 ($T_{1/2} = 3.48 \cdot 10^5$ y [76]) is chemically separated from ^{252}Cf post-irradiation, but grows into the source via α decay of ^{252}Cf. However, ^{248}Cm is unlikely to contribute significantly to the neutron emission rate until the source is more than 40 years old, because the relative neutron yield of ^{248}Cm remains less than 10% of the total yield in the source depending on initial source isotopic ratios [74]. At the end of the recommended working life, the ^{248}Cm contribution is typically on the order of 10^{-5}% of the total neutron yield [74].

A ^{252}Cf source was recently purchased for calibrating neutron counters developed for nuclear safeguards instrumentation at Oak Ridge National Laboratory (ORNL). The source request specified ^{252}Cf from a freshly irradiated batch to ensure that it was dominated by ^{252}Cf for high-accuracy, absolute source calibration using passive neutron correlation counting [77, 78]. Upon counting the new and old sources on the large-volume active well coincidence counter operated in passive mode [79], the ratios of the doubles-to-singles counting rates, which is a measure of the fission rate to the total neutron emission rate, from each source were discovered to be statistically

different at the 3-σ limit. Because the doubles-to-singles ratio is a direct measure of the nature of the source and indicative of the neutron multiplication in a multiplying sample matrix, the ratios of all similarly encapsulated sources are expected to agree if the Cf is from a freshly irradiated batch. The cause of this discrepancy was unknown and led to the investigation reported in this work.

Gamma-ray spectroscopy is rarely performed on ^{252}Cf sources intended for metrological purposes because the gamma-ray spectra have generally been assumed to provide little useful information. However, gamma-ray signatures from spontaneous fission products (SFP) are present in the spectrum and have been exploited to estimate ^{252}Cf source age [80, 81]. Source age can be calculated by setting the experimental ratio of the gamma-ray emission rate from the 661.657 keV line from ^{137}Cs ($T_{1/2}$ = 30.08 y [82]) to the gamma-ray emission rate from a short-lived fission product equal to the theoretical ratio of the same gamma ray emission rates derived using the Bateman equations [83] and solved for time. In essence, ^{137}Cs logs the total number of fissions, whereas the shorter-lived nuclides mark present decay rates. Previous work measured the source age to within 1% of the value reported by the vendor using this method [80, 81]. These works did not, however, include a comprehensive method for calculating measurement uncertainty, fission product in-growth from both secondary neutron emitters ^{250}Cf and ^{248}Cm, or isotopic analysis using gamma-ray spectroscopy.

The work described here used high-resolution gamma-ray spectroscopy to characterize ^{252}Cf sources currently used for detector calibration by confirming source age and isotopic ratios. Uncertainty analyses were performed to determine which short-lived product(s) are best for calculating source age using gamma-ray spectroscopy.

4.2 Materials and Methods

4.2.1 Data Collection

Gamma-ray spectra were collected using an n-type high-purity germanium detector (Model GL2820R/S, Canberra Industries, Meriden, Connecticut). The primary concern for collecting a gamma-ray spectrum from a ^{252}Cf source was radiation damage to the detector from prolonged neutron exposure. The neutron flux from each neutron source was small enough to cause little radiation damage and resolution degradation [84]. However, to limit damage from prolonged neutron exposure, an aged detector with degraded performance from prior use was used. Preliminary results established that spectral resolution was acceptable for this methodology.

Energy calibration and detection efficiency were determined using a ^{152}Eu source (4.7 μCi). The source was placed 15 cm from the face of the detector along the centerline and a gamma-ray spectrum collected for 2 h. A 2-h background spectrum was then collected and subtracted from the ^{152}Eu gamma-ray spectrum using PeakEasy 4.98.1 [85]. The peak locate and peak analysis algorithms in Canberra Genie$^{\text{TM}}$ 2000 Spectroscopy Software (V3.4.1) [86] were used to locate ^{152}Eu peaks in the spectrum and calculate net count rate with associated uncertainty for each identified peak. The absolute full-peak detection efficiency curve was constructed using seven gamma rays in the ^{152}Eu spectrum. The absolute full-energy peak efficiency, ϵ_{abs}, was calculated for each peak by

$$\epsilon_{abs} = \frac{CR}{A \cdot I_\gamma} \tag{4.1}$$

where CR is the net count rate in the gamma-ray full-energy peak corrected for capsule attenuation, A is the decay-corrected source activity [Bq], and I_γ is the gamma-

ray yield [γ/decay]. The absolute detection efficiency curve was normalized to the efficiency at 661.657 keV to create the relative detection efficiency curve.

Five ^{252}Cf sources were measured. They were labeled as sources A–E to remove any identifying information to a specific vendor. Sources D and E were older sources included to extend the dynamic range of calculated source ages and serve as a test of the method. Source A was placed 20 cm from the face of the detector along the centerline and sources B–E were placed 15 cm from the face of the detector along the centerline. These distances were chosen to keep the dead time under 10% and also to ensure true coincidence summing was negligible. Spectra were collected in 2-h increments for quality control purposes for a total of 42 h for sources A–C and 48 h for sources D and E and background. Each 2-h spectrum was summed for each source and background in PeakEasy 4.98.1 [85]. The summed background spectrum, normalized in time, was then subtracted from each summed and time-normalized source spectrum. Spectra were then analyzed in Genie^{TM} 2000 [86] using the VMS Standard Peak Search peak locate algorithm to locate fission product peaks followed by the Sum/Non-Linear Least Squares Fit peak area algorithm to quantify the net count rate with associated uncertainty for each identified peak in the spectrum.

4.2.2 Methodology for Calculating Source Age

Source ages were calculated by setting the experimental ratio, R_{exp}, of the count rate of two SFPs equal to the theoretical ratio of the gamma-ray emission rates from the same SFPs derived using the Bateman equations and solving for time. In this case, time represents time passed since the last Cm separation and not time since irradiation of the production batch, because the fission products would have been stripped from the source during the Cm separation. All source material can be

traced to Cf produced in the High Flux Isotope Reactor at ORNL.

The experimental ratio is a measure of the current source age. Cesium-137 is a long-lived isotope that accumulates as the source ages for the age range studied here, and the short-lived SFP is a measure of the present fission rate. The experimental ratio was calculated by dividing the net count rate of the ^{137}Cs 661.657 keV peak by the net count rate of the short-lived SFP gamma-ray peak and accounting for relative detection efficiency respective to the 661.657 keV peak, $\epsilon_{rel,661}$, such that

$$R_{exp} = \frac{CR(^{137}\text{Cs})}{CR(x)} \cdot \epsilon_{rel,661}(E_x) \tag{4.2}$$

where $CR(^{137}\text{Cs})$ and $CR(x)$ are the capsule attenuation-corrected net count rates in the gamma-ray full-energy peak for the ^{137}Cs and isotope x, respectively, and E_x is the gamma-ray energy emitted from isotope x [keV].

Theoretical ratios required derivation of the gamma-ray emission rate equations from the Bateman equations [83]. This ratio is dependent on time, which was solved for to calculate source age when set equal to the experimental ratio. Gamma-ray emission rate equations for SFP in-growth and decay were derived starting from the Bateman equations for spontaneous fission and α decay of ^{252}Cf, ^{250}Cf, and ^{248}Cm. Note that the ^{248}Cm Bateman equation also included a term for in-growth of ^{248}Cm from α decay of ^{252}Cf. Bateman equations were then derived and solved for production and decay of spontaneous fission product from ^{252}Cf, ^{250}Cf, and ^{248}Cm individually. The Bateman equations were solved for using the separation of variables technique for solving differential equations; only one solution was found. Each equation was normalized to initial activity of ^{252}Cf, $A_0(^{252}\text{Cf})$, to cancel out this variable in most of the equations when calculating the theoretical ratio. Initial quantities of ^{252}Cf and ^{250}Cf were assumed to be present in the source; ^{248}Cm was assumed to be fully

chemically separated at time zero. The resulting gamma-ray emission rate equation for isotope x from ^{252}Cf spontaneous fission, $G_{\text{Cf-252}}(x)$ [γ/s], was

$$\frac{G_{\text{Cf-252}}(x)}{A_0(^{252}\text{Cf})} = \frac{1}{1 - \frac{T_{1/2,x}}{T_{1/2,\text{Cf-252}}}} \cdot S_{\text{Cf-252}} \cdot Y_{x,\text{Cf-252}} \cdot I_x \cdot \left(e^{-\frac{\ln 2}{T_{1/2,\text{Cf-252}}} t} - e^{-\frac{\ln 2}{T_{1/2,x}} t} \right) \quad (4.3)$$

where $T_{1/2,\text{Cf-252}}$ and $T_{1/2,x}$ are the half-lives of ^{252}Cf and isotope x [y], respectively, $S_{\text{Cf-252}}$ is the ^{252}Cf spontaneous fission branching ratio [fissions/decay], $Y_{x,\text{Cf-252}}$ is the cumulative spontaneous fission product yield of isotope x from ^{252}Cf [atoms of isotope x/fission], I_x is the gamma-ray yield from isotope x [γ/decay], and t is time [y]. The gamma-ray emission rate equation for isotope x from ^{250}Cf spontaneous fission, $G_{\text{Cf-250}}(x)$ [γ/s], was

$$\frac{G_{\text{Cf-250}}(x)}{A_0(^{252}\text{Cf})} = \frac{1}{1 - \frac{T_{1/2,x}}{T_{1/2,\text{Cf-250}}}} \cdot S_{\text{Cf-250}} \cdot Y_{x,\text{Cf-250}} \cdot I_x \cdot \frac{A_0(^{250}\text{Cf})}{A_0(^{252}\text{Cf})} \cdot \left(e^{-\frac{\ln 2}{T_{1/2,\text{Cf-250}}} t} - e^{-\frac{\ln 2}{T_{1/2,x}} t} \right) \quad (4.4)$$

where $T_{1/2,\text{Cf-250}}$ is the half-life of ^{250}Cf [y], $S_{\text{Cf-250}}$ is the ^{250}Cf spontaneous fission branching ratio [fissions/decay], and $Y_{x,\text{Cf-250}}$ is the cumulative spontaneous fission product yield of isotope x from ^{250}Cf [atoms of isotope x/fission], and $A_0(^{250}\text{Cf})/A_0(^{252}\text{Cf})$ is the ratio of initial activities of ^{250}Cf to ^{252}Cf. The initial activity ratio is related to the initial atom ratio by

$$\frac{A_0(^{250}\text{Cf})}{A_0(^{252}\text{Cf})} = \frac{N_0(^{250}\text{Cf}) \cdot T_{1/2,\text{Cf-252}}}{N_0(^{252}\text{Cf}) \cdot T_{1/2,\text{Cf-250}}} \quad (4.5)$$

where $N_0(^{250}\text{Cf})$ and $N_0(^{252}\text{Cf})$ are the initial atom percent values of ^{250}Cf and ^{252}Cf, respectively. Typically, initial atom ratios of ^{250}Cf to ^{252}Cf are 0.10–0.15, and initial activity ratios are 0.02–0.03. The gamma-ray emission rate equation for isotope x

from ^{248}Cm spontaneous fission, $G_{\text{Cm-248}}(x)$ [γ/s], was

$$\frac{G_{\text{Cm-248}}(x)}{A_0(^{252}\text{Cf})} = \frac{1}{1-\frac{T_{1/2,\text{Cm-248}}}{T_{1/2,\text{Cf-252}}}} \cdot S_{\text{Cm-248}} \cdot Y_{x,\text{Cm-248}} \cdot I_x$$
$$\cdot \left[\frac{1}{1-\frac{T_{1/2,x}}{T_{1/2,\text{Cf-252}}}} \left(e^{-\frac{\ln 2}{T_{1/2,\text{Cf-252}}}t} - e^{-\frac{\ln 2}{T_{1/2,x}}t} \right) - \frac{1}{1-\frac{T_{1/2,x}}{T_{1/2,\text{Cm-248}}}} \left(e^{-\frac{\ln 2}{T_{1/2,\text{Cm-248}}}t} - e^{-\frac{\ln 2}{T_{1/2,x}}t} \right) \right] \tag{4.6}$$

where $T_{1/2,\text{Cm-248}}$ is the half-life of ^{248}Cm [y], $S_{\text{Cm-248}}$ is the ^{248}Cm spontaneous fission rate [fissions/decay], and $Y_{x,\text{Cm-248}}$ is the cumulative spontaneous fission product yield of isotope x from ^{248}Cm [atoms of isotope x/fission].

Two mathematical models were derived for calculating the theoretical ratio. Model I only accounts for SFP in-growth from spontaneous fission and decay of ^{252}Cf and is the same model used by Gehrke [80]. It is suitable for freshly irradiated sources that are dominated by ^{252}Cf. The theoretical ratio equation for Model I, $R_{th,1}$ is

$$R_{th,I} = \frac{G_{\text{Cf-252}}(^{137}\text{Cs})}{G_{\text{Cf-252}}(x)}. \tag{4.7}$$

Model II accounts for SFP in-growth from spontaneous fission and decay of ^{252}Cf, ^{250}Cf, and ^{248}Cm. The theoretical ratio equation for Model II, $R_{th,2}$ is

$$R_{th,II} = \frac{G_{\text{Cf-252}}(^{137}\text{Cs}) + G_{\text{Cf-250}}(^{137}\text{Cs}) + G_{\text{Cm-248}}(^{137}\text{Cs})}{G_{\text{Cf-252}}(x) + G_{\text{Cf-250}}(x) + G_{\text{Cm-248}}(x)}. \tag{4.8}$$

Source age was calculated by setting the experimental ratio equal to the theoretical gamma-ray emission rate ratio and solving for time, t.

4.2.3 Uncertainty Analysis

The standard deviation for source age, σ_t, was calculated using

$$\sigma_t = \sqrt{\sum \sigma_{u_i}^2 \left(\frac{\partial t}{\partial u_i}\right)^2} \tag{4.9}$$

where u_i is the ith variable in Model I or Model II, and σ_{u_i} is the uncertainty associated with u_i. However, the derivative in Eqn. 4.9 could not be analytically derived from Eqns. 4.7 or 4.8, because t could not be isolated. The forward-backward finite difference method was instead used as a numerical approximation to estimate the derivative in Eqn. 4.9. For this work, the forward-backward finite difference method was calculated as

$$\frac{\partial t}{\partial u_i} = \frac{t\left(u_i + \sigma_{u_i}\right) - t\left(u_i - \sigma_{u_i}\right)}{2\sigma_{u_i}}. \tag{4.10}$$

The ith variable and associated uncertainty in Eqn. 4.10 were substituted for the value and associated uncertainty, respectively, for each variable in Eqns. 4.7 or 4.8. This was repeated for each variable included in Models I or II to solve for the source age uncertainty in Eqn. 4.9.

4.3 Results and Discussion

High-resolution gamma-ray spectra, shown in Fig. 4.1, were collected for five ^{252}Cf sources of varying ages. Background is subtracted from each spectrum. Each spectrum was normalized to the maximum net count rate in the 661.657 keV peak of ^{137}Cs for comparison based on source age. All spectra had the same conversion gain. Cesium-137 records the number of fissions since Cm separation and thus acts as a metric for source age. The prominent peaks from left to right in order of increasing

energy are Cm K-series x-rays between 104 and 123 keV, ^{251}Cf gamma ray peak at 177.52 keV, ^{249}Cf gamma ray peaks at 333.37 and 388.17 keV, and ^{137}Cs gamma ray peak at 661.657 keV; all other discernable peaks are short-lived SFP. No notable impurities were identified in the gamma-ray spectra for any of the sources.

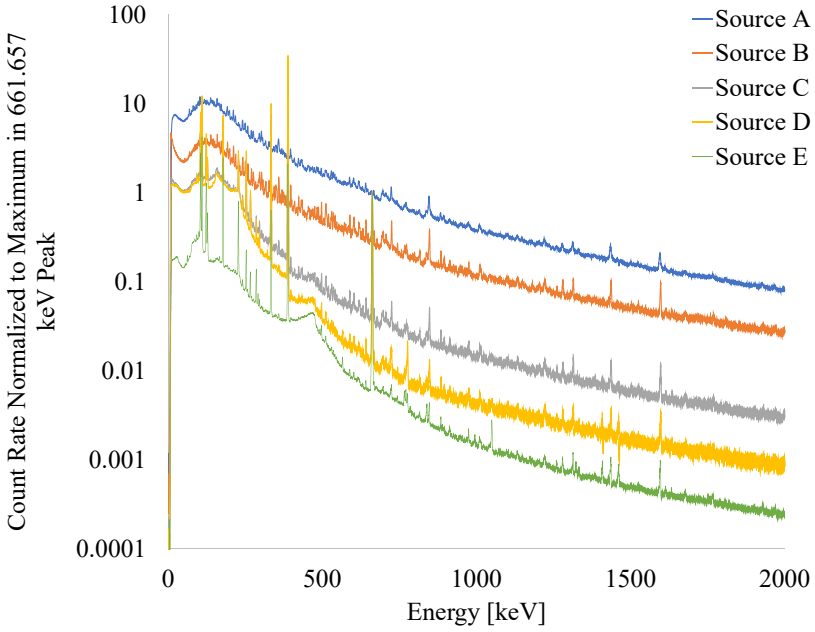

Figure 4.1: Californium-252 spectra for sources A–E normalized to the maximum count rate in the 661.657 keV gamma-ray peak.

4.3.1 Californium-252 Source Ages

Gamma-ray peaks from four SFP—^{132}I, ^{136}I, ^{138}Cs, and ^{142}La—were chosen to calculate source age. Iodine-136, ^{138}Cs, and ^{142}La were chosen because they have SFP yields $> 2\%$ and are resolvable peaks in the ^{252}Cf gamma-ray spectrum. Iodine-132 was used as a comparison to Gehrke et al. ([80]). The the properties of the spontaneous fission nuclides are listed in Table 4.1, and the SFP properties are listed in Table 4.2. These values were input into Eqns. 4.3-4.6 to calculate the theoretical ratio for Model I and Model II. No uncertainty was provided for three gamma-ray

yields as noted in Table 4.2, so the associated uncertainty was assumed to be zero. Initial activity ratios of ^{250}Cf to ^{252}Cf are listed in Table 4.3 for sources A–C. The initial activity ratios were calculated for sources A–C by converting atom or weight percent isotopic values on the TDS to activity percent. The isotopic ratios were decay-corrected from the mass analysis date to the date of last ^{248}Cm separation. TDS were unavailable for sources D and E, so the initial activity ratios are the average value of sources A–C. Two SFP, ^{136}I and ^{138}Cs, had metastable isomers with SFP yields greater than 10% of the ground isomer SFP yield from at least one spontaneous fission nuclide. The model was modified to account for this phenomenon by individually calculating the gamma-ray emission rate from each isomer for each spontaneous fission nuclide using Eqns. 4.3, 4.4, and 4.6. The gamma-ray emission rate from each isomer was then added together to calculate the total gamma-ray emission rate for the isotope. This value was then entered into the denominator of Eqns. 4.7 and 4.8 to calculate source age.

Table 4.1: Properties of spontaneous fission nuclides present in a ^{252}Cf source. Uncertainties are in parentheses and represent 1-σ.

Isotope	Half-life [y]	Probability of Spontaneous Fission [%]	Avg. Neutrons/Fission [87]
^{252}Cf [73]	2.645(8)	3.092(8)	3.77
^{250}Cf [75]	13.08(9)	0.077(3)	3.53
^{248}Cm [76]	$3.48{\cdot}10^{5}$(6)	8.39(16)	3.11

Table 4.2: Properties of ^{252}Cf fission products used for age dating an unknown ^{252}Cf source. Uncertainties are in parentheses and represent 1-σ.

Isotope	Energy [keV]	Half-life	Gamma-Ray Yield	SFP Yield [atoms/fission] [1]		
			[γ/decay]	^{252}Cf Yield	^{250}Cf Yield	^{248}Cm Yield
^{137}Cs [82]	661.657(3)	30.08(9) y	0.851(2)	0.0502(20)	0.0545(125)	0.0608(36)
^{132}I [88]	667.714(2)	2.295(13) h	0.987*	0.0215(137)	0.0245(157)	0.0433(278)
^{136}I [89]	1313.02(10)	83.4(4) s	0.667*	0.0228(53)	0.0176(41)	0.0288(46)
^{136m}I [89]	1313.02(10)	46.6(11) s	1*	0.00939(422)	0.0131(30)	0.0127(29)
^{138}Cs [90]	1435.77(7)	32.5(2) m	0.763(5)	0.0547(15)	0.0555(89)	0.0650(103)
^{138m}Cs [90]	1436.0(2)	2.91(10) m	0.19(3)	0.00301(192)	0.00591(266)	0.00146(94)
^{140}La [91]	1596.21(4)	1.67855(12) d	0.9540(8)	0.0596(8)	0.0525(31)	0.0582(35)

*No uncertainty provided

Table 4.3: Initial activity ratios of ^{250}Cf to ^{250}Cf at time since ^{248}Cm separation and neutron emission rates at time of high-resolution gamma-ray spectroscopy measurements. Initial activity ratios were calculated using isotopic analyses reported on the TDS for sources A–C. TDS for sources D and E were unavailable, so values reported are the average ratios of sources A–C.

Variable	Source				
	A	B	C	D	E
$A_0(^{250}\text{Cf})/A_0(^{252}\text{Cf})$	0.0304	0.0217	0.0312	0.0278	0.0278
Neutron Emission Rate [n·s^{-1}]	$2.46{\cdot}10^5$	$2.12{\cdot}10^5$	$9.18{\cdot}10^4$		

Experimental emission rate ratios were calculated using Eqn. 4.2. Count rate data is listed in Appendix A. Relative detection efficiency accounted for differences in detector response to varying gamma-ray energies with respect to the 661.657 keV gamma ray from ^{137}Cs and was derived from absolute full-energy peak efficiency. Full-width-at-half-maximum (FWHM) was 1.67 keV at 122 keV and 3.08 keV at 1408 keV. The gamma-ray peaks were Gaussian in shape and low energy tailing was not present. Although the energy resolution for this detector was degraded, the detector was deemed fit-for-purpose, because the methodology employed here was not identifying and quantifying many overlapping peaks and thus did not require superb energy resolution. The absolute full-energy peak efficiency for each peak was calculated using Eqn. 4.1. A power fit was applied to the seven data points to create an absolute detection efficiency curve as shown in Fig. 4.2. The fit was within the uncertainty of all data points and was determined to be a good fit. The power fit was then normalized to the absolute efficiency value at 661.657 keV to create the relative detection efficiency curve. Note that the relative efficiency curve is applicable for sources placed at varying distances with no added absorbers between the source and detector. The detector response of one gamma-ray energy relative to a second

gamma-ray energy will remain approximately constant with changing distance over the energy range considered; only the source intensity changes with distance. The attenuation in the ^{152}Eu source was negligible over the energy range of interest and approximately canceled when the relative efficiency curve was formed.

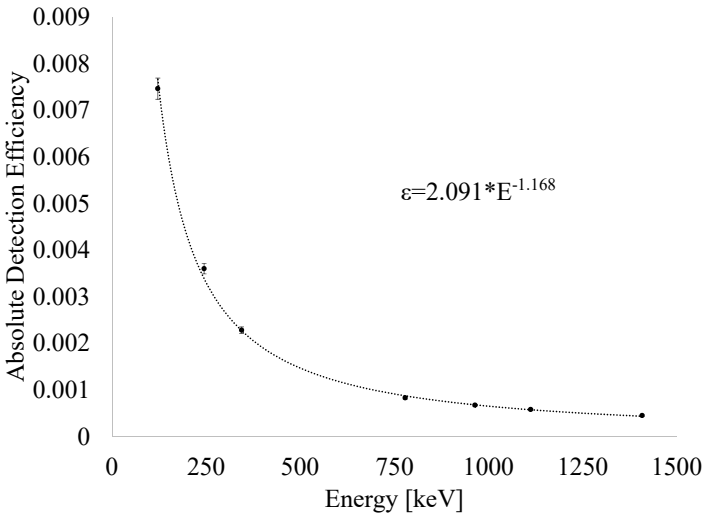

Figure 4.2: Absolute efficiency curve constructed from a ^{152}Eu calibration source.

The calculated age and associated uncertainty of each source using Models I and II are displayed in Table 4.4 for each SFP and the average age from all SFP. Average source age represents the weighted average and associated weighted uncertainty [92]. The calculated source ages from ^{132}I and ^{136}I were consistently below the source ages for ^{138}Cs and ^{140}La. The methodology employed here was strongly dependent on the quality of the nuclear data available. A systematic bias likely exists in the data for ^{132}I and ^{136}I that was carried through in this calculation. However, all individual SFP source ages were within two standard deviations of each other for each source. The agreement among different SFP indicates that this is a robust method for calculating

source age of a ^{252}Cf source.

Table 4.4: Calculated source ages of ^{252}Cf sources with associated uncertainty. Uncertainty represents 1-σ.

	Isotope, x	Source Age [y]				
		A	B	C	D	E
Model I	^{136}I	12.2±0.9	14.5±0.9	24.2±1.0	29.6 ±1.0	33.0±1.0
	^{138}Cs	14.7±0.3	16.2±0.2	25.8±0.2	31.6 ±0.3	35.1±0.2
	^{140}La	14.4±0.5	16.1±0.3	25.7±0.2	31.6 ±0.2	35.1±0.2
	^{132}I	11.8±2.9	14.6±3.0	24.3±3.2	28.6±3.2	33.1±3.2
	Average	14.4±0.3	16.1±0.2	25.7±0.2	31.5±0.2	35.0±0.2
Model II	^{136}I	12.1±0.9	14.6±0.9	24.7±1.0	31.6±1.1	38.9±1.7
	^{138}Cs	14.7±0.3	16.2±0.2	26.7±0.3	35.2±0.8	53.0±14.1
	^{140}La	14.4±0.5	16.1±0.3	26.4±0.3	34.4±0.4	45.8±2.1
	^{132}I	11.9±2.9	14.7±3.0	25.0±3.1	30.5±3.3	42.7±16.0
	Average	14.4±0.3	16.1±0.2	26.4±0.2	34.2±0.4	41.7±1.3

Comparing source ages between Models I and II for the same source demonstrates the importance of accounting for contributions from secondary neutron emitters for older sources. Both models are in statistical agreement at the 1-σ limit for sources A and B, indicating that the sources are dominated by ^{252}Cf spontaneous fission and the contributions from ^{250}Cf and ^{248}Cm are negligible. The calculated source ages of source C for Models I and II statistically agree at the 2-σ limit, suggesting that ^{252}Cf is still the dominant neutron emitter in the source, but contributions from ^{250}Cf are beginning to affect source characteristics and should be accounted for. This result is not surprising as ^{250}Cf accounts for about 11% of the neutron yield for this source at its estimated age. An increase in ^{250}Cf neutron yield proportionately affects

the SFP in-growth contributions from ^{250}Cf. Models I and II are statistically different at the 3-σ limit for sources D and E, so ^{250}Cf and ^{248}Cm contributions are no longer negligible for these sources. Source D is at approximately the age that ^{250}Cf neutron yield is greater than or equal to the ^{252}Cf neutron yield, and source E is at approximately the age that ^{248}Cm neutron yield is greater than or equal to the ^{252}Cf neutron yield [74]. Consequently, the assumptions for Model I are not valid for sources D and E as the SFP in-growth contributions from ^{250}Cf and ^{248}Cm are not negligible. Model II is ultimately more appropriate for calculating ^{252}Cf source age, because its underlying assumptions remain true for a wider age range of sources than Model I.

A third model, Model III, was considered that accounted only for SFP in-growth from ^{252}Cf and ^{250}Cf and assumed SFP in-growth from ^{248}Cm was negligible. The average source age was less than 0.5% different between Models II and III for sources A–C. The ^{248}Cm neutron yield was at least three orders of magnitude less than the total neutron yield from ^{252}Cf and ^{250}Cf for these sources at their calculated source ages. This translated to the SFP contribution from ^{248}Cm being proportionately smaller and negligibly affecting the calculated source when not accounted for in the model. However, the average source ages were 1.8% and 7.9% different for sources D and E, respectively, between Models II and III. Much of the ^{252}Cf has decayed away in these sources, so the ^{248}Cm SFP contributions were only one order of magnitude less than the combined ^{252}Cf and ^{250}Cf SFP contributions for source D and on the same order of magnitude as the ^{252}Cf and ^{250}Cf SFP contributions for source E. The ^{248}Cm contributions were thus not negligible. This result strengthens the argument that Model II should be used when calculating source age for ^{252}Cf sources, because its underlying assumptions hold true for a wider age range of sources.

Calculated source ages were compared to declared sources ages on the TDS for sources A–C and displayed in Fig. 4.3. Sources D and E could not be compared

to their respective TDS as they were unable to be located. Source B is the only source with a calculated source age within 1-σ of the reported source age; sources A and C are statistically different at the 3-σ limit. Previous work [80, 81] indicated that the method used here to calculate source age from the gamma-ray spectrum should reproduce the source age provided on the technical data, which means that the observed discrepancy is likely the result of a problem with the source, the provided TDS, or the assumptions for calculating source age.

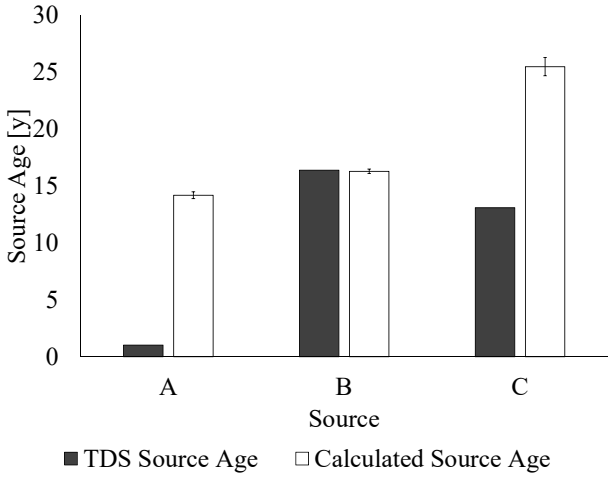

Figure 4.3: Comparison of the source age listed on the ^{252}Cf TDS and measured values from high-resolution gamma spectroscopy.

An unidentified impurity or contaminant in the source was investigated as a possible cause of the severely overestimated source age. Cesium-137 is the isotope in the numerator of both experimental and theoretical ratios for calculating source age and is consequently the only isotope that could cause an overestimation in source age. It is also the only SFP used in the source age calculation with a long enough half-life to appear as an impurity or contaminant in the source; all short-lived SFP used in this calculation would have decayed away shortly after source fabrication. For ^{137}Cs to exist as an impurity or contaminant in a ^{252}Cf source, either radiochemical processing

did not fully separate Cs from Cf or the fabrication laboratory was contaminated with ^{137}Cs. Actinides, such as Cf, are readily separated from alkali metals, such as cesium, via the ion exchange process used at the Radiochemical Engineering Development Center (REDC) at ORNL, making the first scenario unlikely [93]. The second scenario is also unlikely because these facilities are regularly tested for contamination. Any ^{137}Cs contamination would be quickly identified in the work area so that a source could not leave the facility contaminated with ^{137}Cs. Additionally, the vendors of both sources stated that they either do not work with cesium or only work with cesium in facilities located in a different building to the ^{252}Cf source fabrication facilities. Ultimately, there are no means for ^{137}Cs to be present as an impurity or contaminant in the sources, so it must have grown into the source as a fission product from the three spontaneous fission nuclides present in the source.

Another possible explanation for the source age discrepancy was that the vendors did not send the correct TDS with the source when purchased. Note that sources B and C were fabricated by the same vendor, and source A was fabricated by a different vendor. The vendor that fabricated source A confirmed that the correct TDS was sent with the source. The vendor that fabricated source C supplied another TDS for source C that statistically agreed at the 2-σ limit with the calculated source age and isotopic ratios. However, the vendor also noted that source C was fabricated from depleted source inventory and could contain source material from different batches, so a single TDS might not accurately represent the source material. Additionally, the vendor later noted that the source material did not come from the batch associated with the newly provided TDS but did not provide information about the specific batch or batches that the material came from. It was ultimately not conclusive if the correct TDS was supplied for source C.

The final possible explanation was that the assumptions for calculating source

age did not hold true. The assumptions for this work presumed that the vendors did not perform any radiochemical processing on the source material and that they created ^{252}Cf sources using the chemical form that the REDC at ORNL sent the material in. However, the vendor that fabricated source A revealed that the Pd wire that the Cf source material is shipped in was dissolved and the Pd extracted using an ion exchange resin prior to source fabrication. This radiochemical process could thus disrupt the contents of the material, resulting in an incorrectly calculated source age based on invalid assumptions.

4.3.2 Nuclear Data Uncertainty Evaluation

The individual source age values in Table 4.4 demonstrate that certain short-lived SFPs produce source age estimates with less uncertainty than others. Lanthanum-140 has the smallest source age uncertainties for Models I and II and ^{132}I has the largest uncertainties. This is a direct result of the magnitude of the uncertainties associated with the SFP yield for these two isotopes. As shown in Table 4.2, ^{140}La has SFP yield uncertainties that are between 1.3% and 6.0% for all spontaneous fission nuclides, whereas ^{132}I has SFP yield uncertainties that are approximately 64% for all spontaneous fission nuclides. These uncertainties ultimately drive the quality of the final source age uncertainties.

Similarly, the source age uncertainty for sources D and E increases dramatically from Model I to Model II but remains consistent for sources A–C. This stems from the 23% uncertainty associated with the ^{137}Cs SFP yield from ^{250}Cf compared to the 4–6% uncertainty associated with the ^{137}Cs SFP yield from ^{252}Cf and ^{248}Cm. Sources D and E are affected by this large uncertainty more than sources A–C, because the ^{250}Cf contributions are no longer negligible. Older sources will thus always have

higher uncertainty when implementing Model II because of the poorer quality of the currently available nuclear data for the ^{137}Cs SFP yield from ^{250}Cf.

Quality nuclear data are essential for obtaining a source age measurement with low uncertainty. The limiting variable in these cases was the SFP yields, but it could be other variables for different isotopes. Currently, great care should be taken when choosing SFP for calculating ^{252}Cf source age. However, the nuclear data used for this work could be improved using the CARIBU beam at the ATLAS facility at Argonne National Laboratory [94]. Specifically, SFP yields could be obtained with improved uncertainty using an ion counting method along a beam of each SFP of interest.

4.3.3 Isotopic Ratios

Californium-250 and ^{252}Cf emit low-energy gamma rays (<210 keV) with low probability of emission (<0.0002 emissions/decay) [73, 75]. These gamma rays are obscured in the gamma-ray spectrum by the gamma rays emitted from SFP and thus cannot be directly measured via gamma-ray spectroscopy to confirm their isotopic composition in a source. However, isotopic analyses on the TDS provide information about the $^{249-254}$Cf isotopes relative to each other. Highly probable gamma rays emitted from the decay of long-lived, odd-numbered californium isotopes, ^{249}Cf and ^{251}Cf, can be exploited to verify isotopic information provided on the TDS for all californium isotopes, including ^{250}Cf and ^{252}Cf.

The 388.17 keV gamma ray from ^{249}Cf and 177.52 keV gamma ray from ^{251}Cf were used to compare the ratio of ^{249}Cf to ^{251}Cf from experimental data to the TDS. The experimental ratio, R_{data}, was calculated by

$$R_{data} = \frac{CR_{\text{Cf-249}}(388.17\text{ keV}) \cdot \epsilon_{rel}(177.52\text{ keV}) \cdot I_{\text{Cf-249}}}{CR_{\text{Cf-251}}(177.52\text{ keV}) \cdot \epsilon_{rel}(388.17\text{ keV}) \cdot I_{\text{Cf-249}}} \tag{4.11}$$

where $CR_{\text{Cf-249}}(388\text{ keV})$ and $CR_{\text{Cf-251}}(177\text{ keV})$ are the net count rates in the 388.17 keV gamma-ray full-energy peak peak from ^{249}Cf and the 177.52 keV gamma-ray full-energy peak peak from ^{251}Cf, respectively, and $I_{\text{Cf-249}}$ and $I_{\text{Cf-251}}$ are the gamma-ray yields of the respective gamma rays emitted by each isotope. The net count rates, included in Appendix A, are corrected for capsule attenuation. The ratio from the TDS data was obtained by dividing the isotopic activity percent of ^{249}Cf to the isotopic activity percent of ^{251}Cf. These values were decay corrected from the isotopic analysis date to the measurement date, but the correction was negligible because both isotopes have long half-lives.

Figure 4.4 displays the ^{249}Cf/^{251}Cf ratios calculated from experimental data and TDS values. Source B was the only source that had an experimental ^{249}Cf/^{251}Cf ratio that agreed with the isotopic ratio reported on the TDS at the 1-σ limit. Sources A and C had experimental and TDS ratios that were statistically different at the 3-σ limit. However, no pathway exists, other than radioactive decay, for the quantity of these isotopes to change from the initial reported quantity. Californium-249 is created via multiple successive neutron captures in ^{248}Cm or a single neutron capture in ^{249}Bk, and ^{251}Cf is created via multiple successive neutron captures in ^{249}Cf. However, Cm and Bk are stripped from the source after irradiation in the reactor, eliminating this as a possible pathway for changes in the reported quantity of ^{249}Cf or ^{251}Cf. The quantity of ^{249}Cf and ^{251}Cf present in the source at $t = 0$ should be equal to the quantity of these isotopes present in the source at the time of measurement because ^{249}Cf and ^{251}Cf decay is negligible in that time period. Consequently, the TDS and experimental ratio should be in statistical agreement. The possible explanations for this discrepancy were the same as the discrepancies for the source age: either the incorrect TDS was provided for the source or the assumptions for the calculation were invalid because the source material contents were disrupted during radiochemical

processing for source fabrication.

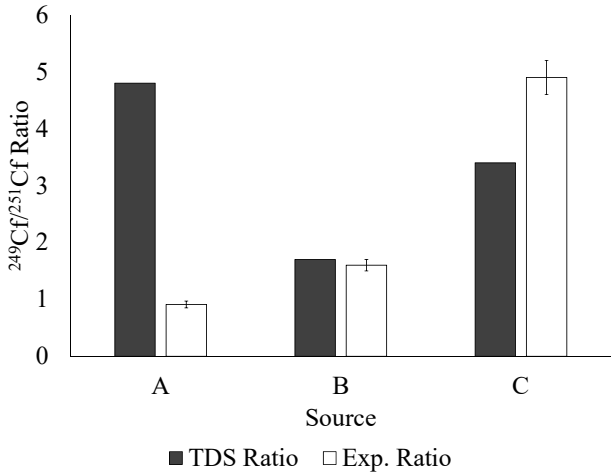

Figure 4.4: Comparison of ^{249}Cf/^{251}Cf ratios calculated from experimental data and the TDS.

4.4 Conclusions

Source age and isotopic data are needed to make accurate decay corrections inclusive of the ^{250}Cf contribution to the neutron yield for calibrating a passive neutron correlation counting system. The present work demonstrated the utility of performing gamma spectroscopy on ^{252}Cf sources to estimate source age. Analysis results from all four SFP used for calculating source age returned statistically similar source ages at the 2-σ limit for Models I and II despite large nominal uncertainties in some SFP yields. Statistical differences in the average source age between Models I and II, however, illustrate the importance of accounting for secondary neutron emitters, ^{250}Cf and ^{248}Cm, when estimating source age using gamma-ray spectroscopy.

Comparing the experimental data to declared values on the TDS for sources A–C revealed discrepancies between the values. Source age and isotopic ratio experimental data for source B were within 1-σ of the values reported on the TDS,

bolstering the claim from previous work [80, 81] that this method has the potential to produce accurate results. However, sources A and C had statistically different source age and isotopic ratio values at 3-σ, suggesting that either an impurity or contamination was present in the source, the TDS did not match the source, or the assumptions for calculating source age and isotopic ratios were invalid. The possibility of an impurity or contamination in the source was eliminated, but the remaining possible explanations for this discrepancy could not be eliminated. However, regardless of the explanation for the discrepancy, the disagreement between source age and isotopic ratios on the TDS and experimental calculations still affects the user's ability to confidently calibrate a passive neutron correlation counter, because accurate source age and isotopic information is needed for decay corrections. It is thus strongly recommended to independently verify the content of ^{252}Cf calibration sources used for passive neutron correlation counting prior to use, and this method can be employed with high accuracy to confirm or query declared values on a TDS for a ^{252}Cf source.

The discrepancies revealed here regarding source age and isotopic ratio did not, however, explain the discrepancy between the doubles-to-singles ratios of ^{252}Cf sources used at ORNL for calibrating neutron counters for nuclear safeguards instrumentation, which is what originally inspired this work. Using nuclear data, the theoretical ratio of the second neutron moment to the first neutron moment squared decreased by only 0.3% at 25 y compared to the initial ratio at source fabrication. In comparison, the experimentally determined ratio of the doubles rate to the square of the singles rate is about 55% different for the sources in question and thus cannot be explained by incorrect source age data. The discrepancy could be explained by unidentified impurities in the source that are adding (α, n) neutrons to the singles rate. The (α, n) reaction occurs when a light element, such as O, is intimately mixed with an actinide that decays via α particle emission. The α particle is then absorbed

by the light element and emits a neutron. The added neutrons from this reaction could explain the discrepancy between the doubles-to-singles ratio and not be identified in a gamma-ray spectrum. Although (α, n) reaction gamma rays are possible, their emission probabilities are commonly low and would likely be overshadowed by the SFP gamma rays. Identification of (α, n) impurities could possibly be accomplished by neutron spectroscopy but will likely require destructive analysis techniques for definitive identification and quantification. Further work is ultimately required to explain this discrepancy between sources.

Chapter 5

Unfolding Neutron Energy Spectra Using Concentric Rings of Moderated ^{3}He Counters

Abstract

The inverse Bonner sphere concept was developed into a novel neutron spectrometer for measuring neutron energy spectra in international safeguards. The concept was initially proposed as an in-situ technique to characterize AmLi sources used in active neutron interrogation techniques. In this method, the source was centrally placed in cylindrical moderators with incrementally increasing diameters and then centered in the large volume active well coincidence counter cavity, operated in passive mode, to surround it by two concentric rings of 48 moderated ^{3}He proportional counters. MCNP simulations were used in this work to simulate the inverse Bonner sphere spectrometer. Californium-252, ^{241}AmLi, and ^{241}AmBe neutron sources. The sources were surrounded by high density polyethylene cylinders to moderate neutrons. The

cylinder diameters were incrementally increased by 1 cm between 0–12 cm to elicit a change the response functions for the unfolding procedure. Response functions were created in MCNP using monoenergetic neutrons between 0.1–14 MeV. The MAXED and GRAVEL algorithms were used to unfold the neutron energy spectra. Proof-of-concept was demonstrated using well-characterized response functions and input guess spectra. Sensitivity studies were then performed for the response functions, the quantity of *a priori* information in the input guess spectra, and impurities in AmLi sources.

5.1 Introduction

Active neutron coincidence counting is an established non-destructive assay (NDA) method implemented by the IAEA to measure the mass of ^{235}U in an item [7]. AmLi neutron sources induce fission in ^{235}U and the resulting number of fissions registered by the neutron counter is related to the mass of ^{235}U via a system calibration. Although a system calibration has traditionally been based on the response to representative standards, simulation-based system calibrations are becoming more commonplace in international safeguards due to the difficulty of obtaining representative standards for complex geometries, such as a fuel assembly. However, biases may be introduced into the system when deriving the system calibration in this manner. An ongoing debate in the literature exists regarding an accurate representation of the neutron spectrum for AmLi [2, 3, 10–12]. A method is needed to establish an accepted neutron energy spectrum not only for the AmLi (α, n) reaction, but for other (α, n) reactions pertinent to international safeguards.

The inverse Bonner sphere spectrometer (iBSS), which was initially proposed as an in-situ technique to characterize AmLi sources installed in neutron collars and

first demonstrated for AmLi sources, with ^{252}Cf as a monitor using a large volume active well coincidence counter (LVAWCC), could be used as a tool to experimentally measure (α, n) neutron energy spectra pertinent to international safeguards [13]. The concept of the standard Bonner sphere spectrometer (BSS), which was initially reported by [14], measured the neutron energy spectrum by placing spherical moderators with increasing diameters centrally around a thermal neutron sensor, specifically a LiI scintillator in this case. Doing so changed the response function such that the peak (i.e. the optimal neutron energy for detection) shifted towards higher energies with increasing moderator diameter. The BSS can measure neutron energy spectra across a wide range of energies from thermal to GeV neutrons depending on the size of the moderators [40]. The BSS has been recreated using several moderator shapes, namely spherical and cylindrical, and a variety of thermal neutron sensors, including BF_3 and ^{3}He [44–49, 95]. In contrast to the standard BSS method, the source, not the thermal neutron detector, was placed spherical or cylindrical moderators with incrementally increasing diameters in the iBSS method. The source and moderator were then centered radially and longitudinally in the LVAWCC cavity such that they were surrounded by two concentric rings of moderated ^{3}He proportional counters. Each ring of ^{3}He counters acted as a single counter, and the ring ratios provided additional insight. Previous published work on the inverse Bonner sphere concept considered which of a number of plausible AmLi spectrum representations most closely reproduced the experimental data, but did not perform explicit neutron energy spectrum unfolding [13]. The work presented here builds upon previous work [13] to develop the inverse Bonner sphere concept into a novel neutron spectrometer, referred to as the iBSS. Proof-of-concept for the iBSS was developed using simulated ^{252}Cf, ^{241}AmLi, and ^{241}AmBe neutron sources in an MCNP model of the LVAWCC. Sensitivity studies were then performed for the response functions, quantity of *a priori* information in

the input guess spectra, and impurities in AmLi sources.

5.2 Methods

5.2.1 MCNP Simulations

Computer simulations were run in MCNP 6.2 [28]. An MCNP model of the LVAWCC was used to simulate measurements of ^{252}Cf, ^{241}AmLi, and ^{241}AmBe neutron sources surrounded by cylindrical HDPE moderators with varying wall thicknesses. The LVAWCC model in MCNP replicated the physical system. A depiction of the cross section of the model with a ^{252}Cf source and HDPE cylinder inside the cavity is illustrated in Fig. 5.1. The cavity had a diameter of 27.9 cm and a height of 38.1 cm and was surrounded by two concentric rings of 48 ^{3}He-filled cylindrical proportional counters embedded in HDPE; each ring had 24 counters spaced equally around the cavity. The proportional counters had a 2.54 cm outer diameter and 0.508 mm steel wall thickness, had an active length of 63.5 cm, and were filled with ^{3}He to a pressure of 4.5 atm at 25°C with an Ar quench gas. The detectors were embedded in HDPE (ρ = 0.95 g/cm^3) to moderate neutrons for optimal detection by the ^{3}He (n,p) reaction.

Each simulated neutron source corresponded to a physical source available in the laboratory. Californium-252 was modeled in a Frontier Technology Corporation Model 10S capsule. The source material was assumed to consist only of ^{252}Cf (ρ = 15.1 g/cm^3), because ^{252}Cf calibration sources are dominated by neutrons emitted from ^{252}Cf with negligible contributions from other isotopes or elements. Neutrons were simulated as originating from a point in the center of the source material, because ^{252}Cf sources are compact neutron sources that are often assumed to approximate

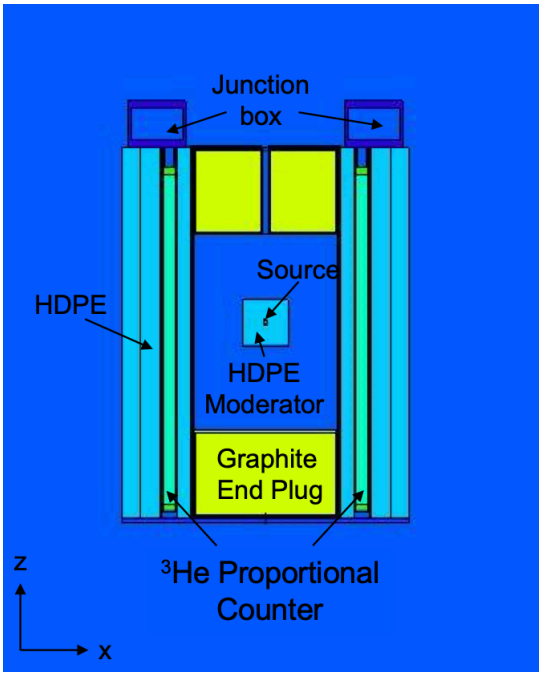

Figure 5.1: Cross section of the LVAWCC MCNP model in the x-z plane

to a point, which eliminates other potential source effects, such as self-multiplication and moderation. Spontaneous fission neutrons from ^{252}Cf were modeled using the Watt spectrum with parameters $a = 1.025$ and $b = 2.926$ [28].

AmLi was modeled in a Gammatron C-series capsule inside of a tungsten pot. The tungsten pot had outer dimensions of 5.73 cm in diameter and 4.31 cm in height and inner dimensions of 2.68 cm in diameter and 3.17 cm in height. Because the composition of AmLi source material is generally not well documented, a general source mixture (ρ=1.6 g/cm^3) was used of LiOH and AmO_2 with a ^{7}Li/^{241}Am atom ratio of 263 to 1 [11]. Neutron were uniformly sampled from the cell containing the source material. SOURCES-4C was used to create the neutron energy spectrum for the general source mixture and included neutron emission contributions from ^{6}Li(α,n) and ^{17,18}O(α,n) [8].

AmBe was modeled in an Eckert & Ziegler Am1.N02 capsule. The source

material (ρ=1.3 g/cm^3) was mixture of AmO_2 and Be with a ^{9}Be/^{241}Am ratio of 9.8 [96, 97]. Neutrons were uniformly sampled from the cell containing the source material in the same manner as the AmLi source. SOURCES-4C was also used to create the neutron energy spectrum and included neutron emission contributions from ^{9}Be(α,n) and ^{17,18}O(α,n) [8].

Each neutron source was centrally placed inside of HDPE cylindrical moderators ($\rho = 0.95$ g/cm^3). Cylindrical moderators were chosen for this work instead of spherical moderators because a cylinder matches the geometry of the neutron sources and LVAWCC cavity used in this work. The wall thickness of the cylindrical moderator was modeled to be equal radially and longitudinally surrounding the source, as shown in Fig. 5.2 by the variable x. The diameter of the cylindrical moderator was then equal to twice the wall thickness plus the diameter of the source capsule, and the height of the cylindrical moderator was then equal to twice the wall thickness plus the height of the source capsule. The moderator wall thicknesses were incrementally increased by 1 cm between 1–12 cm for ^{252}Cf and AmBe and 1–11 cm for AmLi; the diameter of the LVAWCC cavity limited the overall diameter of the moderators. The bare source with no moderator present was also simulated.

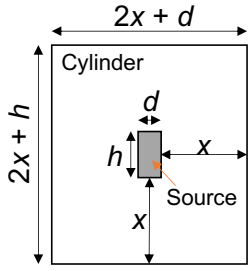

Figure 5.2: Cylinder depiction

Only neutron transport was considered in this work; photon transport was ignored because ^{3}He proportional counters discriminate gamma rays well. An F4

tally—the averaged track length in a volume divided by the volume—was used to average the flux over the cells representing the active length of ^{3}He proportional counters. This was combined with a tally multiplier to account for the ^{3}He(n,p) reaction rate using the ENDF70 cross section library in MCNP [98]. In a physical sense, the tally and multiplier together represent the number of neutrons that produce an electrical pulse and results in a neutron detection. Tallies were collected for the inner ring counters and outer ring counters separately. One million neutron histories were run for each MCNP input file to ensure the statistical uncertainties were below 1%.

5.2.2 Unfolding Algorithms

The "few channel" versions of the MAXED (MAXimum Entropy Deconvolution) and GRAVEL algorithms, which were written for BSS with thermal neutron detectors, were used to unfold the neutron energy spectra in this work. MAXED is based on the maximum entropy principle, which requires the best solution to have the largest entropy to reduce errors and biases in the unfolding [61]. GRAVEL is a modification of the SAND-II algorithm and is based on non-linear least squares regression [61]. The codes were run using the suggested input parameters for a BSS system [60]. The data input into the algorithm were the same for both algorithms and included the simulated data and associated uncertainties, an initial guess spectrum, and the response functions. The algorithms required the data to be input as counts or count rate and the uncertainty to be separated into counting statistics and other sources of uncertainty. Within the algorithm, the two uncertainty categories were added in quadrature. For the simulated data in this work, the simulated counts were

calculated from the MCNP F4 tally as

$$M_d = (F4)_d \cdot V \cdot H \tag{5.1}$$

where $(F4)_d$ is the results of the F4 tally for each moderator and ring combination, V is ^{3}He active length cell volume in each ring, and H is the total number of neutron histories. The counts were then entered into the algorithm separately for each ring and source and moderator combination. Uncertainty due to counting statistics was the square root of the number of counts. Other sources of uncertainty (e.g. systematic uncertainty) were estimated to be 1% for ^{252}Cf and AmBe to cover uncertainty from source assay and nuclear data. For AmLi, other sources of uncertainty were increased to 3% for the added uncertainty in source composition.

Different input guess spectra were used for each neutron source to test the sensitivity of the algorithms. Each spectrum contained varying amounts of *a priori* information, but each was chosen such that the energy range was a positive, smooth function between 0–14 MeV and zero outside of this energy range. This energy range was chosen, because it covers the likely energy range of typical neutron emitters in international safeguards. The first input guess spectrum for was the neutron energy spectrum input into MCNP for each respective neutron source, as described in the previous section, to test if the algorithm could unfold the spectrum given the correct solution. A uniform spectrum was also used to test the sensitivity of the iBSS to the quality and quantity of *a priori* information included in the input guess spectrum. The uniform spectrum provided no information about the shape of the resultant spectrum; it simply contained information about the expected energy range of the resultant spectrum.

The response functions were simulated in MCNP for each neutron source and

moderator combination described above. Monoenergetic neutrons were emitted from each source in 0.1 MeV increments from 0.1–14 MeV. Additional energy bins were included for the AmLi response functions in 0.05 MeV increments between 0–2 MeV due to the soft neutron spectrum of that source. Neutrons were emitted from a point in the center of the source material for ^{252}Cf and from the source material volume for the AmLi and AmBe sources. Separate response functions were created for each ring of ^{3}He proportional counters.

5.3 Results and Discussion

Californium-252, AmBe, and AmLi neutron energy spectra were unfolded in the MAXED and GRAVEL algorithms using simulated data generated in MCNP 6.2 using a model of the LVAWCC. These sources are surrogates for fission and (α, n) neutron spectra that are of interest in international safeguards. They represent three distinct, well-known neutron energy spectra and serve to verify the method. Simulated counting data are provided in Appendix B. Response functions for each source and moderator combination were created first in MCNP prior to unfolding neutron spectra. Proof-of-concept for the methodology was demonstrated using the ideal case wherein the input guess spectra matched the neutron energy spectrum used to generate the data and the response functions corresponded to the neutron source. Since the ideal case is not always possible, non-ideal scenarios were explored to test the sensitivity of the algorithms, including sensitivity to the response functions and sensitivity to the *a priori* information available in the input guess spectrum.

5.3.1 Response Functions

Response functions were created in MCNP for each source and HDPE cylinder configuration. Separate response functions were required for the inner and outer ring of ^{3}He proportional counters in the LVAWCC, because each ring of counters operated as an individual counter and required separate input to the unfolding algorithm. The response values were calculated by dividing the simulated counts by the total neutron histories to calculate the efficiency, and then multiplying the efficiency values estimated in MCNP by the surface area of the LVAWCC cavity. The surface area of the LVAWCC cavity is the surface of interest for the neutron fluence to be calculated. The response functions are displayed for each cylinder wall thickness for the inner and outer rings, respectively, in Figs. 5.3 for the ^{252}Cf source, Figs. 5.4 for the AmBe source, and Figs. 5.5 for the AmLi source. Note that the wall thickness refers to the quantity of HDPE that surrounds the outer surface of the source and not the radius of the cylinder. The radius of the HDPE was the source radius plus the HDPE wall thickness and varies for each source.

Each response function plot has a discontinuity at approximately 3 MeV, a peak at about 6.5 MeV, and another peak between 7.5–8 MeV. All of these features are caused by the total neutron cross section of C shown in Fig. 5.6. Carbon is a large component of HDPE, so it was expected that the response functions resembled the C total cross section due to the quantity of HDPE present in this system: each source was surrounded by HDPE cylinders and both rings of ^{3}He proportional counters were embedded in HDPE. The sharp peak at approximately 2 MeV in the C total cross section did not appear in the response functions, because it occurs at an energy that was between the monoenergetic neutron energies considered in this work. In other words, the increments used to generate the response functions were not resolved

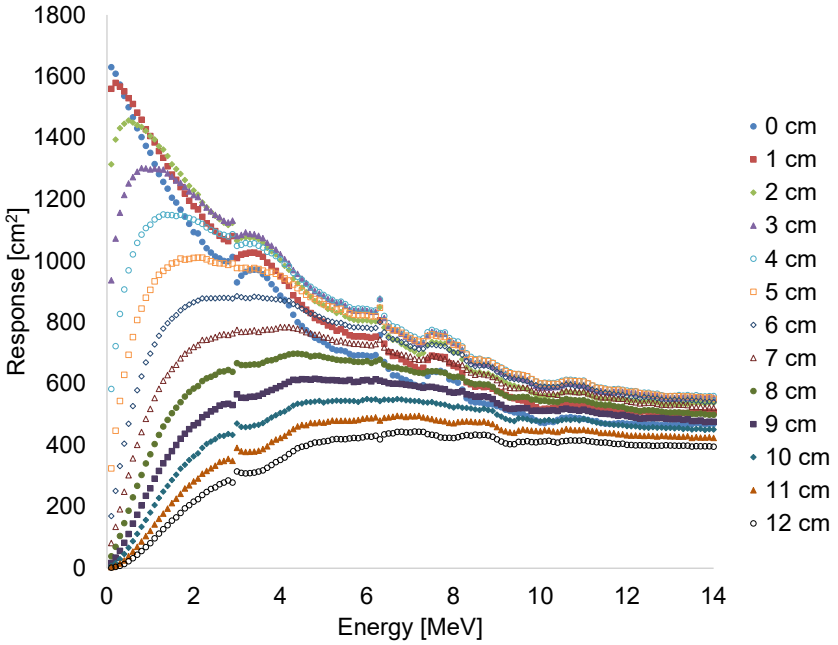

(a) Inner Ring

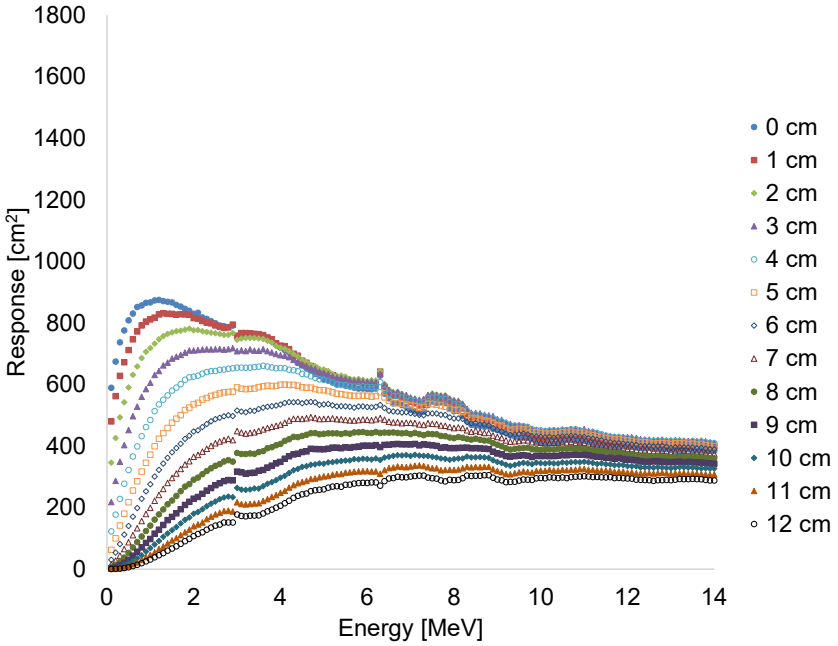

(b) Outer Ring

Figure 5.3: Response functions for ^{252}Cf neutron sources for varying wall thicknesses for the inner and outer rings of the LVAWCC

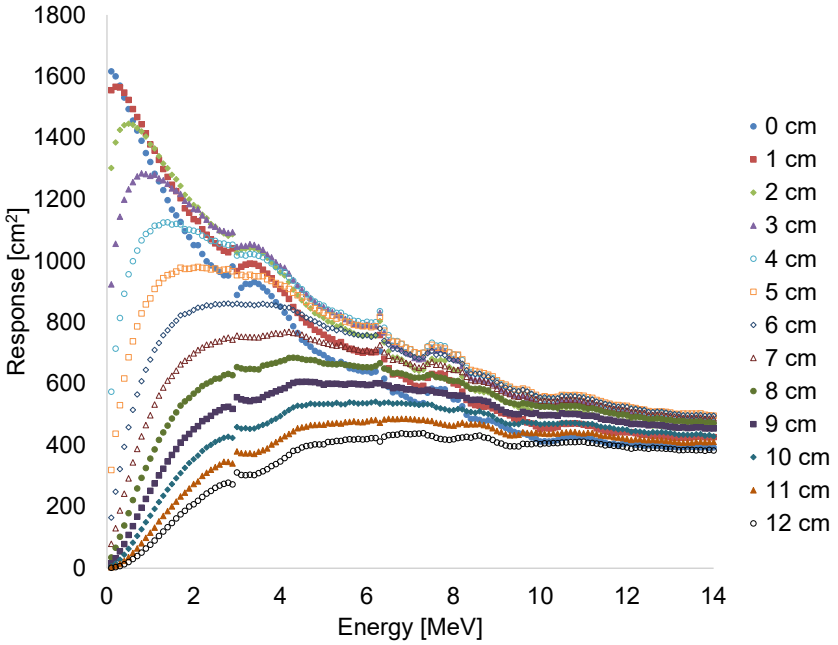

(a) Inner Ring

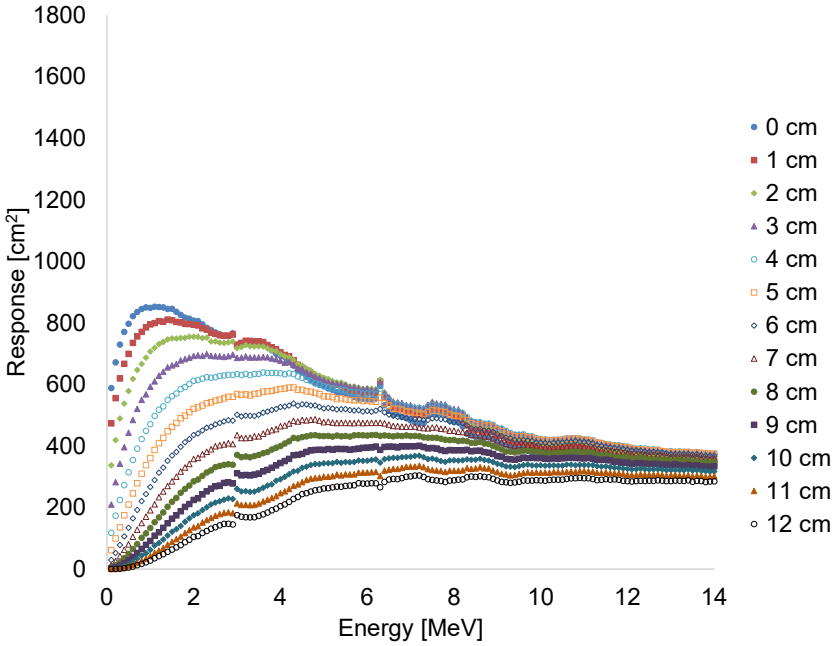

(b) Outer Ring

Figure 5.4: Response functions for AmBe neutron sources for varying wall thicknesses for the inner and outer rings of the LVAWCC

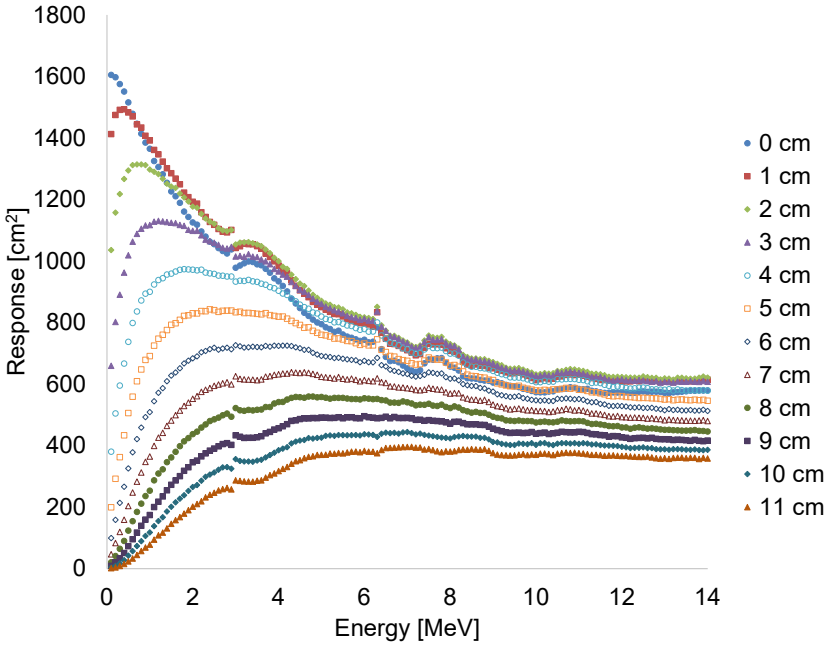

(a) Inner Ring

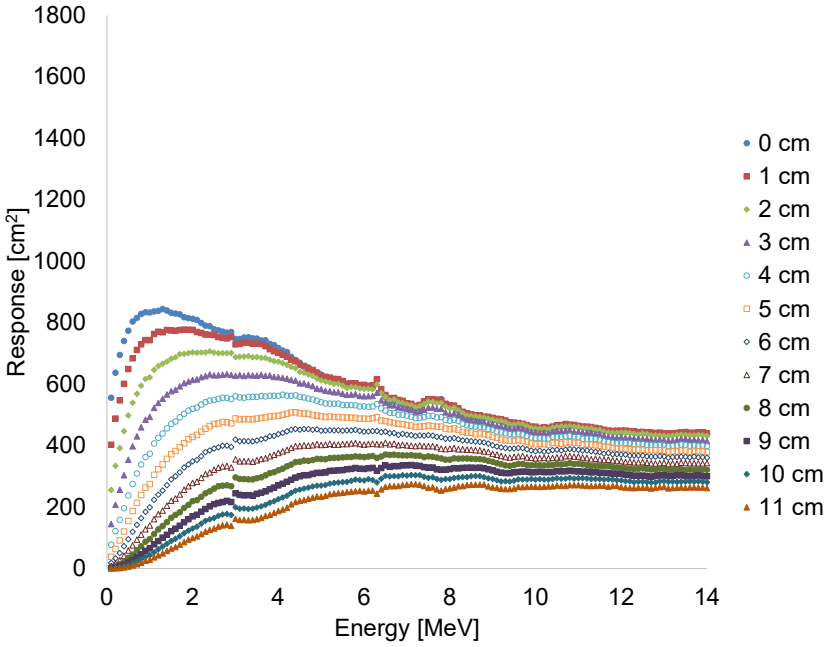

(b) Outer Ring

Figure 5.5: Response functions for AmLi neutron sources for varying wall thicknesses for the inner and outer rings of the LVAWCC

enough to capture the finer peaks in the C total cross section.

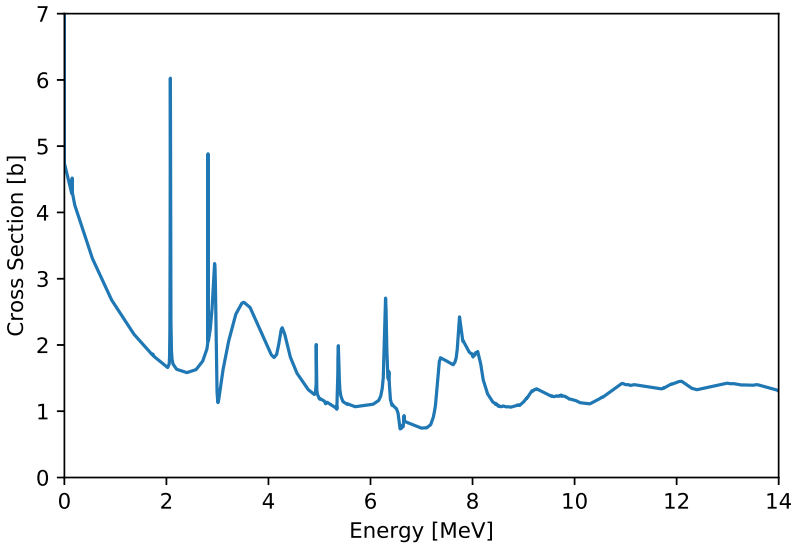

Figure 5.6: Carbon total cross section [1]

The response functions had broader peaks at higher energies and were smaller in magnitude when neutrons had to travel through greater amounts of bulk matter, and were thus subject to more neutron moderation, prior to detection. This can be observed when comparing the response functions for different wall thicknesses, counter rings, and neutron sources. The changes in response functions for different wall thicknesses and counter rings due to neutron moderation were necessary to generate an energy dependence in the measured response. Without this, the LVAWCC would have no energy dependence. However, differences between neutron sources mean that a new set of response functions should be created for each neutron source. Advances in computational codes and technology, however, provide a good resource for creating response functions for the iBSS as needed.

5.3.2 Proof-of-Concept

Proof-of-concept for the iBSS as a novel neutron spectrometer was verified by unfolding simulated ^{252}Cf spontaneous fission spectrum, ^{241}AmBe (α,n) spectrum, and ^{241}AmLi (α,n) spectrum using MAXED and GRAVEL in the ideal scenario. The input guess spectrum for each neutron source was the same neutron energy spectrum input into MCNP to generate the simulated data and thus the expected solution. For ^{252}Cf, the input guess spectrum was a Watt fission spectrum, and, for AmBe and AmLi, the input guess spectra were generated using SOURCES-4C. Three criteria were used to assess the quality of the solution spectra unfolded by MAXED and GRAVEL. The first criterion, relative error, compared the solution spectrum and expected spectrum–the neutron energy spectrum input into MCNP to generate the simulated count rate data. The relative error for each energy bin, RE_i, was calculated as

$$RE_i = \frac{|\Phi_{s,i} - \Phi_{e,i}|}{\Phi_{e,i}} \tag{5.2}$$

where $\Phi_{s,i}$ is the solution spectrum and $\Phi_{e,i}$ is the expected spectrum. The second and third criteria, reduced chi-square value and the calculated-to-measured ratio, evaluated how well the calculated count rate, obtained by folding the solution spectrum with the response functions, aligned with the measured iBSS count rates input by the user. Note that "measured count rates" here refers to the simulated count rates generated by MCNP. The reduced chi-square value, χ^2/ν, determines whether or not a statistically significant difference exists between the calculated and measured count rate based on the significance level. In this work, the significance level was set to 1% and represented the probability that the calculated and measured count rates were statistically similar but determined to be different. A two-sided chi-square test was used for this work due to the random nature of radioactive decay. The χ^2/ν 1%

significance level translated to critical value ranges of 0.421–1.88 for ^{252}Cf and AmBe, which had 25 degrees of freedom, and 0.403–1.92 for AmLi, which had 23 degrees of freedom. The degrees of freedom are equivalent to one less than the number of measured count rates entered into the algorithm, which is one less twice the number of moderators used for the measurements. The calculated-to-measured ratio, C_d/M_d, is a measure of how closely each calculated count rate compared to each corresponding measured count rate. The solution spectrum is considered to be close to the true spectrum if calculated-to-measured ratio is within 1-σ of unity for all count rate data [40]. Note that the uncertainty in the calculated-to-measured ratio is a measure of the statistical uncertainty in the measured data and not a measure of the uncertainty in the solution spectrum. Both the statistical limits for the χ^2 and calculated-to-measured ratios, which ultimately affect the solution spectrum, were set to be the most stringent limits.

The solution spectra for MAXED and GRAVEL, shown in Fig. 5.7, for ^{252}Cf, AmBe, and AmLi show high relative agreement with the expected spectrum and confirmed by the small relative error plots between the solution and expected spectra, as shown in Fig. 5.8. Note that MAXED data points not shown in plot have a relative error less than 0.0001. A threshold was set at 0.05 relative error to represent good agreement between the solution spectrum and expected spectrum and is represented by the black horizontal line on the relative error plots. The relative error was approximately zero for all three neutron emitters for MAXED. The input guess spectrum was close to the correct solution under the MAXED optimization procedure and thus required little adjustment. GRAVEL minimized the relative error at the maximum points in each neutron energy spectrum. Although the relative error was almost 0.05 towards the extreme ends of each GRAVEL solution spectrum, the values for normalized fluence rate per unit lethargy were small and approaching zero.

In both cases, the adjustment to the input guess spectrum was minimal to obtain the solution spectrum as suggested by the relative error plots. Strong agreement was also observed between the iBSS calculated and measured count rate data. The χ^2/ν values, displayed in the legends in Fig. 5.7, for all solution spectra were within the desired critical value range, and the calculated-to-measured ratios in Fig. 5.9 are also all within 1-σ of unity for ^{252}Cf, AmBe, and AmLi. This indicated that that the solution spectra are consistent with the expected neutron energy spectrum for each neutron emitter.

The possibility exists that each solution is a local minimum in the unfolding algorithms as opposed to the global minimum. This could be determined by generating a series of new measured count rate data sets. Each new data set would contain data altered from the original data set using a Poisson distribution. The new data sets would then be individually run through the algorithms to unfold the neutron energy spectra. If all unfolded spectra are statistically similar to the original solution spectra (determined by the χ^2/ν value), then it is likely that the solution spectrum was a global minimum to the problem.

The combined results presented here demonstrate proof-of-concept for the novel neutron spectrometer using the iBSS concept in the ideal scenario. However, these results do not indicate how well the algorithms adapt to the measured iBSS data when the response functions do not match the source and moderator geometry exactly or when the input guess spectrum has limited *a priori* information. This is the more likely scenario when measuring individual sources, because the spectrum is expected to vary slightly from source-to-source based on differences in the composition and microstructure of the source material. A sensitivity study for the methodology was completed for the response functions, input guess spectra with less *a priori* information, and ability to detect anomalies and impurities in a spectrum.

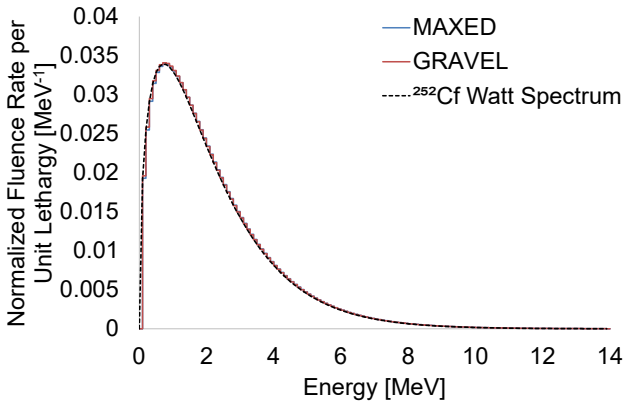

(a) ^{252}Cf

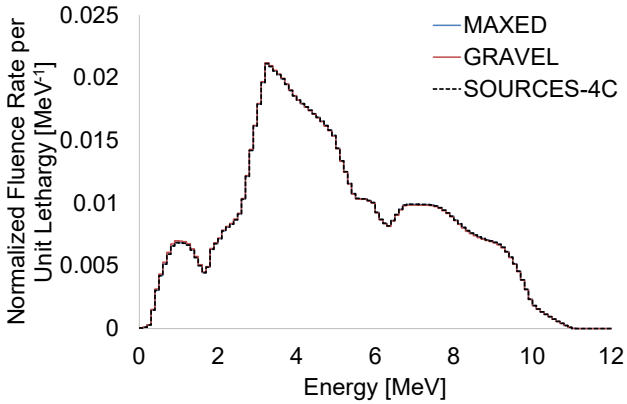

(b) AmBe

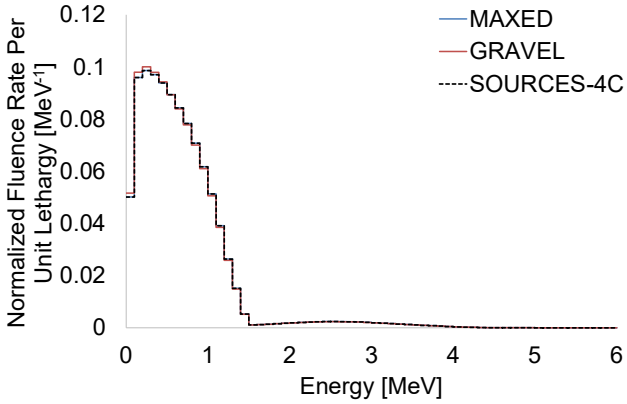

(c) AmLi

Figure 5.7: MAXED and GRAVEL solution spectra for ^{252}Cf, AmBe, and AmLi using the expected solution as the input guess spectrum

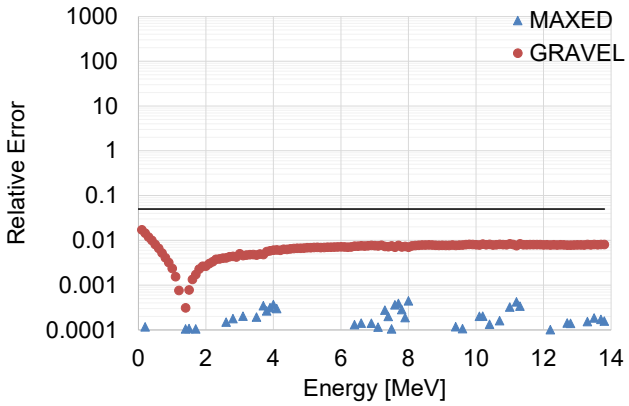

(a) ^{252}Cf

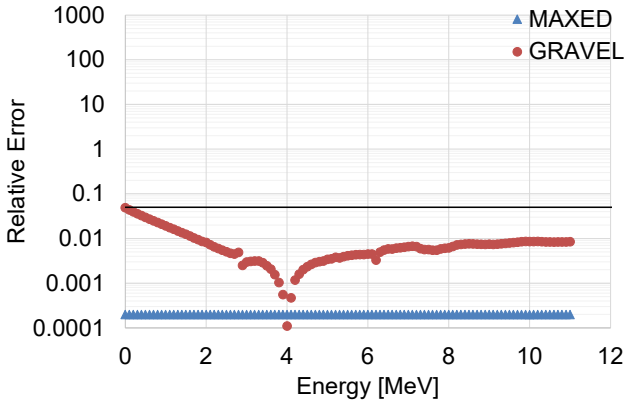

(b) AmBe

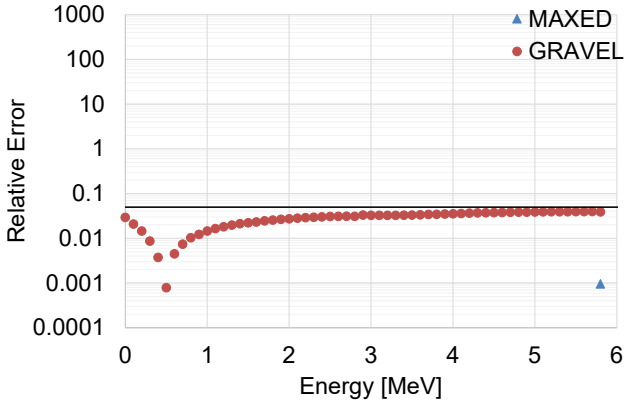

(c) AmLi

Figure 5.8: Relative error for ^{252}Cf, AmBe, and AmLi using the expected solution as the input guess spectrum. Note that MAXED data points not shown in plot have a relative error less than 0.0001.

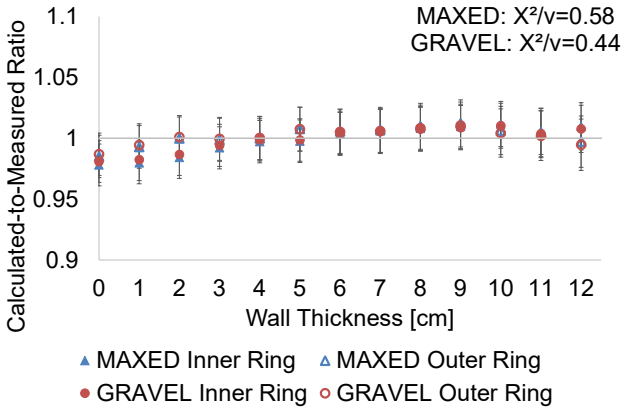

(a) ^{252}Cf

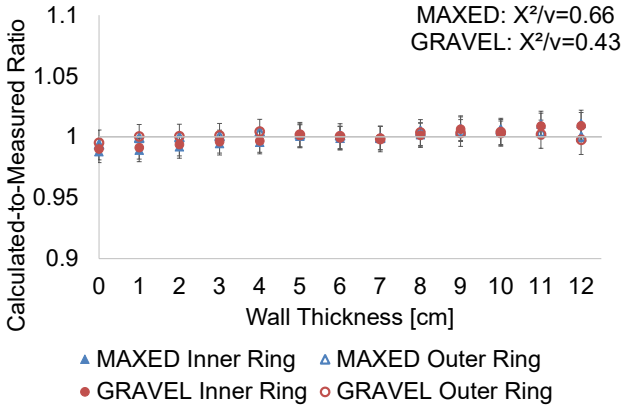

(b) AmBe

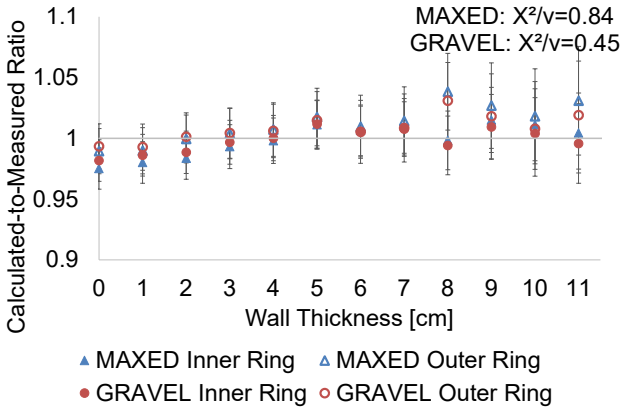

(c) AmLi

Figure 5.9: Calculated-to-measured ratios for ^{252}Cf, AmBe, and AmLi using the expected solution as the input guess spectrum for MAXED and GRAVEL

5.3.3 Sensitivity to Response Functions

A number of studies have shown that good knowledge of the response functions for the standard BSS are central to unfolding accurate neutron energy spectra [40, 41, 44, 48, 49], and the iBSS is expected to have a similar dependence on the response functions. The standard BSS is dependent on a single set of response functions for all moderators, because the counter's response is considered to be independent of the source or neutron field geometry. However, the iBSS could require a different set of response functions for each source, because the moderators, and thus geometry of the iBSS, changes with each neutron source. The extent to which the iBSS is affected by this was explored by unfolding the AmBe and AmLi neutron energy spectra using the ^{252}Cf response functions. In international safeguards, ^{252}Cf calibration sources are most often used as a surrogate for other neutron emitters in the fuel cycle. Californium-252 sources can be approximated as point sources and are assumed to have negligible self-moderation. However, most neutron sources in international safeguards cannot be approximated as a point, and using a ^{252}Cf calibration source as a surrogate to create the iBSS response functions has the potential to introduce significant errors into unfolding process.

Although the AmBe source was not approximated as a point source, it was physically similar in size to the ^{252}Cf source and expected to undergo limited self-moderation. The unfolded spectra from MAXED and GRAVEL, shown in Fig. 5.10a, had good relative agreement, suggesting that the source self-moderation was negligible. The relative error, shown in Fig. 5.10b, at the soft end of the spectrum was larger and above the 0.05 threshold for unfolded spectra from the ^{252}Cf response functions than the AmBe response functions in Fig. 5.7b. Due to the size of the AmBe source, self-moderation was likely highest at the soft end of the spectrum and thus aligns

with this result. There was also relatively good agreement between the calculated and measured count rates as indicated by the χ^2/ν and calculated-to-measured ratios. The χ^2/ν were within the desired critical value range for both MAXED and GRAVEL. The calculated-to-measured ratios were not within 1-σ for all of the wall thicknesses, as shown in Fig. 5.10c; the ratio at 12 cm was greater than 1-σ for both MAXED and GRAVEL, indicating that the fit to the data might not be accurate despite the acceptable solution spectrum. The response functions for ^{252}Cf can likely be substituted for sources similar in size to a ^{252}Cf source, but caution should be exercised as the data might not align as well. The similar results between the ideal scenario and this result suggest that the self-moderation by the AmBe source was limited and likely negligible for this measurement. The ^{252}Cf response functions can thus be used as a surrogate source for the iBSS if the source is physically similar in size and geometry to the ^{252}Cf source.

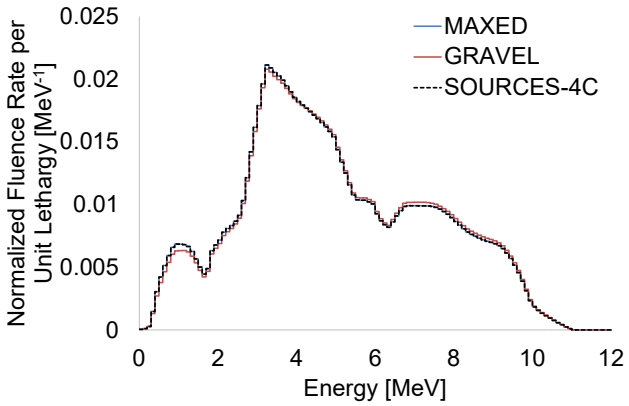

(a) Solution spectrum

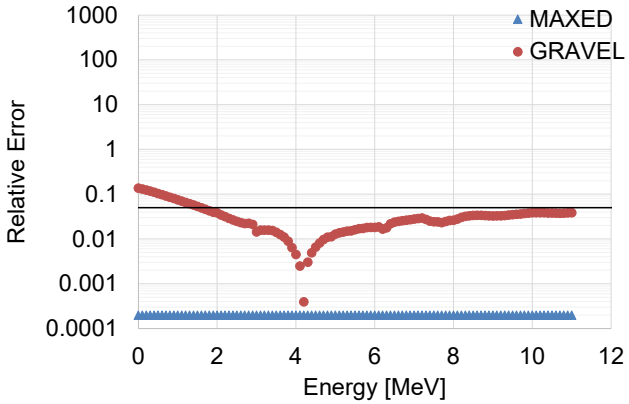

(b) Relative error

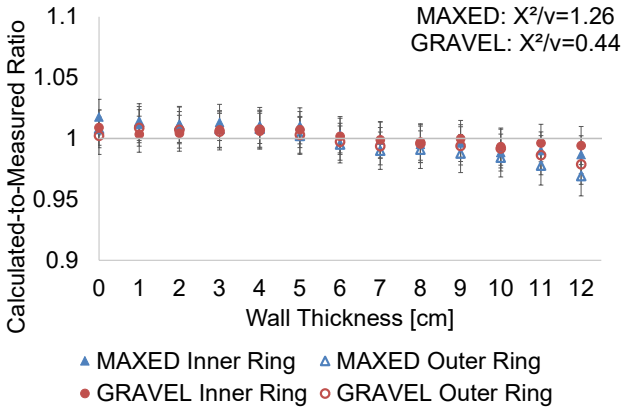

(c) Calculated-to-measured ratios

Figure 5.10: AmBe solution spectra, relative error plots, and calculated-to-measured ratios using the ^{252}Cf response functions with MAXED and GRAVEL

AmLi, on the other hand, was a physically larger neutron source than ^{252}Cf, so the neutrons emitted from the AmLi source were expected to undergo significant self-moderation that needed to be accounted for in the response functions. The effects of not accounting for this additional moderation were demonstrated by the stark disagreement between the solution spectra and expected spectrum shown in Fig. 5.11a and the large relative error above the 0.05 threshold shown in Fig. 5.11b. The χ^2/ν also were not within the desired critical value range nor were the calculated-to-measured ratios in Fig. 5.11c within 1-σ of unity for more than half of the wall thicknesses for MAXED and GRAVEL. All of the data thus point to the AmLi source undergoing significant self-moderation that needed to be accounted for in the response functions.

In international safeguards, items containing fissile material can rarely be approximated as a point source. Unlike the standard BSS, which requires a single response function for the set of moderators, the iBSS need to mirror the source, moderator, and counter geometry as closely as possible for the unfolding algorithms to produce the most accurate results. The iBSS thus requires a different set of response functions for each source and moderator geometry. This is not always realistic, however, and the user will likely have to make substitutions or approximations to the best of their knowledge when generating the response functions.

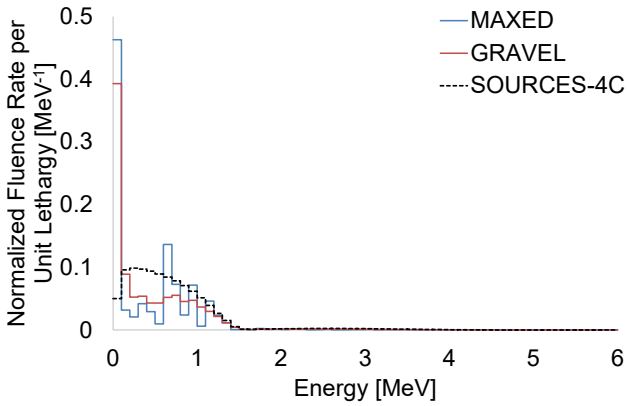

(a) Solution spectrum

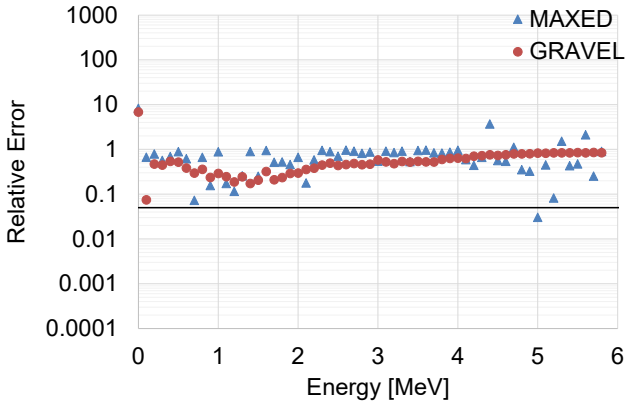

(b) Relative error

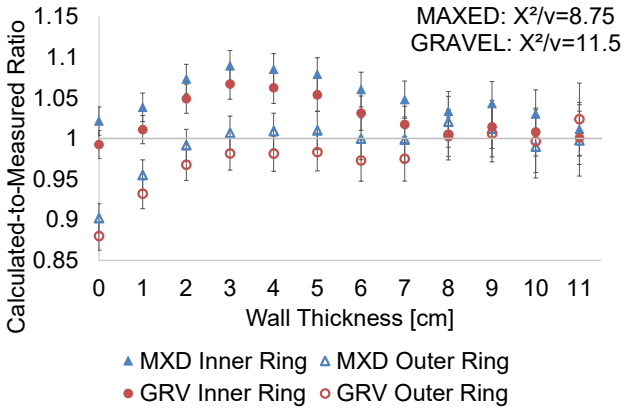

(c) Calculated-to-measured ratios

Figure 5.11: AmLi solution spectra, relative error plots, and calculated-to-measured ratios using the ^{252}Cf response functions with MAXED and GRAVEL

5.3.4 Sensitivity to the Quantity of *a priori* Information in the Input Guess Spectrum

The quality of the solution spectrum from the standard BSS is dependent on the quality and quantity of *a priori* information provided in the input guess spectrum for MAXED and GRAVEL [40]. The algorithms were tested to understand how they respond to varying amounts of *a priori* information in the input guess spectrum for the iBSS. The response functions that correspond to the proper source geometry were used for each spectral unfolding. A uniform spectrum was used as the input guess spectrum for unfolding the ^{252}Cf spontaneous fission spectrum, AmBe (α,n) spectrum, and AmLi (α,n) spectrum. The uniform spectrum represents the worst case scenario with regards to *a priori* information. Only information about the energy range of the spectrum was provided; no information about the shape of the solution spectrum was provided.

MAXED and GRAVEL both produced a solution spectrum that resembled a fission spectrum, but neither algorithm reproduced the ^{252}Cf Watt spectrum, as shown in Fig. 5.12a. The relative error, plotted in Fig. 5.12b, was greater than the 0.05 threshold for most data points and more than 5 times greater on a bin-by-bin basis than the relative error shown in Fig. 5.8a for the ideal scenario. The GRAVEL χ^2/ν was within the desired critical value range and all but one of the calculated-to-measured values were within 1-σ of unity. MAXED, on the other hand, did not have a χ^2/ν within the desired critical value range, and 1/3 of the calculated-to-measured ratios were not within 1-σ of unity. The MAXED unfolding results ultimately suggest that the correct solution spectrum is a fission spectrum, but the current solution spectrum does not match the data well. The MAXED results do, however, provide additional *a priori* information for a better constructed input guess spectrum.

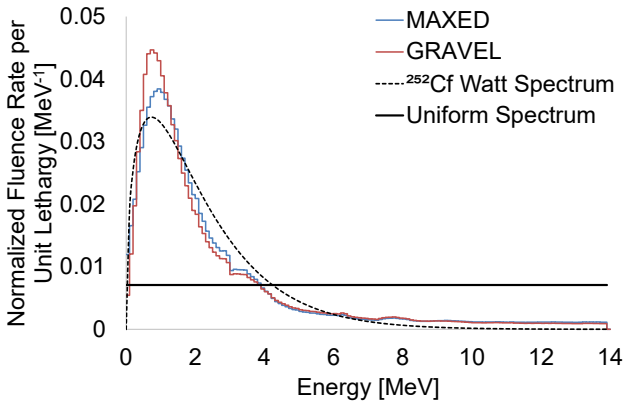

(a) Solution Spectrum

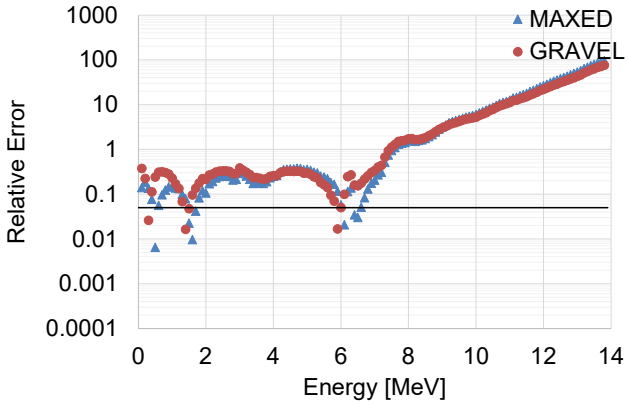

(b) Relative error

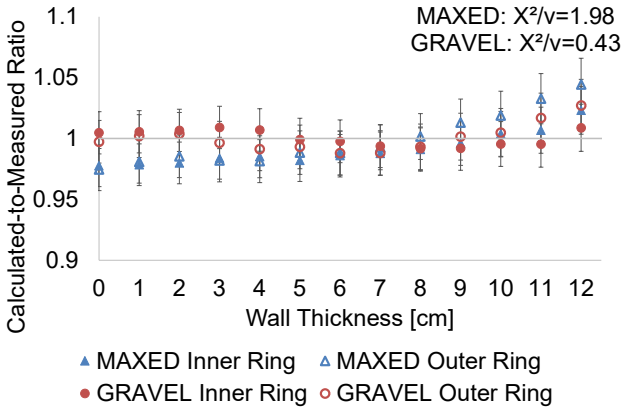

(c) Calculated-to-measured ratios

Figure 5.12: Solution spectrum, relative error, and calculated-to-measured ratios for ^{252}Cf unfolded using a uniform spectrum in MAXED and GRAVEL

A ^{240}Pu Watt spontaneous fission spectrum replaced the uniform spectrum as the input guess spectrum for the second round of unfolding. The MAXED and GRAVEL solution spectra are shown in Fig. 5.13a and the relative error in Fig. 5.13b. Although neither MAXED nor GRAVEL generated solution spectra that matched the ^{252}Cf Watt spectrum exactly, the relative error decreased by an order of magnitude across the entire energy range relative to the solution spectrum for the uniform input guess spectrum. Additionally, the solution spectra for MAXED and GRAVEL shifted from the input guess spectrum towards the ^{252}Cf Watt spectrum, which was the correct solution. The χ^2/ν values were both within the desired critical value range and the calculated-to-measured ratios were within 1-σ of unity. The updated input guess spectrum thus improved upon the solution spectrum for the uniform input guess spectrum to produce a better solution spectrum and match the measured count rate data better. This process of unfolding the neutron energy spectra several times while updating the input guess spectra with newly-learned *a priori* information is commonly implemented when using the standard BSS with limited or no *a priori* and can be used for the iBSS as well [40].

The AmBe (α,n) spectrum was a challenge for MAXED and GRAVEL to unfold without *a priori* information about the correct solution spectrum. The algorithms operate under the assumption that the solution spectrum will be smooth unless the user advises otherwise in the input guess spectrum [41]. However, the AmBe spectrum has three relative maximum points between 0–11 MeV that were difficult for MAXED and GRAVEL to unfold from the uniform spectrum as the input guess spectrum, as shown in Fig. 5.14a. Instead, both MAXED and GRAVEL produced a solution spectrum that resembled a smooth fission spectrum for both algorithms. The reduced chi-squared values, all within the desired critical value range, provided no indication in this example that the solution might be incorrect. Only

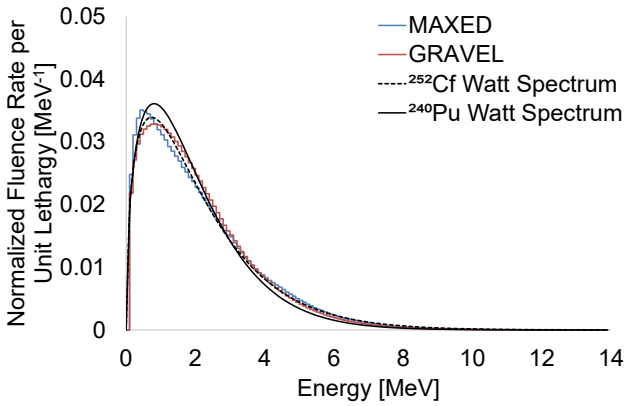

(a) Solution Spectrum

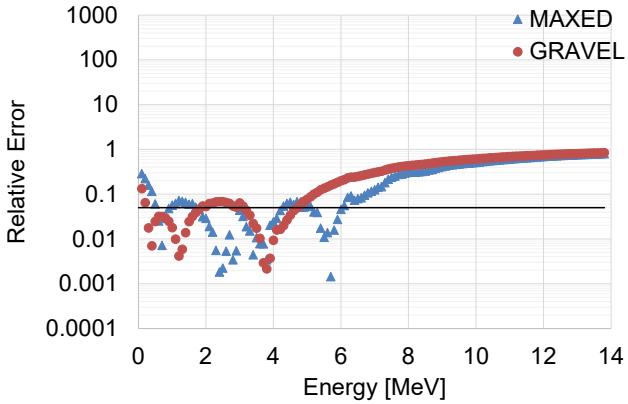

(b) Relative error

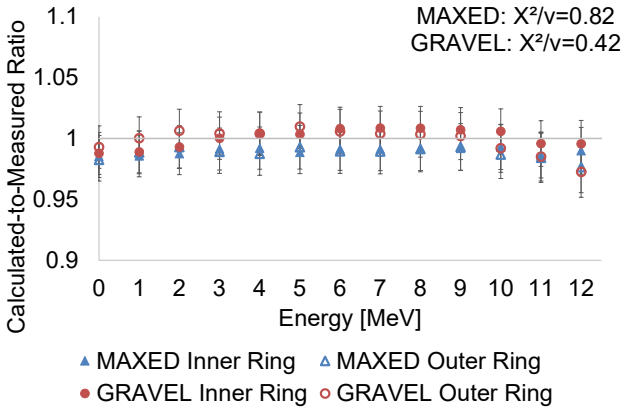

(c) Calculated-to-measured ratios

Figure 5.13: Solution spectrum, relative error, and calculated-to-measured ratios for ^{252}Cf unfolded using the^{240}Pu Watt spectrum in MAXED and GRAVEL

the 12 cm wall thickness calculated-to-measured ratios for the inner and outer ring for the MAXED unfolding with a uniform distribution provided any indication that the solution spectrum, without knowledge of the correct solution, might not be correct. The AmBe (α,n) spectrum was thus a good example to demonstrate that the quality of the *a priori* information is a crucial element for the unfolding algorithms to produce the correct solution spectrum.

Unfolding the AmLi (α,n) spectrum using the uniform input spectra produced solution spectra that resembled the correct solution at the soft end of the spectrum where the ^{7}Li(α,n) component is, as shown in Fig. 5.15a. The relative error was greater than 1 for most of the energy range and was highest towards the harder end of the spectrum where the ^{17,18}O(α,n) component would be. The reduced chi-square values were within the desired critical value range, but the calculated-to-measured ratios for the were not all within 1-σ of unity. The AmLi solution spectra, similar to the AmBe solution spectra, resembled a fission spectrum with a single peak in the spectrum. However, the ^{17,18}O(α,n) component was not properly unfolded, likely because the feature is small compared to the strong ^{7}Li(α,n) component. Much like the standard BSS, the MAXED and GRAVEL algorithms were not sensitive enough to detect that feature without *a priori* information due to the poor energy resolution of the iBSS [40, 41]. Small features, such as the ^{17,18}O(α,n) component, thus need to be included in the input guess spectrum if MAXED and GRAVEL are to include it in the unfolded spectrum.

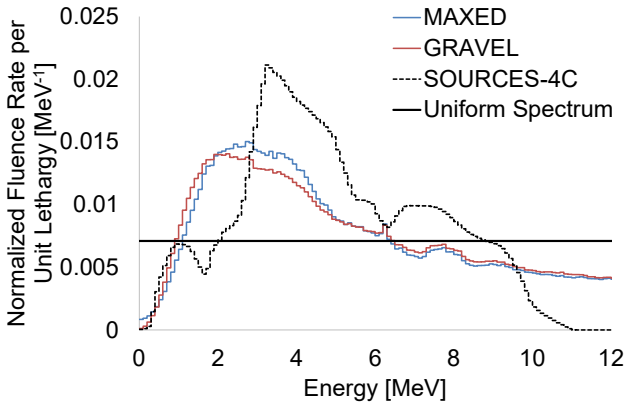

(a) Solution Spectrum

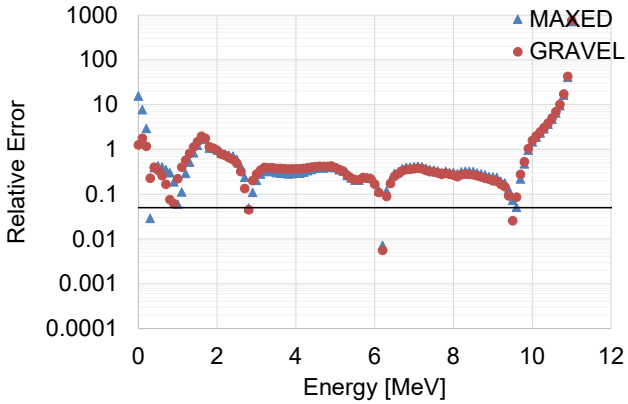

(b) Relative error plot

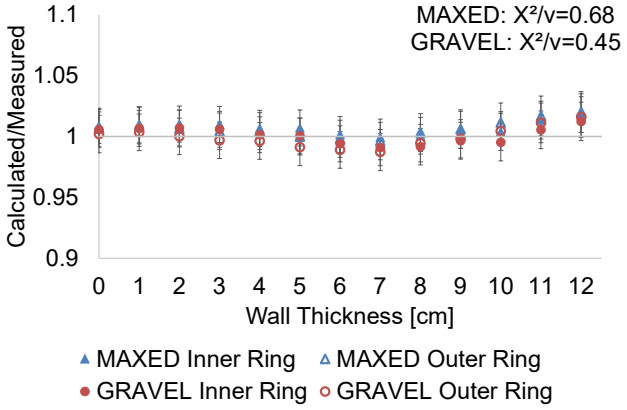

(c) Calculated-to-measured ratios

Figure 5.14: Solution spectrum, relative error, and calculated-to-measured ratios for AmBe unfolded using a uniform spectrum in MAXED and GRAVEL

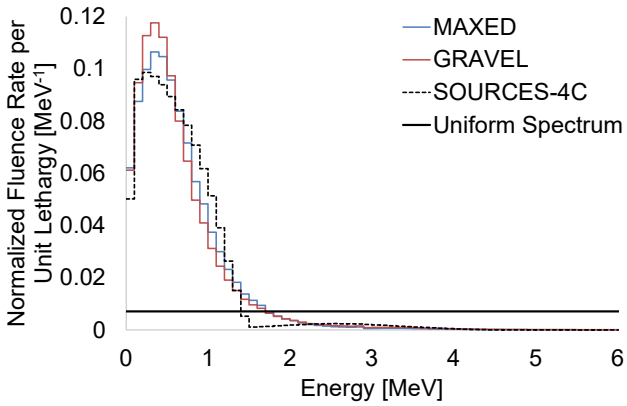

(a) Solution Spectrum

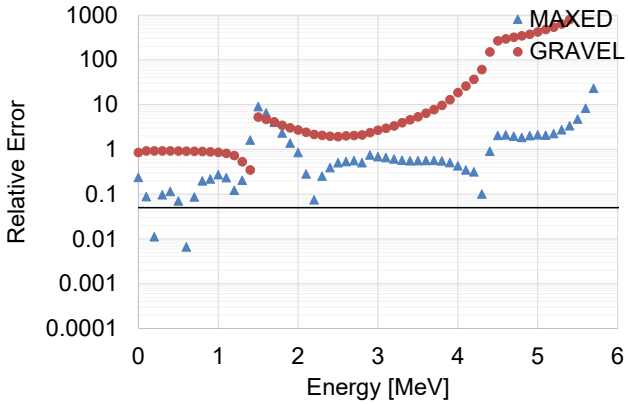

(b) Relative error

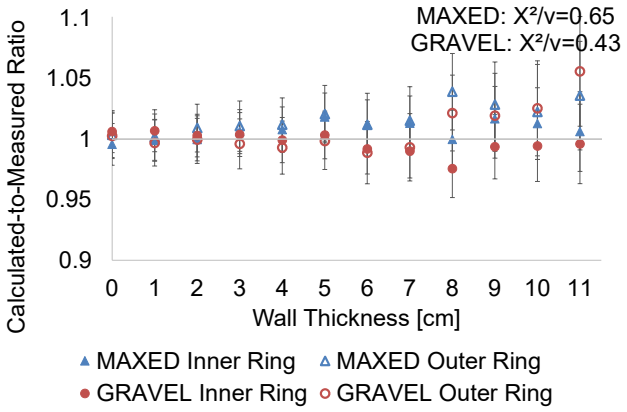

(c) Calculated-to-measured ratios

Figure 5.15: Solution spectrum, relative error, and calculated-to-measured ratios for AmLi unfolded using a uniform spectrum in MAXED and GRAVEL

5.4 Sensitivity to Impurities in AmLi Sources

The unknown oxygen content in an AmLi source translates to an additional ^{17,18}O(α, n) component to the neutron energy spectrum. Additionally, reports of a Be impurity could affect the neutron energy spectrum for individual AmLi sources. Quantifying the ^{17,18}O(α, n) and potential Be contributions to the neutron emission rate for individual AmLi sources is a desirable feature for the iBSS [13]. This section explores the ability of the iBSS to quantify the ^{17,18}O(α, n) and Be impurity content from a general AmLi spectrum.

Neutron energy spectra were derived by scaling the individual (α, n) neutron energy spectra for ^{7}Li, ^{17,18}O, and ^{9}Be to the desired fraction and adding the spectra together on a bin-by-bin basis. Each of these spectra are pictured individually in Fig. 5.16. Neutron energy spectra were created for 3%, 5%, and 10% of the total neutron emissions from ^{17,18}O(α, n) and 97%, 95%, and 90% of the total neutron emissions from ^{7}Li(α, n), respectively. For the Be impurity, neutron energy spectra were created for 0.3, 1, and 3% neutron emissions from the ^{9}Be (α, n) reaction, 5% neutron emissions from the ^{17,18}O (α, n) reaction and 94.7, 94, and 92% neutron emissions from the ^{7}Li (α, n) reaction, respectively. A previous study suggested that the Be impurity, if it were present in the source, accounted for 0.3–3% of the neutron emission rate [99]. Each spectra was input into MCNP to generate simulated count rate data to be input into the MAXED and GRAVEL unfolding algorithms. The AmLi response functions and input guess spectrum used in previous sections were used here.

The MAXED and GRAVEL solution spectra for the varying ^{17,18}O(α, n) content are plotted in Fig. 5.17 on a semi-logarithmic scale the input guess spectrum generated in SOURCES-4C for reference. The MAXED and GRAVEL solution spec-

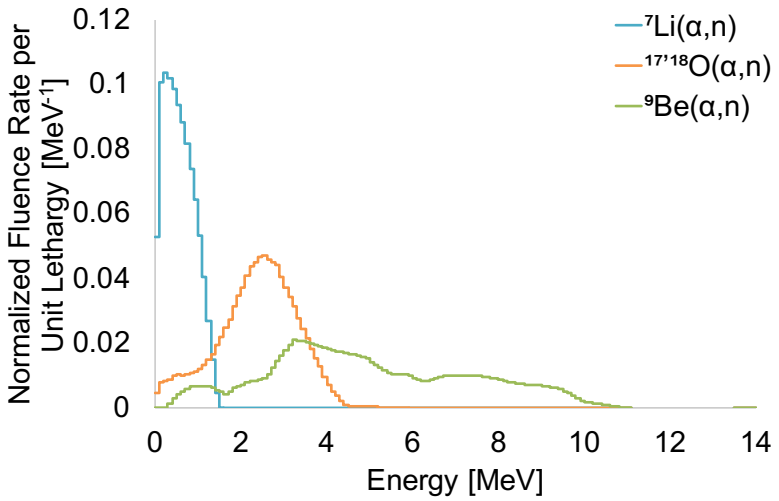

Figure 5.16: (α, n) spectra from alpha particles emitted from ^{241}Am

tra for a given ^{17,18}O(α, n) were indistinguishable from each other and indicate that both solutions agreed. The calculated and measured count rate had good agreement as evidenced by χ^2/ν being within the desired critical range and the calculated-to-measured ratios being within 1-σ of unity for all data, as shown in Fig. 5.18. The spectra were distinguishable based on ^{17,18}O(α, n) neutron emissions. The spectra displayed on a logarithmic scale in Fig. 5.17b show the fluence rate per unit lethargy increase with respect to percent ^{17,18}O(α, n) where the ^{17,18}O(α, n) spectrum was most prominent (i.e. 2–4 MeV). However, the spectra displayed on a linear scale in Fig. 5.17a show that the ^{7}Li(α, n) portion of the neutron energy spectrum was distorted for changing ^{17,18}O(α, n) content. The neutron energy spectrum is essentially a probability density function, so the integral value of the curve must be equal to one. The algorithms likely distorted the spectrum to account for the lesser probability of the ^{17,18}O(α, n) content with respect to the input guess spectrum by adjusting the portions with higher probability (i.e. the ^{7}Li(α, n) content). Although the iBSS was able to scale the spectrum based on the ^{17,18}O(α, n) contribution to the neutron

emission rate, the more prominent ^{7}Li(α, n) portion of the neutron energy spectrum was distorted. Additional experimental studies will need to be conducted to confirm whether or not the distorted ^{7}Li(α, n) agrees with neutron energy spectra for individual AmLi sources.

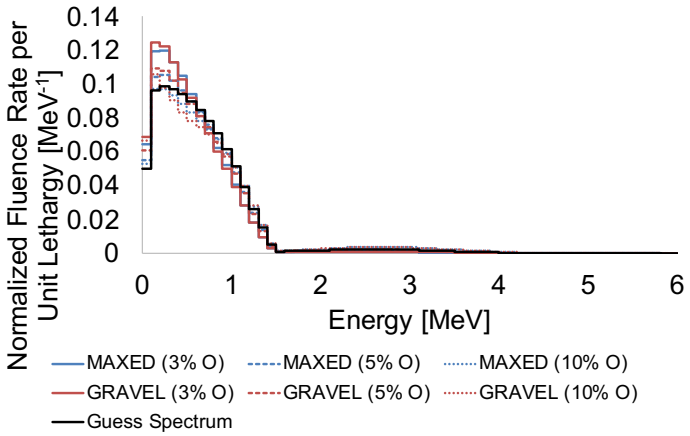

(a) Linear Scale

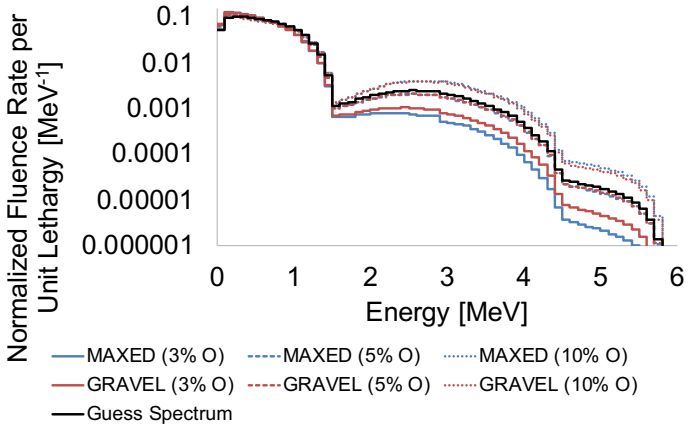

(b) Semi-logarithmic Scale

Figure 5.17: MAXED and GRAVEL solution spectra for AmLi sources with total neutron emissions of 3, 5, and 10% from the ^{17,18}O(α, n) reaction and 97, 95, 90% from the ^{7}Li(α, n) reaction, respectively. The input guess spectrum was generated from a general AmLi source material composition.

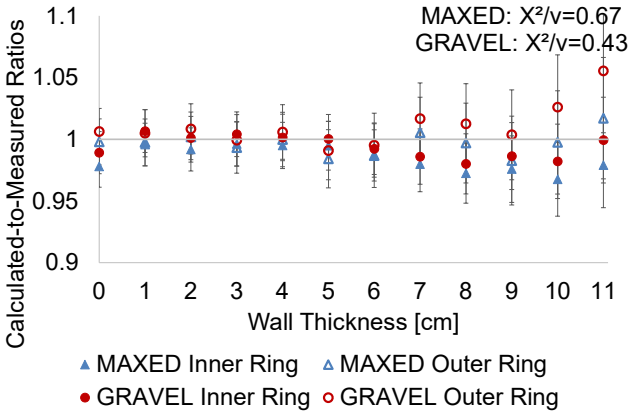

(a) 3% O and 97% Li

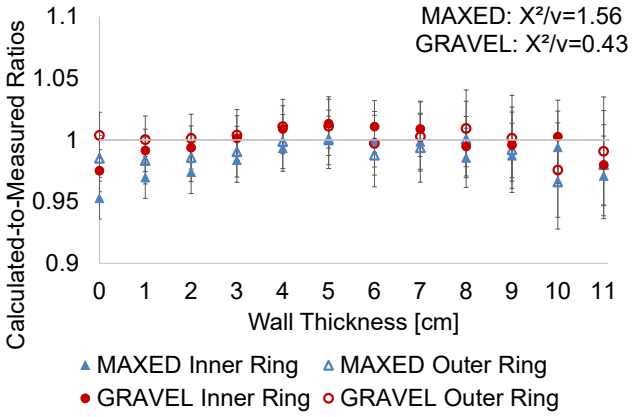

(b) 5% O and 95% Li

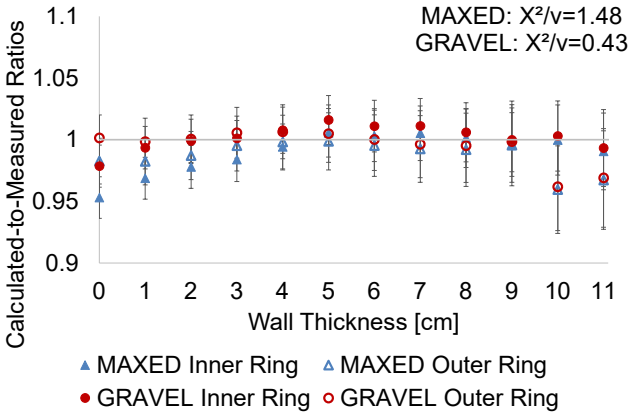

(c) 10% O and 90% Li

Figure 5.18: Calculated-to-measured ratios for unfolded AmLi spectra with 3–10% of the neutron emissions from ^{17,18}O (α, n)

The MAXED and GRAVEL solution spectra for the varying ^{9}Be(α, n) content are shown in Fig. 5.19 on a linear and semi-logarithmic scale alongside the input guess spectrum. The input guess spectrum contained neutron emissions only from ^{7}Li and ^{17,18}O and not ^{9}Be, because it would be assumed that there was no ^{9}Be content in an AmLi source with unknown source composition. The purpose of this section was to determine how the general AmLi spectrum with ^{17,18}O content would be affected with a Be impurity and if it could be identified using the general input guess spectrum. Good agreement was achieved between the simulated count rate data and the solution spectra as evidenced by χ^2/ν being within the desired critical range and the calculated-to-measured ratios being within 1-σ of unity for all data, as shown in Fig. 5.20. None of the solution spectra exactly reproduced the input guess spectra, but were almost indistinguishable between each other, indicating that the Be content cannot be easily identified or quantified using the iBSS methodology using a general AmLi spectrum with contributions only from ^{7}Li and ^{17,18}O. Additionally, the changes in the solution spectra from the input guess spectrum resemble similar changes in the solution spectra in Fig. 5.17 for different neutron emission percentages from the ^{17,18}O (α, n) reaction, opening up the possibility for a Be contaminant to be mistaken for excess ^{17,18}O in the item. The Be content could be better identified if the ^{9}Be(α, n) spectrum was included in the input guess spectrum. However, this will disrupt the solution spectra and possibly cause inaccuracies, because the algorithm would assume Be was present even though it was not confirmed to be present. It is recommended to identify the presence of Be contamination via gamma-ray spectroscopy.

The iBSS demonstrated promise for characterizing the neutron energy spectra for individual AmLi sources. However, impurities in the sources must be present in the input guess spectrum so that the unfolding algorithms can scale the quantity of the contribution. Without knowledge of the impurity, the unfolding algorithm

does not appear to be able to identify and quantify the contribution to the neutron emission rate from that impurity.

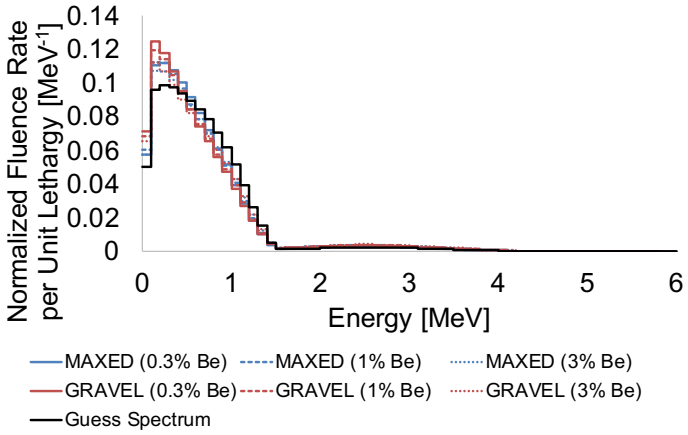

(a) Linear Scale

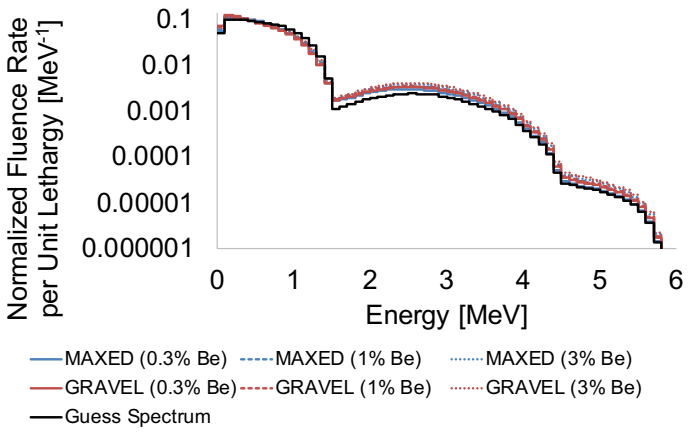

(b) Semi-logarithmic Scale

Figure 5.19: MAXED and GRAVEL solution spectra for AmLi sources with total neutron emissions of 0.3, 1, and 3% from the ^{9}Be (α, n) reaction, 5% from the ^{17,18}O (α, n) reaction and 94.7, 94, and 92% from the ^{7}Li (α, n) reaction, respectively. The input guess spectrum was generated from a general AmLi source material composition with oxygen.

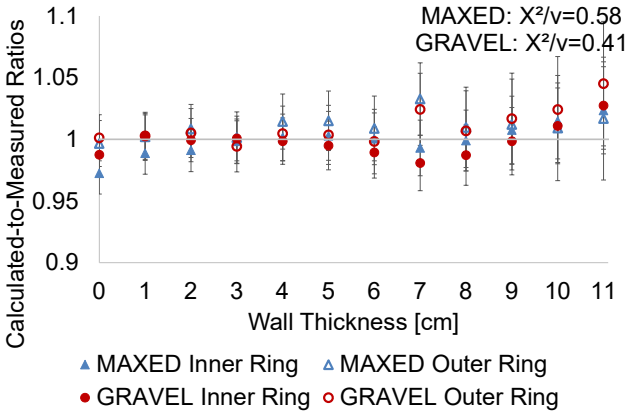

(a) 0.3% Be and 99.7% Li

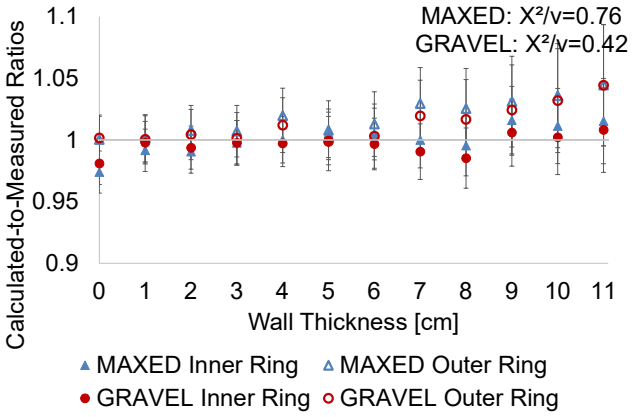

(b) 1% Be and 99% Li

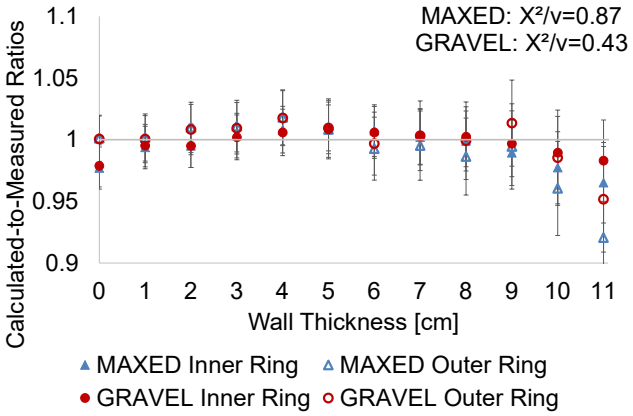

(c) 3% Be and 97% Li

Figure 5.20: Calculated-to-measured ratios for unfolded AmLi spectra with 0.3–3% of the neutron emissions from ^{9}Be (α, n)

5.5 Conclusions

The iBSS successfully unfolded the the ^{252}Cf spontaneous fission spectrum, AmBe (α, n) spectrum, and AmLi (α, n) spectrum in the ideal scenario where the response functions matched the geometry exactly and the input guess spectrum was the correct solution. Unfolding the AmBe neutron energy spectrum yielded acceptable results when the ^{252}Cf response functions were used, because the two sources had similar geometry and thus similar response functions. The method did not, however, fair as well when the ^{252}Cf response functions replaced the AmLi response functions or when the input guess spectrum incorporated little *a priori* information about the content of the source. The neutron spectrum unfolded using the iBSS scaled with oxygen content in the AmLi source. Therefore, a potential use for iBSS could be to verify oxygen content in AmLi sources. The capability of iBSS to flag the presence of Be impurities was fairly limited. The observed perturbation on the neutron spectrum was not as significant as oxygen. Furthermore, when investigating an AmLi source of unknown composition, it may not be possible to determine whether Be or O content perturbed the neutron energy spectrum. The presence or absence of Be must first be verified using high-resolution gamma-ray spectrometry. The dependence of the iBSS on well-characterized response functions and quality *a priori* information makes the iBSS well-suited to scenarios where measurements are to be verified. International safeguards is a technical discipline built upon verifying state declarations to ensure the peaceful use of nuclear science and technology. Although the inverse Bonner sphere concept was originally proposed as a method to establish the AmLi neutron energy spectrum, it could have a broader impact on international safeguards for verification measurements.

Chapter 6

The Inverse Bonner Sphere Spectrometer as a Verification Method for SOURCES-4C

Abstract

The inverse Bonner sphere spectrometer (iBSS) was used as a tool to experimentally verify neutron energy spectra in SOURCES-4C. SOURCES-4C is a computer code that produces neutron energy spectra for spontaneous fission neutrons, delayed neutrons, and (α,n) neutrons that can be used for MCNP simulations of neutron measurements in international safeguards. Although the code continues to be updated, discrepancies exist between experimentally determined neutron energy spectra and SOURCES-4C, particularly for (α, n) reactions. Three ^{252}Cf sources, a high-purity $^{240}PuO_2$ source, four AmLi sources, and one AmBe source were each measured in triplicate using the large volume active well coincidence counter in passive mode. Sources were centrally placed in a different cylinder made from high density polyethylene for

each measurement with wall thicknesses of 0.64–6.99 cm for ^{252}Cf and AmBe and 0.64–5.72 cm for $^{240}PuO_2$ and AmLi. Neutron energy spectra for each source were unfolded using the MAXED and GRAVEL algorithms. The solution spectra for ^{252}Cf and $^{240}PuO_2$ agreed to within 1-σ of the expected spectrum, indicating that the iBSS can accurately unfold neutron energy spectra and can thus be used as a verification tool. AmLi and AmBe did not, however, agree with the SOURCES-4C neutron energy spectra, indicating that the SOURCES-4C spectra may need to be updated using experimentally measured spectra.

6.1 Introduction

International safeguards are technical measures implemented to ensure the peaceful use of nuclear science and technology. Neutron counting is an established non-destructive assay method used in international safeguards to measure the fissile mass of an item [20]. For accurate neutron measurements, it is important to have knowledge of the significant sources of neutrons emitted from an item, which can include neutrons from induced fission, spontaneous fission, and (α, n) reactions. SOURCES-4C is a computer code that produces neutron energy spectra for spontaneous fission neutrons, delayed neutrons, and (α,n) neutrons for complex source material compositions [8, 9]. In international safeguards, SOURCES-4C is most commonly used to generate energy spectra for MCNP simulations of neutron measurements for verifying declared content in enriched U storage cylinders or spent nuclear fuel. The code has been benchmarked using experimental results and continues to be updated as more information becomes available. The most extensive benchmarking study was performed using well-characterized PuO_2 items with varying burn-up content [39]. All PuO_2 spectra in SOURCES-4C had excellent relative agreement with experimen-

tally measured spectra. Other experimental benchmark studies for neutron energy spectra, such as those for PoBe and PuBe, did not have as good of relative agreement as the PuO_2 study, differing by as much as 18%. Additionally, other computationally-determined spectra for (α, n) reactions, such as the AmLi (α, n) reaction, do not agree with the spectrum produced by SOURCES-4C [11]. A tool, such as the inverse Bonner sphere spectrometer (iBSS), could be useful for experimentally verifying neutron energy spectra in SOURCES-4C and updating those that cannot be verified.

The inverse Bonner sphere concept was initially proposed as a methodology to determine the neutron energy spectrum of individual AmLi sources for improved detector performance characterization [13]. The concept was then expanded and the proof-of-concept was demonstrated for a novel neutron spectrometer using MCNP computer simulations [100]. In the iBSS, a neutron source was placed in the center of a cylindrical moderator and surrounded by multiple concentric rings of moderated ^{3}He proportional counters. The moderator diameter was incrementally increased to illicit a change in the detector response due to increased neutron moderator with respect to neutron energy so that the neutron energy spectrum could be unfolded. Based on preliminary results using simulated data, the iBSS successfully unfolded the ^{252}Cf spontaneous fission spectrum, AmLi (α, n) spectrum, and the AmBe (α, n) spectrum under ideal conditions [100]. The ideal scenario for the iBSS included detector response functions that matched the physical geometry of the measurement and an input guess spectrum that was similar to the true spectrum.

This work demonstrates the application of the iBSS for providing experimental data to verify neutron energy spectra in SOURCES-4C using the large volume active well coincidence counter (LVAWCC) in passive mode. Proof-of-concept for the methodology using experimental measurements was demonstrated using ^{252}Cf. Experimentally unfolded neutron energy spectra of $^{240}PuO_2$, AmLi, and AmBe were

then compared to SOURCES-4C and other experimentally measured spectra to verify or contest the spectra.

6.2 Materials and Methods

6.2.1 Experimental Setup

The Oak Ridge National Laboratory (ORNL) Large-Volume Active Well Coincidence Counter (LVAWCC), pictured in Fig. 6.1 was used for this work. The LVAWCC operates in the same manner as the AWCC (Canberra Industries Inc., Model JCC-51), but has a larger cavity and more ^{3}He proportional counters [79]. The LVAWCC detector cavity had a diameter of 27.9 cm and a depth of 38.1 cm. The counter had 48 ^{3}He proportional counters (GE RS-P4-08P4-202) spaced equally around the detector cavity in two concentric rings of 24 counters each. The proportional counters had an outer diameter of 2.54 cm, a steel wall thickness of 0.508 mm steel wall thickness, and an active length of 63.5 cm. Each ^{3}He proportional counter was filled to a pressure of 4.5 atm with ^{3}He gas and Ar as a quench gas. The counters were embedded in high density polyethylene (HDPE) ($\rho = 0.95$ g/cm^{3}) to moderate neutrons to thermal energies for optimal detection by the ^{3}He(n,p) reaction. Graphite end plugs with an internal 0.5 mm Cd layer were used for this work.

(a) Exterior

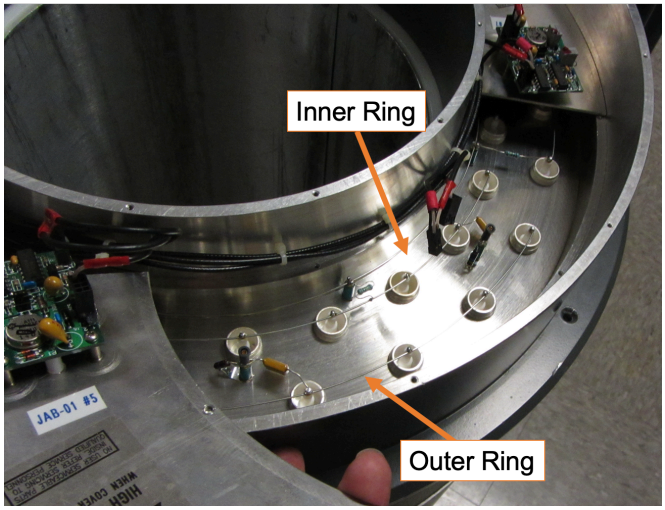

(b) Top of rings of ^{3}He proportional counters and associated electronics in junction box

Figure 6.1: Large volume active well coincidence counter

Three ^{252}Cf sources, a high-purity $^{240}PuO_2$ source, four ^{241}AmLi sources, and one ^{241}AmBe source were measured in this work. Pertinent technical data for each source was provided in Table 6.1. Technical data sheets are available in Appendix D. A neutron emission rate was not provided for AmBe on the technical data sheet, and the $^{240}PuO_2$ source encapsulation was designed for this source specifically and did not have an associated model number. In addition to the stainless steel encapsulation, the ^{241}AmLi sources were placed in a tungsten pot to shield the 59.5 keV gamma ray to reduce the dose rate. The tungsten pot had outer dimensions of 5.73 cm in diameter and 4.31 cm in height and inner dimensions of 2.68 cm in diameter and 3.17 cm in height.

Table 6.1: Neutron source information.

Neutron Emitter	Serial No.	Neutron Emission Rate [n/s]	Encapsulation
^{252}Cf	FTC-Cf-1830[1]	$1.33{\cdot}10^5 \pm 1.06\%$	Model 10S
^{252}Cf	FTC-Cf-3010[1]	$5.64{\cdot}10^4 \pm 1.07\%$	Model 10S
^{252}Cf	EZ Q9-304[2]	$1.53{\cdot}10^5 \pm 1.07\%$	3023 Capsule
^{240}Pu	C2-05N	$1.74{\cdot}10^4$	N/A[4]
^{241}AmLi	AN-HP-C268[3]	$5.5{\cdot}10^4 \pm 10\%$	C-series
^{241}AmLi	AN-HPC272[3]	$5.5{\cdot}10^4 \pm 10\%$	C-series
^{241}AmLi	AN-HP-N458[3]	$5.5{\cdot}10^4 \pm 10\%$	N-series
^{241}AmLi	AN-HP-N459[3]	$5.5{\cdot}10^4 \pm 10\%$	N-series
^{241}AmBe	K560/18[2]	N/A[4]	N02 Capsule

[1] Frontier Technology Corporation, 1641 Burnett Drive, P.O. Box 486, Xenia, OH 45385

[2] Eckert & Ziegler Isotope Products, 24937 Avenue Tibbitts, Valencia, CA 91355

[3] Gammatron, Inc., P.O. Box 34042, Houston, TX 77034

[4] Not available.

Cylindrical moderators were machined using HDPE to encase the neutron sources. A cavity was positioned such that the sources were in the center of the cylinder. A plug was then machined for each cylinder to sit on top of the source and fill the cavity. The HDPE cylinders, pictured in Fig. 6.2, were designed to fit each of the neutron sources using the same set of moderators. Because the AmLi sources were physically the largest, the cavity diameter was machined to fit these sources. The $^{240}PuO_2$ source was as tall as the AmLi sources but with a slightly smaller diameter and fit in the cylinder cavity without an insert. The ^{252}Cf and AmBe sources, however, were physically much smaller and required an insert made of HDPE to be machined that had the same dimensions as the AmLi sources. By doing this, the wall thickness of the insert cylinder and larger cylinder was additive. Two additional smaller cylinders with were machined so that neutron measurements could be collected with the thinner wall thicknesses. Physical dimensions for all cylinders and plugs are provided in Appendix C.

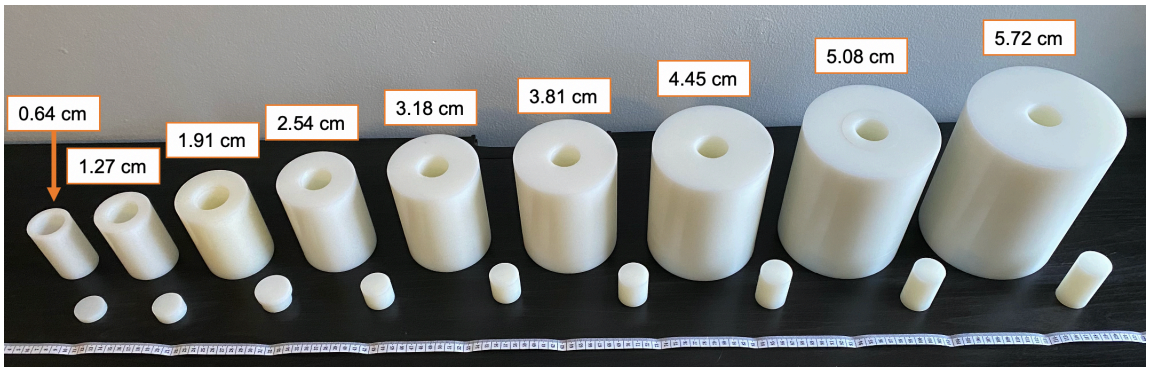

Figure 6.2: HDPE cylinders for $^{240}PuO_2$ and AmLi sources and ^{252}Cf and AmBe inserts. Dimensions represent wall thickness.

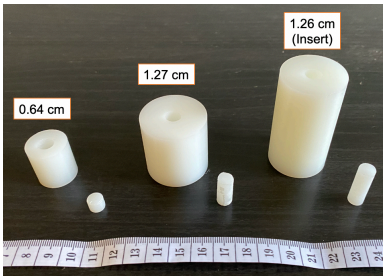

Figure 6.3: HDPE cylinders for ^{252}Cf sources. Dimensions represent wall thickness.

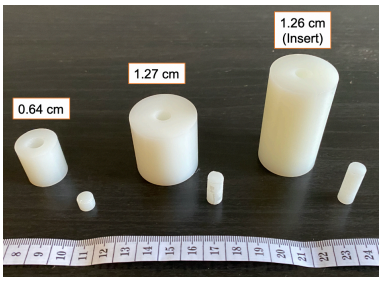

Figure 6.4: HDPE cylinders for the AmBe source. Dimensions represent wall thickness.

Neutron measurements were collected using the JSR-15 Handheld Multiplicity Register (Canberra Industries Inc., Meriden, CT) controlled by the IAEA Neutron Coincidence Counting (INCC) software [101]. Although typically used for neutron coincidence counting, only the singles count rate data from the inner ring and outer ring were considered. Sources and moderators were placed on a lab jack and centered in the detector both radially, as shown in Fig. 6.5, and longitudinally. Each configuration for each source was measured in triplicate to account for repositioning errors. Californium-252, AmLi, and AmBe sources were measured for 5 min in each configuration and ^{240}Pu was measured for 15 min in each configuration. Background measurements were collected for 5–15 min with only the lab jack in the LVAWCC cavity. Additional long background measurements were collected to characterize the background count rate.

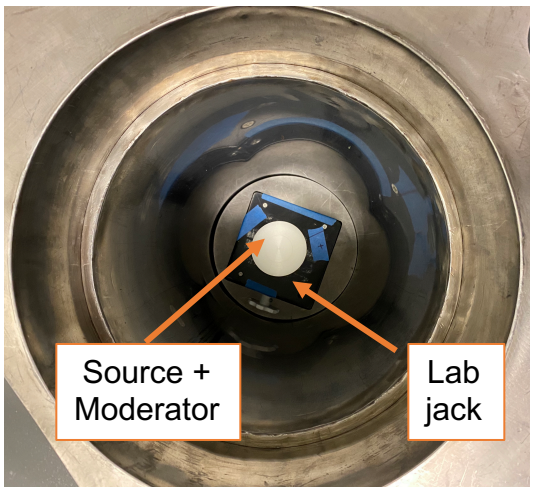

Figure 6.5: Source and moderator positioned centrally inside of the LVAWCC detector cavity on an aluminum lab jack

6.2.2 Unfolding Algorithms

Spectra were unfolded using the "few channel" versions of the MAXED and GRAVEL algorithms [60, 61]. Both codes were compiled using the suggested input parameters for a standard BSS system [61]. The algorithm inputs include count rate data and associated uncertainties, response functions, and input guess spectra. Count rate data was entered directly from the INCC software for each ring of the LVAWCC. Associated uncertainty was split into counting statistics and other sources of uncertainty. Other sources of uncertainty was set to the uncertainty in the source assay for this work, because it was the largest source of uncertainty outside of counting statistics. Source assay uncertainty was 1% for ^{252}Cf sources and the AmBe source. The source assay uncertainty was increased to 3% for AmLi because of the unknown composition of the source material. The ^{240}Pu source assay uncertainty was set to 0%, because the source composition was determined via mass spectrometry, which typically has an associated uncertainty much less than counting statistics. The algorithms added uncertainty due to counting statistics and other sources of uncertainty

in quadrature.

Response functions were generated in MCNP using a model of the LVAWCC. The neutron sources, HDPE cylinders, and aluminum lab jack were modeled in the detector cavity to match the experimental geometry. A depiction of the LVAWCC MCNP model with an AmLi source and HDPE cylinder with 4.45 cm wall thickness is in Fig. 6.6. Californium-252 sources were modeled as point sources from the center of the source. The high-purity $^{240}PuO_2$ source material was modeled using the exact source composition measured by mass spectrometry. Because the composition of AmLi source material is generally not well documented, a general source mixture (ρ=1.6 g/cm^3) was used of LiOH and AmO_2 with a ^{7}Li/^{241}Am atom ratio of 263 to 1 [11]. The AmBe source material (ρ=1.3 g/cm^3) was similarly unknown and assumed to be a mixture of AmO_2 and Be with a ^{9}Be/^{241}Am ratio of 9.8 [96, 97]. Neutrons were uniformly emitted from the source material volume for the AmBe, AmLi, and ^{240}Pu sources. Monoenergetic neutrons were emitted from each source in 0.1 MeV increments from 0.1–14 MeV. Additional data points were included for the AmLi response functions in 0.05 MeV increments between 0–2 MeV due to the soft nature of the AmLi spectrum. Separate response functions were created for each ring of ^{3}He proportional counters.

Input guess spectra were tailored to each neutron emitter. A Watt fission spectrum was used for all ^{252}Cf sources. SOURCES-4C was used to generate input guess spectra for the high-purity $^{240}PuO_2$ source, AmLi sources, and AmBe source. The homogeneous option in SOURCES-4C—which simulates the α-emitting isotopes as intimately mixed with the light target elements—was used to create the input guess spectra with the same source composition entered into the MCNP simulations for the response functions. The PuO_2 input guess spectrum included components from spontaneous fission and the ^{17,18}O(α,n) reaction component. The AmLi input

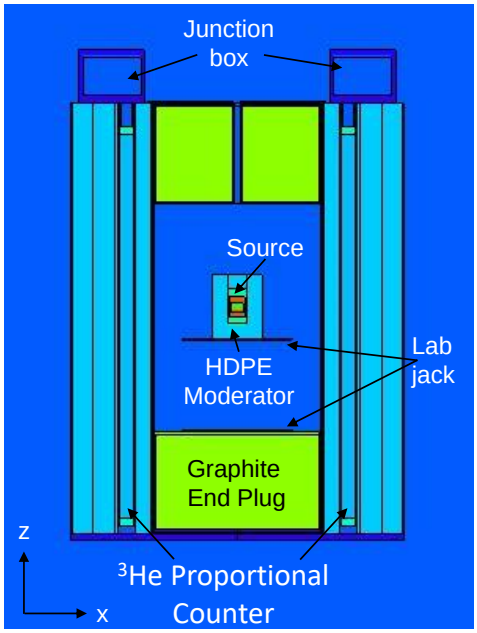

Figure 6.6: Depiction of the cross section of the LVAWCC in MCNP with an AmLi source and HDPE cylinder with 4.45 cm wall thickness

guess spectrum included the ^{7}Li(α,n) and ^{17,18}O(α,n) reactions. The AmBe input guess spectrum was composed of the ^{9}Be(α,n) and ^{17,18}O(α,n) reactions.

6.3 Results and Discussion

Neutron measurements were collected for ^{252}Cf, $^{240}PuO_2$, AmLi, and AmBe neutron sources. Net count rates are listed in Appendix C for each measurement. Measurements were collected in three different geographic locations and thus had different background count rates. Sources FTC-Cf-1830, EZ Q9-304, AN-HP-C268, and AN-HP-C272 were measured in the same location with an average total background count rate of 36.35±0.02 cpm, 10.06±0.01 cpm for the inner ring, and 26.29±0.02 cpm for the outer ring. Source C2-05N was measured in a location with an average total background count rate of 6.04±0.01 cpm, 2.40±0.01 cpm for the inner ring, and 3.64±0.01 cpm for the outer ring. Sources FTC-Cf-3010, AN-HP-N458, AN-HP-

N459, K560/18 were measured in a location with an average background count rate of 8.56±0.01 cpm for both rings, 3.17±0.01 cpm for the inner ring, and 4.94±0.01 cpm for the outer ring.

Detection efficiency was determined using the bare NIST-certified FTC-Cf-1830 ^{252}Cf source. The value was calculated by dividing the net singles count rate by the decay-corrected neutron emission rate. The total detection efficiency was 34.5±0.4%, 20.6±0.2% for the inner ring, and 13.9±0.1% for the outer ring. The LVAWCC and HDPE cylinder MCNP models were benchmarked to experimental measurements using the absolute detection efficiency for each ring and moderator combination. NIST-certified FTC-Cf-1830 and the high-purity $^{240}PuO_2$ source were used to benchmark the MCNP model to experimental results, because both of these sources are well-characterized and act as standard sources. The simulated and measured detection efficiencies for FTC-Cf-1830 and the $^{240}PuO_2$ source are shown in Fig. 6.7. The agreement between the simulated and measured indicated that the MCNP model can reliably predict experimental results and can thus be used to create the response functions.

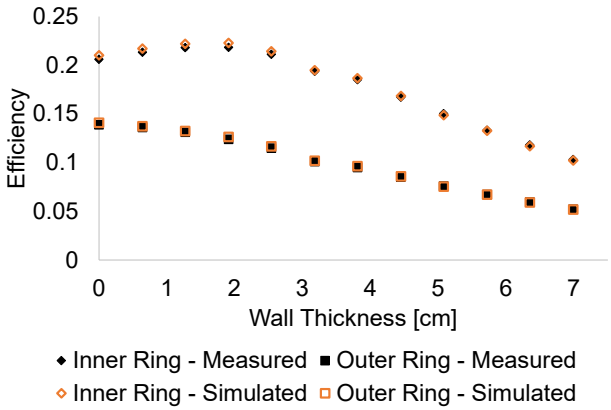

(a) FTC-Cf-1830

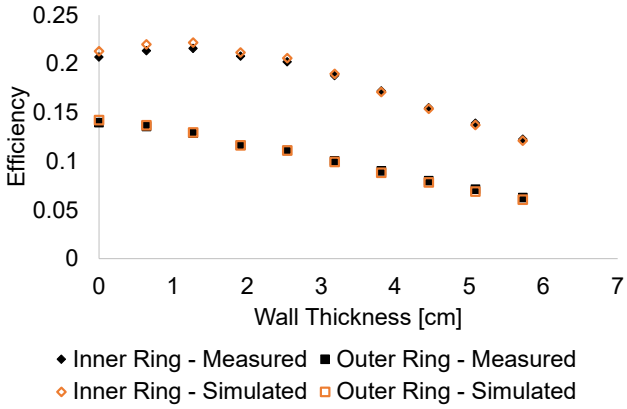

(b) $^{240}PuO_2$

Figure 6.7: Comparison of measured and simulated detection efficiency values for the LVAWCC. Error bars are too small to be visible.

6.3.1 Californium-252

Californium-252 is commonly used as a standard for establishing the performance of novel neutron counters and methodologies, because it has well-known fissioning characteristics, a well-defined neutron energy spectrum, and approximates to a point. The three ^{252}Cf sources measured here were used to demonstrate the iBSS proof-of-concept using experimental data, because previous work only demonstrated proof-of-concept using simulated data [100]. Each of the three ^{252}Cf sources measured

were previously characterized using high-resolution gamma-ray spectroscopy to confirm source age and isotopic ratios on the technical data sheet, but the technical data sheet could only be confirmed for NIST-certified FTC-Cf-1830 [71]. However, calculations using nuclear data determined that the fissioning characteristics of FTC-Cf-3010 and EZ Q9-304 would deviate less than 0.5% from the characteristics of a pure ^{252}Cf source. This means that both sources can be assumed to act as pure ^{252}Cf sources with negligible contributions from secondary neutron emitters ^{250}Cf and ^{248}Cm, because the changes in the fissioning characteristics are smaller than the measurement uncertainties. Even though the technical data sheets could not be confirmed for all three sources, it was hypothesized that all of the sources can be used to establish experimental proof-of-concept for the iBSS.

All three of the ^{252}Cf sources had the same geometry, so the same response functions were used to unfold solution spectra for all three sources. The response functions are illustrated in Fig. 6.8. As was the case for the proof-of-concept work performed in simulation space, the peak broadens and shifts toward higher energies with increased HDPE and thus increased neutron moderation [100]. Additionally, the magnitude and shape of the response functions of the inner and outer ring response functions are unique, so each measured count rate distinctively contributed towards the unfolding spectral problem.

MAXED and GRAVEL were used to unfold the solution spectrum for each neutron source and measurement individually. The quality of a solution spectrum is typically judged by how well the solution spectrum, when folded with each respective response function, agrees with the measured count rate data [40]. The two units of measure used to quantify this are the reduced chi-square value, χ^2/ν, and the calculated-to-measured ratios. The reduced chi-square value determines whether or not a statistically significant difference exists between the calculated and measured

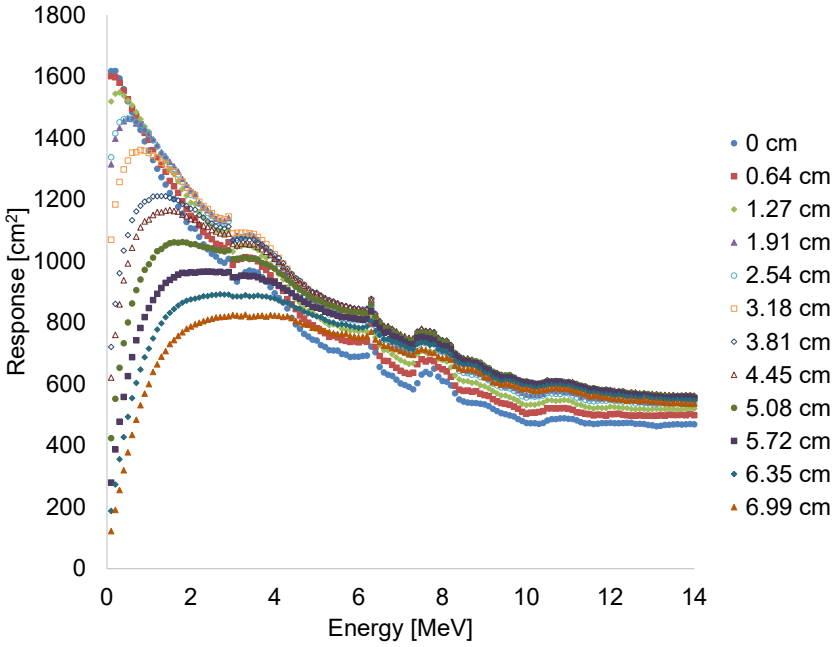

(a) Inner Ring

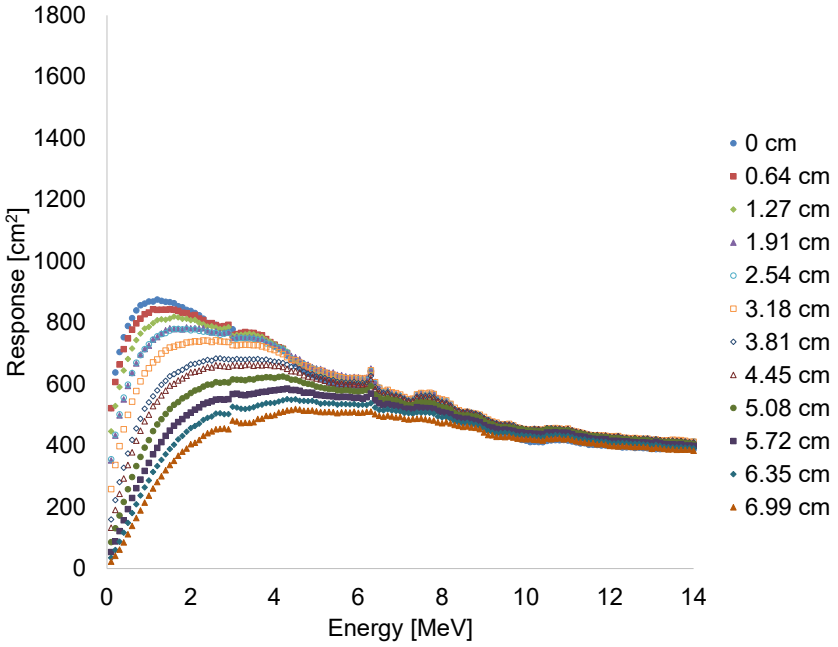

(b) Outer Ring

Figure 6.8: Response functions for ^{252}Cf neutron sources for different HDPE moderator wall thicknesses

count rate based on the significance level. In this work, the significance level was set to 1% and represented the probability that the calculated and measured count rates were statistically similar but determined to be different. The 1% significance for ^{252}Cf translated to critical values of 0.40–1.92 for 23 degrees of freedom. The degrees of freedom are equivalent to one less than the number of measured count rates entered into the algorithm or one less twice the number of moderators used for the measurements. The calculated-to-measured ratio, C_d/M_d, is a measure of how closely each calculated count rate compared to each corresponding measured count rate. The solution spectrum is considered to be close to the true spectrum if calculated-to-measured ratio is within 1-σ of unity for all count rate data [40]. Note that the uncertainty in the calculated-to-measured ratio is a measure of the statistical uncertainty in the measured data and not a measure of the uncertainty in the solution spectrum. The χ^2/ν and calculated-to-measured ratios are shown in Figs. 6.9, 6.10, 6.11 for FTC-Cf-1830, FTC-Cf-3010, and EZ Q9-304, respectively. The χ^2/ν values for all MAXED and GRAVEL solution spectra for all neutrons measurements were within the desired critical value range. This confirms that all solution spectra, when folded with the response functions, statistically agreed with the measured count rate data for each measurement. The calculated-to-measured ratios were within 1-σ of unity, shown as the gray horizontal line in each plot, for the majority of data points across all measurements. The data points not within 1-σ of unity were the outer ring count rate for the 3.81 cm wall thickness for measurement 1 for FTC-Cf-1830 and the 4.45 cm wall thickness for measurement 2 and 1.27 cm wall thickness for measurement 3 for EZ Q9-304. In each of these cases, the count rate was lower than expected. The cause of the lower count rate was not the result of human error, but likely due to a temporary electronics glitch. Ultimately, these data indicate that the solution spectra are a good solution for the measured data for all

^{252}Cf measurements [40].

The MAXED and GRAVEL solution spectra for each neutron source are pictured in Fig. 6.12. All solution spectra were indistinguishable for sources FTC-Cf-1830 and FTC-Cf-3010. Solution spectra for EZ Q9-304, however, were undifferentiated for measurements 1 and 2, but the solution spectra for measurement 3 could be differentiated from the other solution spectra. This was caused by an outlying count rate data point for the outer ring 1.27 cm moderator. The outlier was observed by the high calculated-to-measured ratio in Fig. 6.11c, which was likely the algorithm's attempt to adjust for the abnormally low count rate data point to produce a solution spectrum. To test the sensitivity to the outlying data point, MAXED and GRAVEL solution spectra were calculated for EZ Q9-304 measurement 3 without the count rate data point from the outer ring 1.27 cm moderator. The χ^2/ν values for MAXED and GRAVEL were within the desired critical value range and the calculated-to-measured ratios were within 1-σ of unity for all data points, as shown in Fig. 6.13b. The new solution spectra for measurement 3, when folded with the response functions, had improved agreement with the measured count rate data without the outlying count rate data point. The new solution spectra for measurement 3 are shown in Fig. 6.13a and compared to the solution spectra from measurements 1 and 2. All MAXED and GRAVEL solution spectra for EZ Q9-304 were undifferentiated with the removal of the outlying data point in the measurement 3 count rate data set. This result demonstrates the robust methodology of the algorithm to adapt to the measured data and not simply reproduce and verify that the input guess spectrum was a likely solution.

The solution spectra for MAXED and GRAVEL for all measurements for a neutron source were averaged and standard deviation calculated on a bin-by-bin basis to generate an averaged solution spectrum for each neutron source, because the agreement was good between MAXED and GRAVEL for each measurement and the

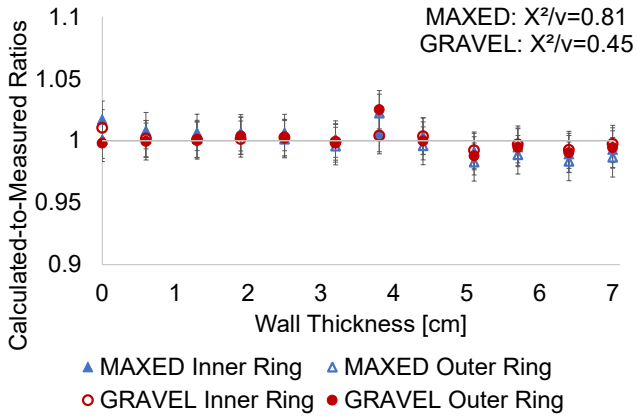

(a) Measurement 1

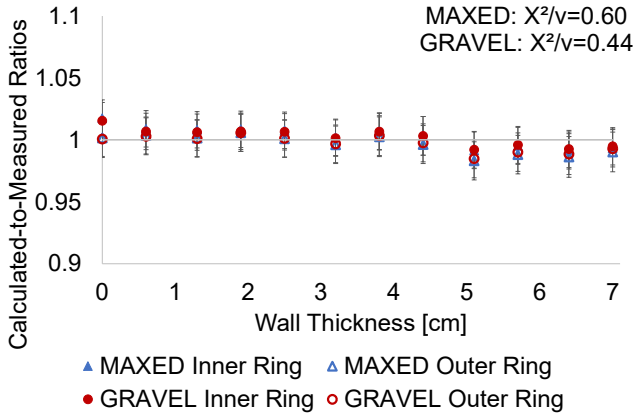

(b) Measurement 2

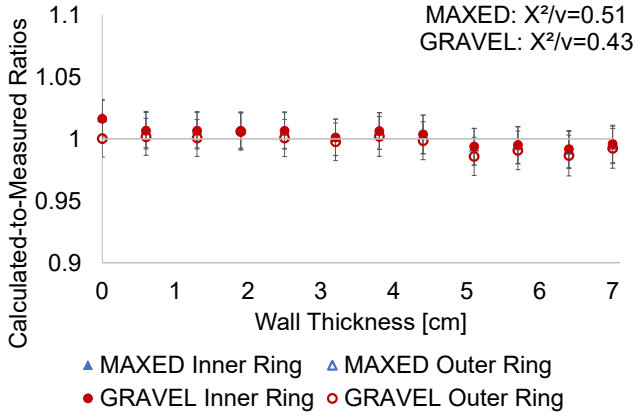

(c) Measurement 3

Figure 6.9: MAXED and GRAVEL calculated-to-measured ratios and χ^2/ν for triplicate measurement of FTC-Cf-1830

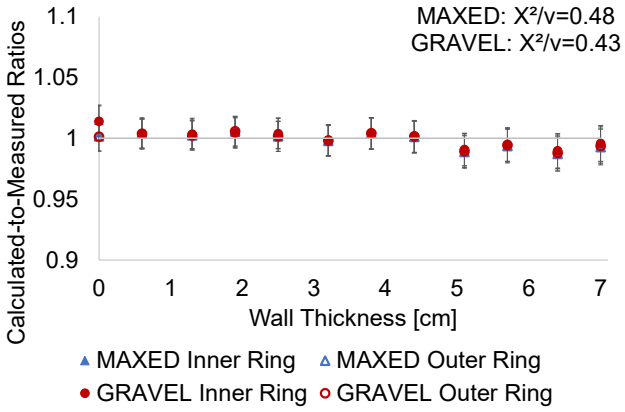

(a) Measurement 1

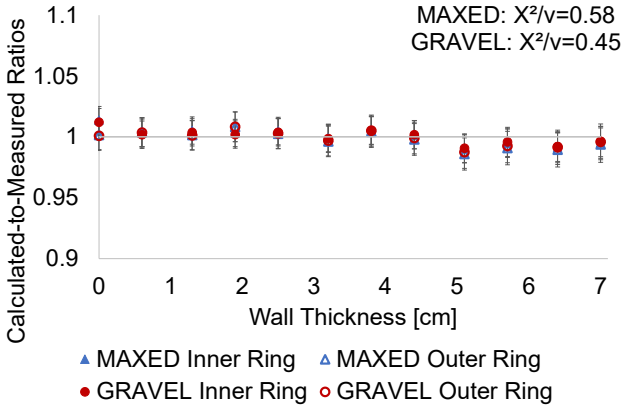

(b) Measurement 2

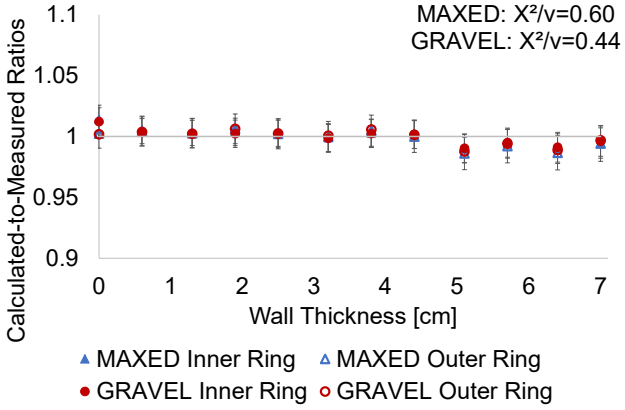

(c) Measurement 3

Figure 6.10: MAXED and GRAVEL calculated-to-measured ratios and χ^2/ν for triplicate measurements of FTC-Cf-3010

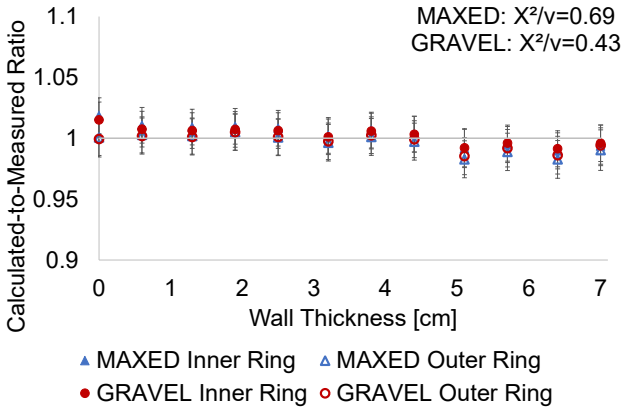

(a) EZ Q9-304

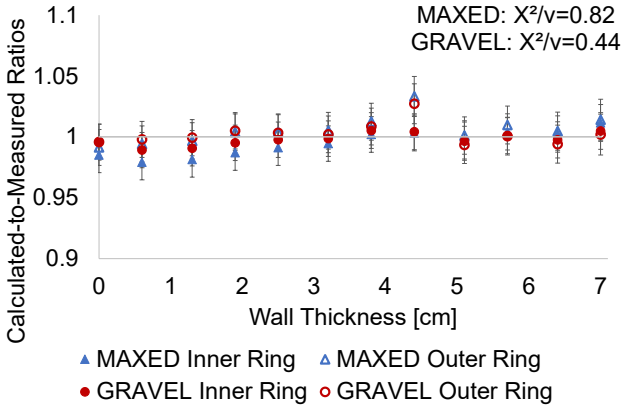

(b) Measurement 2

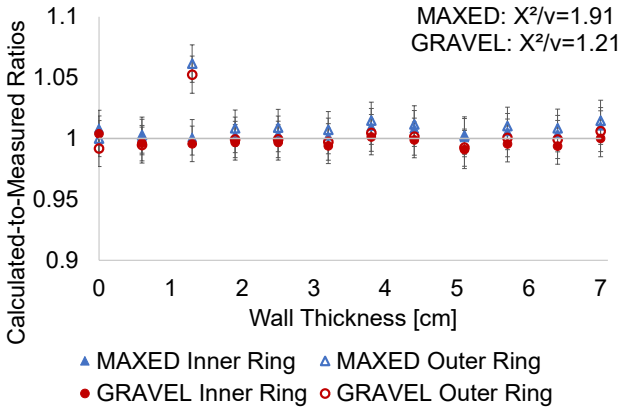

(c) Measurement 3

Figure 6.11: MAXED and GRAVEL calculated-to-measured ratios and χ^2/ν for triplicate measurement of EZ Q9-304

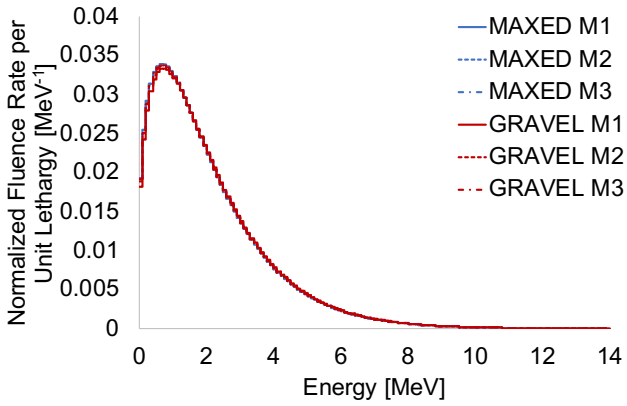

(a) FTC-Cf-1830

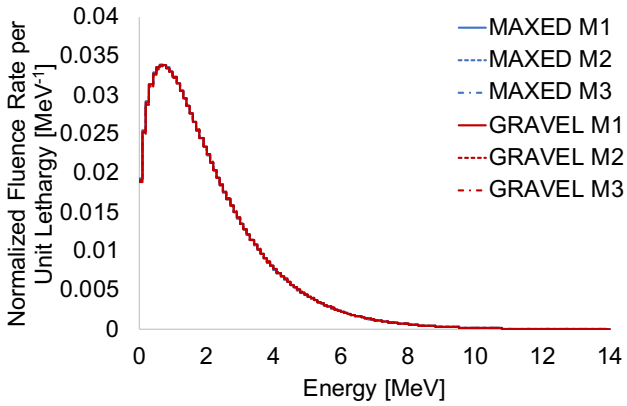

(b) FTC-Cf-3010

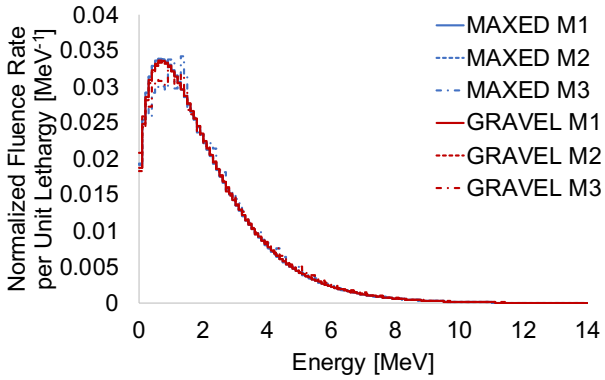

(c) EZ Q9304

Figure 6.12: MAXED and GRAVEL spectra for ^{252}Cf neutron sources measured in triplicate. M1, M2, and M3 are abbreviations for Measurement 1, 2, and 3, respectively.

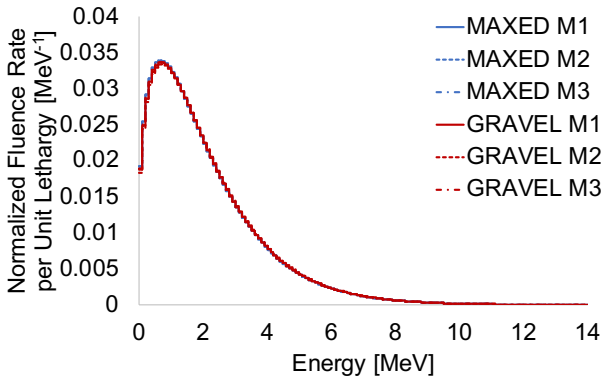

(a) Solution spectra

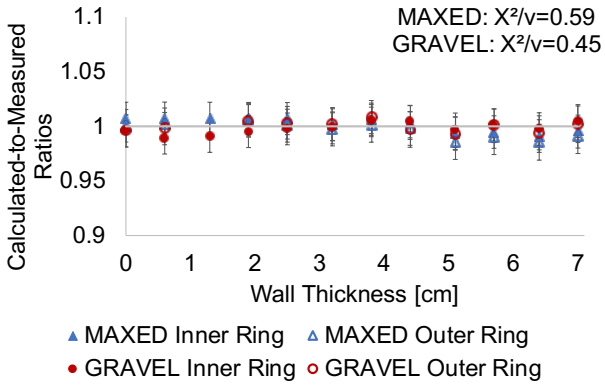

(b) Calculated-to-measured ratios for Measurement 3

Figure 6.13: MAXED and GRAVEL spectra for EZ Q9-304 measurement 3 unfolded without the outlying count rate data point for the outer ring 1.27 cm moderator and compared to the spectra for measurement 1 and 2. M1, M2, and M3 are abbreviations for Measurement 1, 2, and 3, respectively.

solution spectra and measured data. The solution spectra calculated without the outlying data point for EZ Q9-304 measurement 3 were included in the averaged spectrum for this source, because these spectra agreed with those from measurement 1 and 2. Although several algorithms, including MAXED, have the mathematical capability to calculate uncertainty on a bin-by-bin basis, quantifying uncertainty for a solution spectrum using a BSS algorithm is a difficult task because the uncertainty associated

with the response functions and input guess spectrum are not easily quantified. Often times, the response functions have unquantifiable biases and the input guess spectra have unknown uncertainty. Inputting values into an algorithm for these data would thus likely be incorrect, causing the final uncertainty in the solution spectrum to be misrepresented. By averaging the solution spectra from multiple measurements of the same source and geometry and calculating standard deviation, the uncertainty can better be quantified in a "top-down" approach that considers how the system change with slightly varying input within statistical limits. The averaged solution spectra for all sources are shown in Fig. 6.14 alongside the ^{252}Cf Watt fission spectrum. Error bars represent standard deviation. All neutron sources are within 1-σ of the ^{252}Cf Watt fission spectrum for each energy bin despite the outlying spectrum for EZ Q9-304. The agreement between the neutron energy spectrum for each source and the ^{252}Cf Watt fission spectrum further confirms that, despite the differences in source age between these sources [71], the neutron energy spectra resemble a pure ^{252}Cf source. Either the neutron emissions from secondary neutron emitters are negligible, as suggested earlier, or the neutron energy spectra cannot be distinguished within the sensitivity of the iBSS from a ^{252}Cf Watt fission spectrum. Neither ^{250}Cf or ^{248}Cm fission spectra are well-known, so differences between them and the ^{252}Cf Watt fission spectrum cannot be established. Ultimately the iBSS spectral agreement with the ^{252}Cf Watt fission spectrum demonstrated reproducibility of the iBSS for several ^{252}Cf sources and proof-of-concept for the iBSS using experimental data. Establishing that the iBSS can be used in the experimental space means that its uses can be expanded, including benchmarking it to SOURCES-4C.

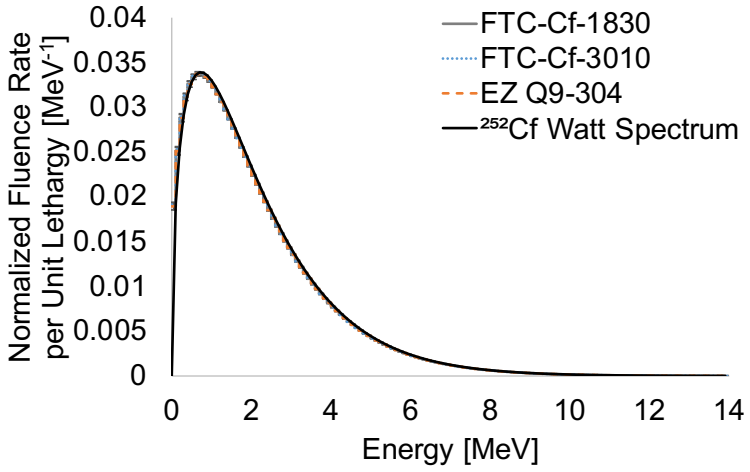

Figure 6.14: Averaged solution spectra for three ^{252}Cf sources measured using the iBSS of the averaged MAXED and GRAVEL solution spectra. Error bars represent standard deviation from the averaged MAXED and GRAVEL solution spectra.

6.3.2 Plutonium-240

ORNL has a high-purity $^{240}PuO_2$ source that served to establish the iBSS as a tool for experimentally verifying neutron energy spectra generated by SOURCES-4C. The source material composition was determined by mass spectrometry and isotopically consists of more than 99% ^{240}Pu. Isotopic information is listed in Table 6.2. Other Pu isotopes that typically need to be considered–spontaneous fission from even-numbered isotopes and the $^{17,18}O(\alpha,n)$ reaction from $^{239}PuO_2$–negligibly contribute to the neutron emission. The high-purity and well-known source composition thus make this an ideal source for benchmarking the iBSS to SOURCES-4C.

Table 6.2: Isotopic information for the high-purity $^{240}PuO_2$ source

Isotope	Isotopic Abundance [%]
^{238}Pu	$9.89 \cdot 10^{-3}$
^{239}Pu	$6.72 \cdot 10^{-2}$
^{240}Pu	99.8
^{241}Pu	$4.79 \cdot 10^{-3}$
^{242}Pu	$1.14 \cdot 10^{-1}$

The $^{240}PuO_2$ source was measured in the LVAWCC and solution spectra unfolded in MAXED and GRAVEL for each data set. Response functions, pictured in Fig. 6.15, were generated in MCNP using a system geometry that matched the physical system. Strong agreement was observed between the calculated count rate and the measured count rate for each data set. The χ^2/ν values were within the desired critical value range of 0.36–1.50 for 19 degrees of freedom, and the calculated-to-measured ratios were within 1-σ of unity for all measurements, as shown in Fig. 6.16. Note that the calculated-to-measured ratios for all count rates in each data set were less than 1% from unity, which is the smallest margin between the measured count rates and calculated count rates estimated in this work and within the measurement uncertainty. Because the three independent data set for the $^{240}PuO_2$ source agreed, the MAXED and GRAVEL solution spectra for each data set were averaged and standard deviation calculated to generate an averaged solution spectrum for the $^{240}PuO_2$ source. The averaged solution spectrum is shown in Fig. 6.17. All energy bins were within 1-σ of the spectrum generated by SOURCES-4C. The statistical agreement between the two spectra confirms that the iBSS can be used as a tool for benchmarking neutron energy spectra in SOURCES-4C.

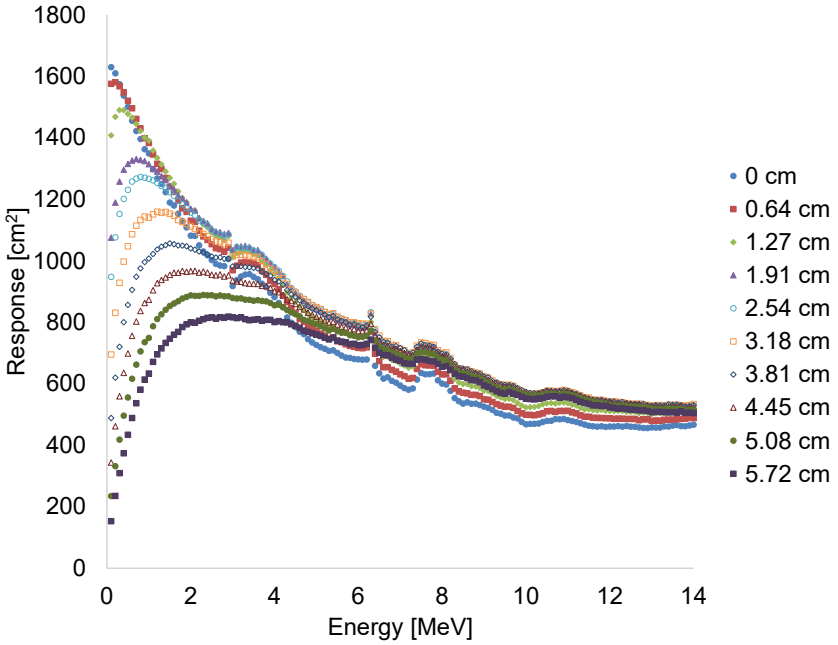

(a) Inner Ring

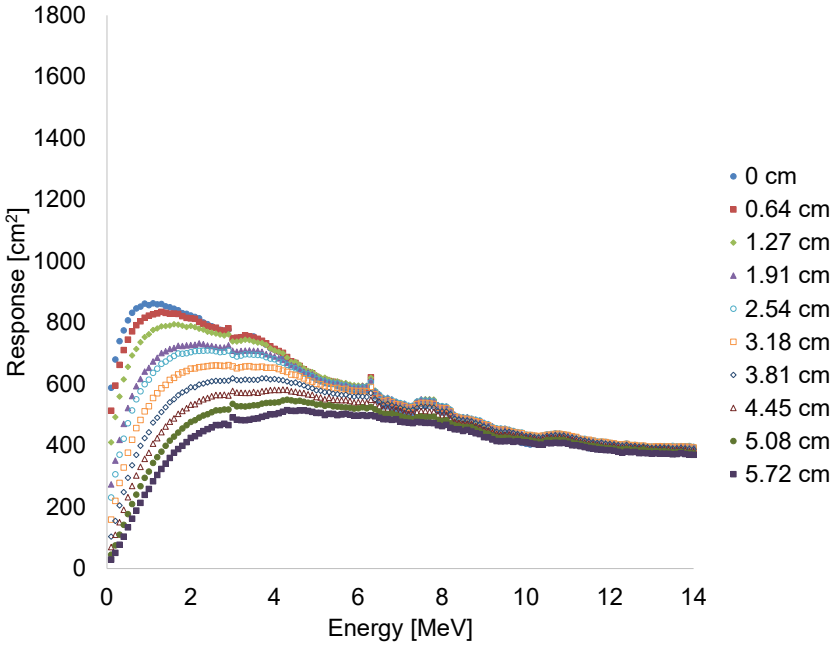

(b) Outer Ring

Figure 6.15: Response functions for the high-purity $^{240}PuO_2$ source for different HDPE moderator wall thicknesses

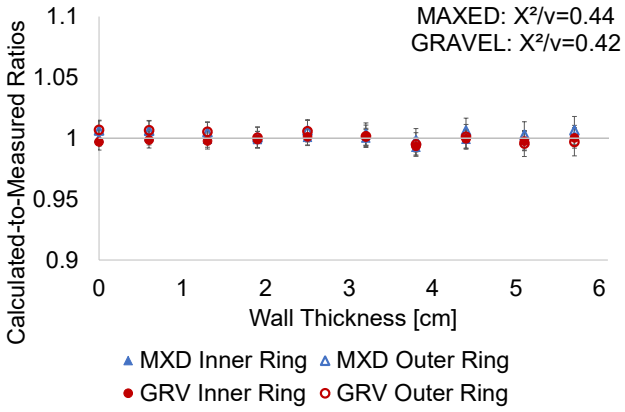

(a) Measurement 1

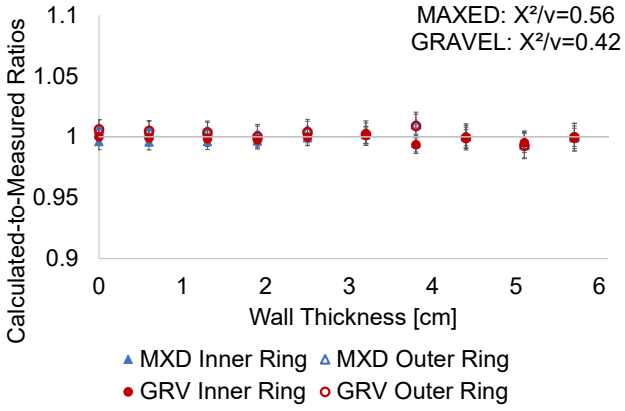

(b) Measurement 2)

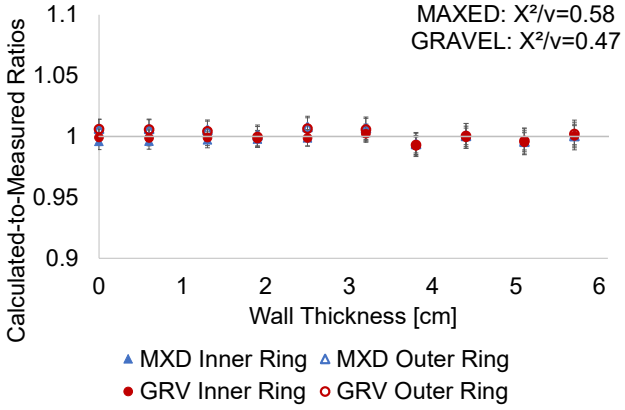

(c) Measurement 3

Figure 6.16: MAXED and GRAVEL calculated-to-measured ratios and χ^2/ν for triplicate measurement of the high-purity $^{240}PuO_2$ source

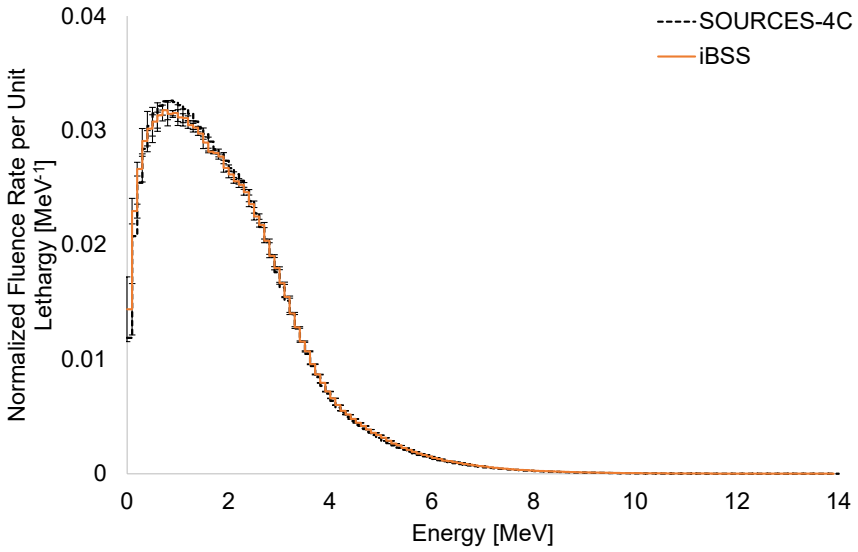

Figure 6.17: Averaged MAXED and GRAVEL solution spectra for the high-purity $^{240}PuO_2$ source measured using the iBSS. Error bars represent standard deviation from the averaged MAXED and GRAVEL solution spectra for triplicate measurement of the source.

Although this benchmarking study between SOURCES-4C and the iBSS was limited to a single source, the number of benchmarking studies for neutron energy spectra in SOURCES-4C is also limited. The PuO_2 benchmark study, on the other hand, used higher quality data and relied on data from multiple neutron sources with different Pu isotopic compositions. Additionally, the source used here was well-characterized and had less than 1% associated uncertainty with each measured count rate. Together the robust benchmark studies previously completed for PuO_2 in SOURCES-4C and high-quality measurement presented here provided the best benchmark for the iBSS to SOURCES-4C.

6.3.3 AmLi

The neutron energy spectrum for the AmLi (α, n) reaction has been measured experimentally and via calculations or simulations [2, 3, 10–12]. However, there is an

ongoing debate in the literature regarding the true neutron energy spectrum for AmLi. The composition of AmLi sources is not well known and consists of a heterogeneous mixture of AmO_2 and Li, LiH, or LiOH [11]. The additional H and O components in the source matrix can produce additional source terms in the neutron energy spectrum that are difficult to account for due to the unknown nature of the source composition. These unknowns in the source composition thus make it difficult to separate the Li(α, n) component from these extraneous components to determine the true neutron energy spectrum for the AmLi (α, n) reaction. Additionally, recent studies suggest that the AmLi neutron energy spectrum generated by SOURCES-4C under estimates the the soft end of the spectrum [3, 11]. The iBSS was utilized to provide additional experimentally-determined data to the literature and offer another comparison for SOURCES-4C.

Gamma-ray spectra were first collected for the AmLi sources to determine if there was a Be impurity in the source and determine whether or not it could be quantified. The spectra were collected using an n-type high-purity germanium detector (Model GL2820R/S, Canberra Industries, Meriden, Connecticut) for 68 h for the C-series sources and 48 h for the N-series sources. The resulting spectra are shown in Fig. 6.18 for AN-HP-C272 and Fig. 6.19 for AN-HP-N458. A gamma-ray peak at 4.468 MeV was present in the AN-HP-C272 gamma-ray spectrum, but not in the AN-HP-N458 spectrum. This gamma-ray is emitted from the ^{9}Be(α, n) reaction and indicated that ^{9}Be is a contaminant in the C-series sources, but not in the N-series sources. However, the quantity of ^{9}Be in the C-series sources could not be quantified, because the neutron-to-gamma ratio of the ^{9}Be(α, n) reaction is not well-known. Additionally, the quantity would need to be calibrated from an AmBe source, but, like AmLi sources, the composition of the source material is not documented. Without knowledge of the ^{9}Be content in AmBe sources or the neutron-to-gamma

ratio of the reaction, the Be contaminant in the C-series sources was not able to be quantified. Previous work also indicated that the iBSS cannot identify or quantify the Be contaminant in a source, so Be was not included in the input guess spectrum for the C-series sources [100].

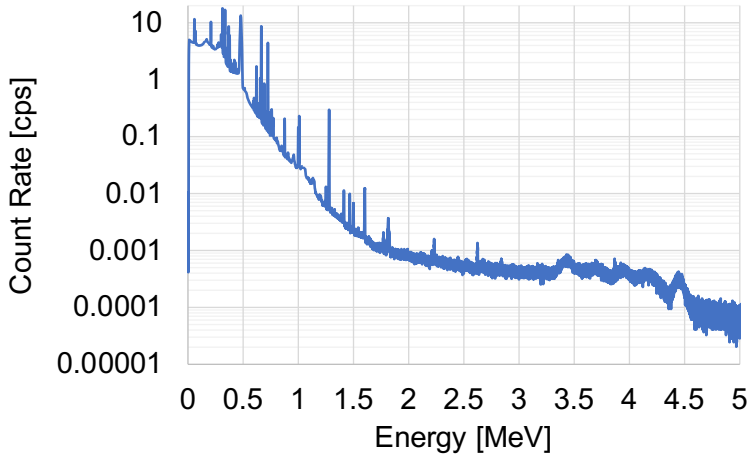

Figure 6.18: Gamma-ray spectrum for AmLi source AN-HP-C272

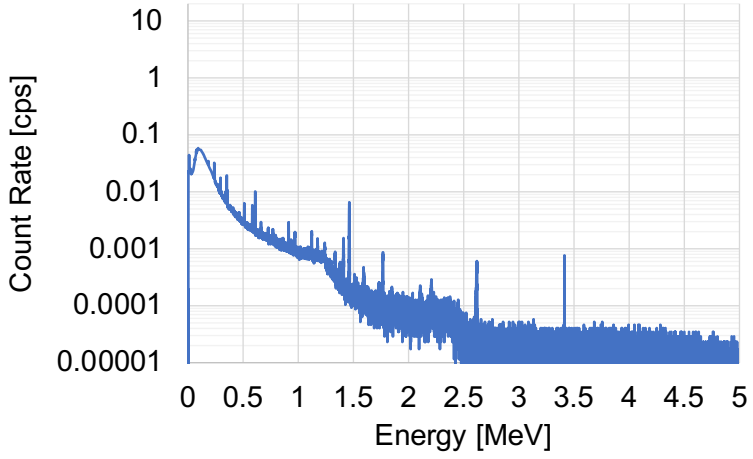

Figure 6.19: Gamma-ray spectrum for AmLi source AN-HP-N458

Solution spectra were unfolded using the MAXED and GRAVEL algorithms for four AmLi sources. All AmLi sources had similar geometry, so a single set of response functions, pictured in Fig. 6.20, were generated for unfolding the neutron energy spectrum for these sources. The MAXED and GRAVEL solution spectra for all measurements, when folded with the response functions, statistically agreed with the measured data. The χ^2/ν values were within the desired critical value range (0.36–1.50 for 19 degrees of freedom) and the calculated-to-measured ratios were within 1-σ of unity for all measurements, as shown in Figs. 6.21. The MAXED and GRAVEL solution spectra had good relative agreement for all measurements for each individual source. A single solution spectrum was calculated for each AmLi source by averaging and calculating the standard deviation from all MAXED and GRAVEL solution spectra for triplicate measurement of each source. The resulting averaged solution spectra are shown in Fig. 6.25 on a linear and semi-logarithmic scale. The C-series averaged solution spectra (AN-HP-C268 and AN-HP-C272) and N-series (AN-HP-N458 and AN-HP-N459) averaged solution spectra agreed to within 1-σ for the sources within each series. The averaged solution spectra for the sources in each series was expected to agree, because the source material came from the same batch of material. However, the C-series and N-series averaged solution spectra do not agree to within 1-σ, likely because they have different source compositions. Each series of source has an unknown H and O content that ultimately affected the final averaged solution spectrum. From Fig. 6.25b, the averaged solution spectrum indicated that the C-series AmLi sources had more ^{17,18}O(α, n) neutron emissions than the N-series AmLi sources. The excess ^{17,18}O(α, n) could have distorted the ^{7}Li(α, n) portion of the spectrum, as suggested by simulation studies [100]. Although the inverse Bonner sphere concept was proposed as a method to characterize individual AmLi sources because of the aforementioned differences in source material composition [13], the

purpose of the present work was to experimentally measure a general spectrum for the ^{7}Li(α, n) reaction and compare it to SOURCES-4C.

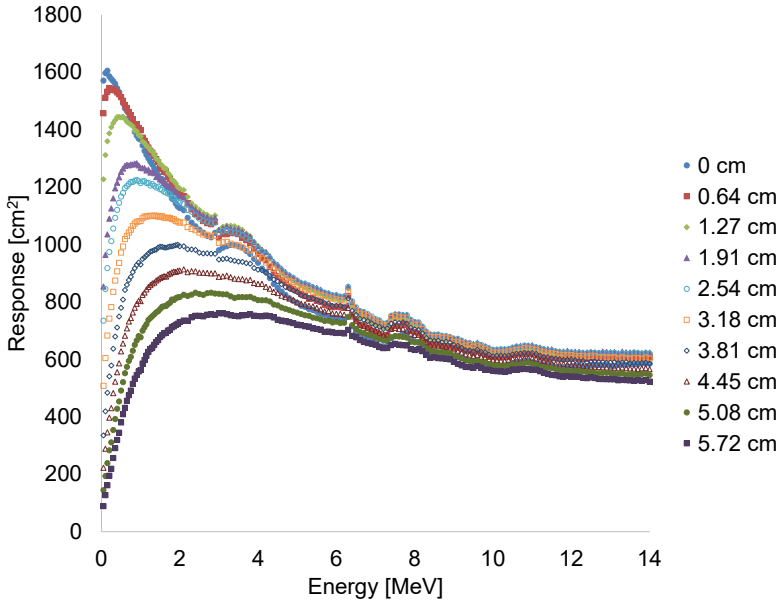

(a) Inner Ring

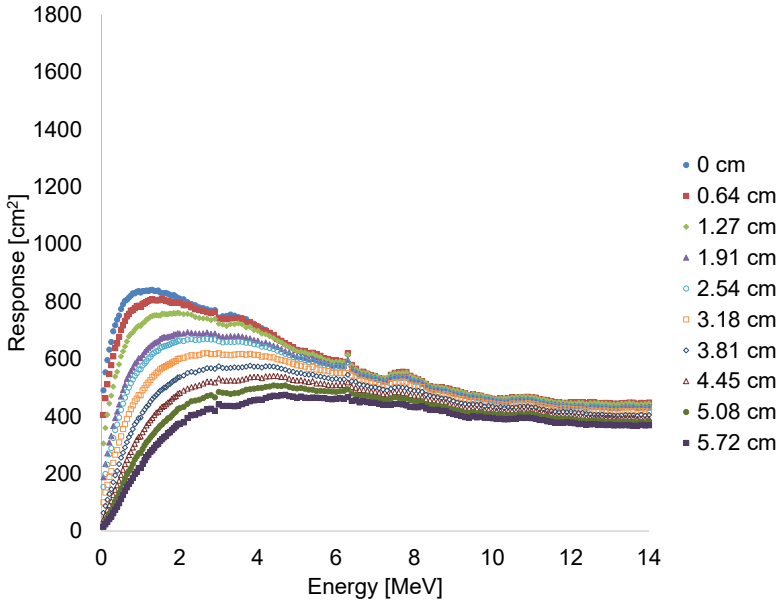

(b) Outer Ring

Figure 6.20: Response functions for AmLi neutron sources for different HDPE moderator wall thicknesses

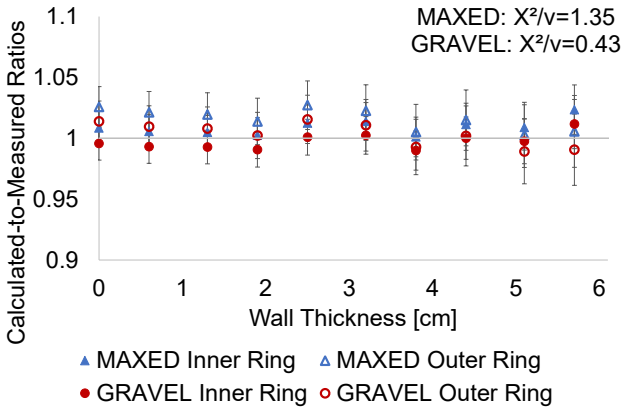

(a) Measurement 1

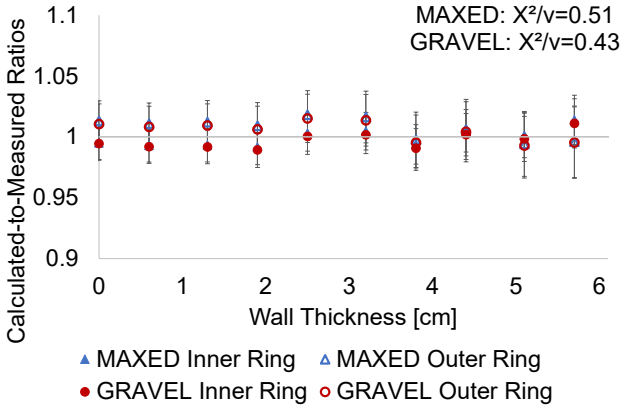

(b) Measurement 2

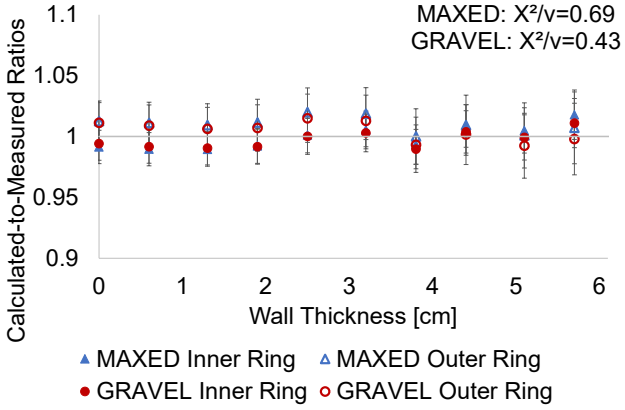

(c) Measurement 3

Figure 6.21: MAXED and GRAVEL calculated-to-measured ratios and χ^2/ν for triplicate measurement of AN-HP-C268

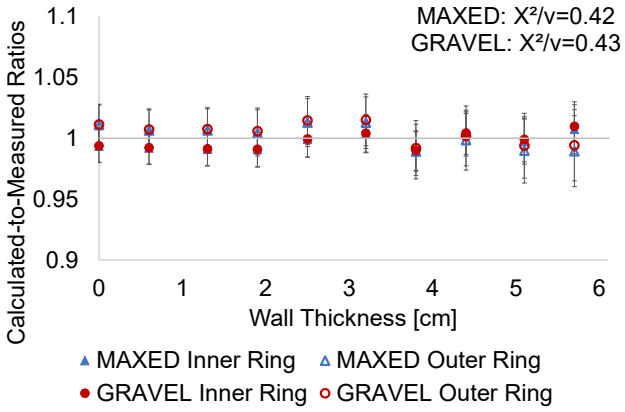

(a) Measurement 1

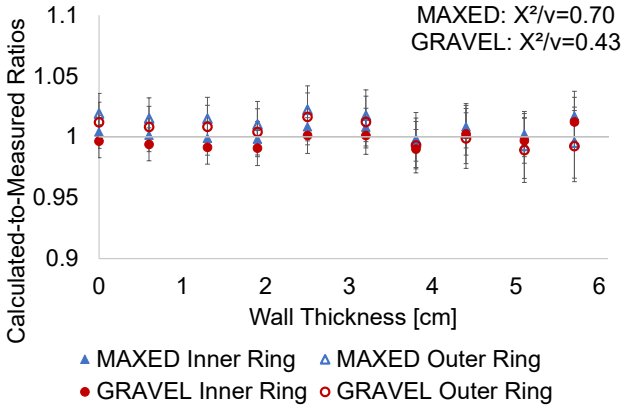

(b) Measurement 2

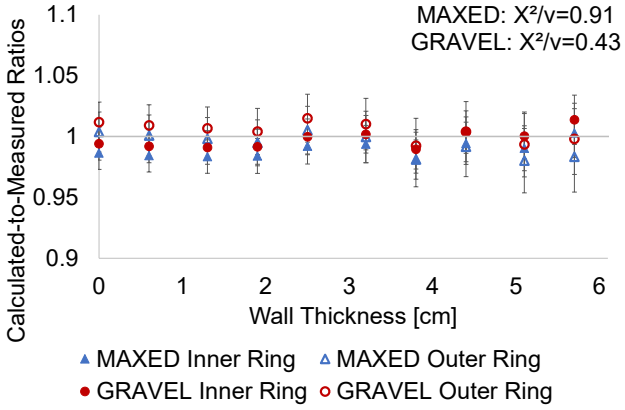

(c) Measurement 3

Figure 6.22: MAXED and GRAVEL calculated-to-measured ratios and χ^2/ν for triplicate measurement of AN-HP-C272

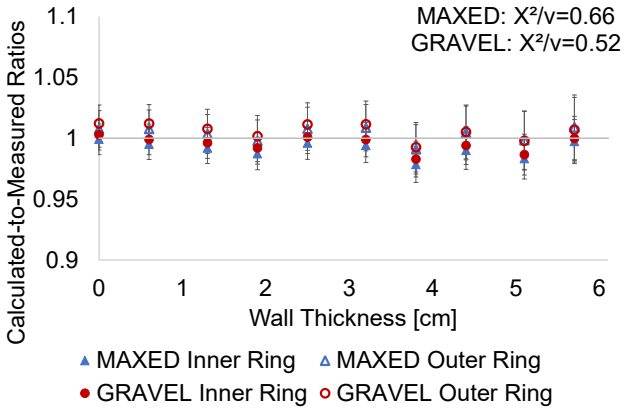

(a) Measurement 1

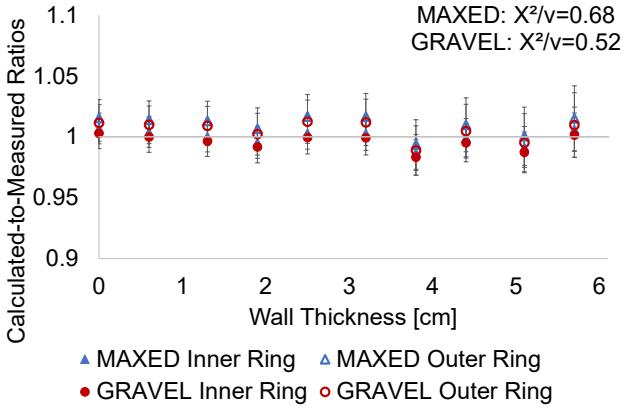

(b) Measurement 2

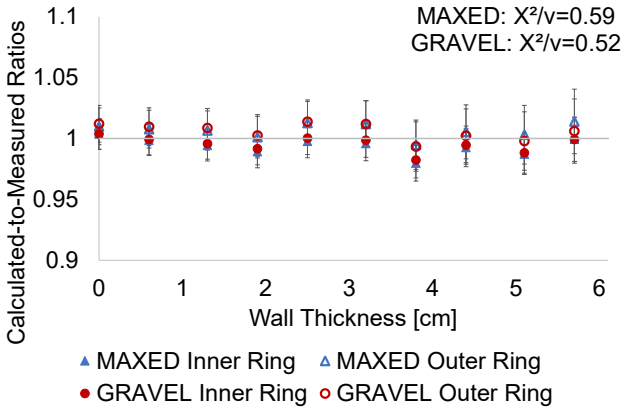

(c) Measurement 3

Figure 6.23: MAXED and GRAVEL calculated-to-measured ratios and χ^2/ν for triplicate measurement of AN-HP-N458

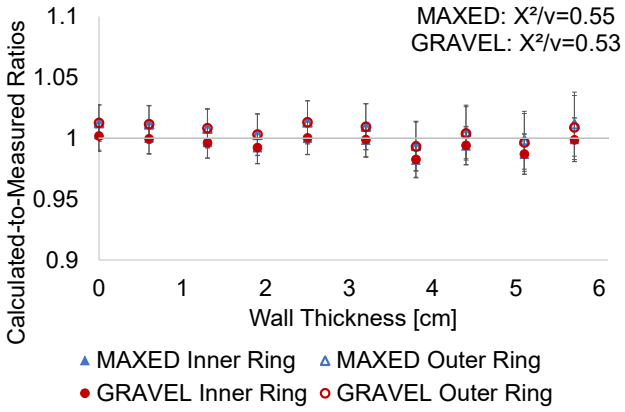

(a) Measurement 1

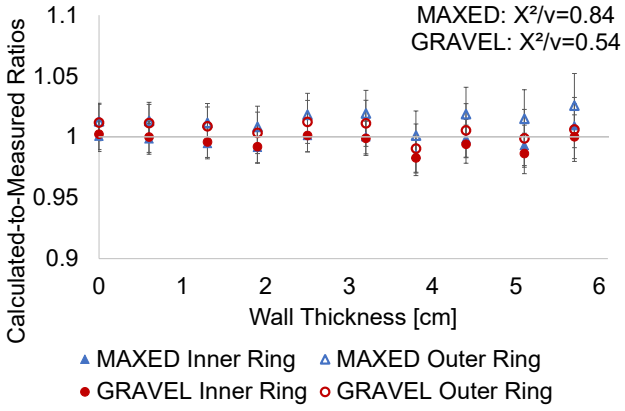

(b) Measurement 2

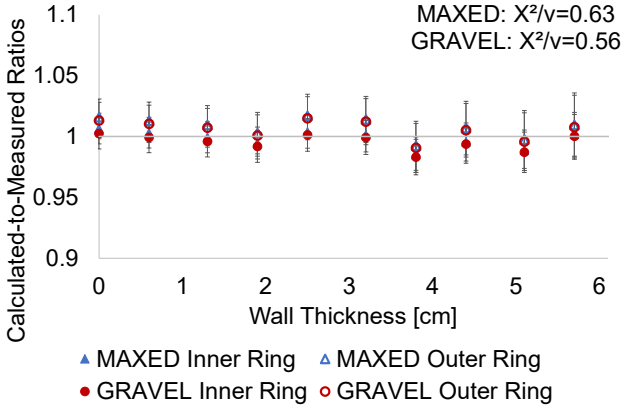

(c) Measurement 3

Figure 6.24: MAXED and GRAVEL calculated-to-measured ratios and χ^2/ν for triplicate measurement of AN-HP-N459

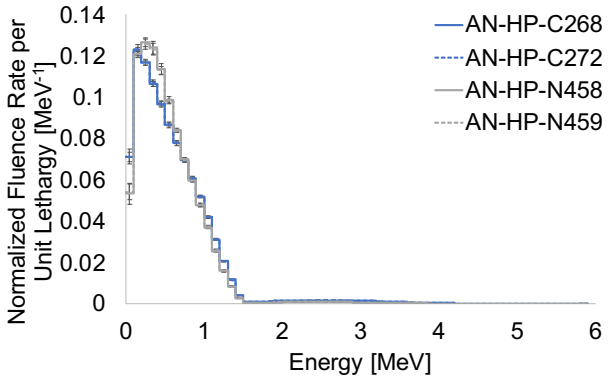

(a) Linear Scale

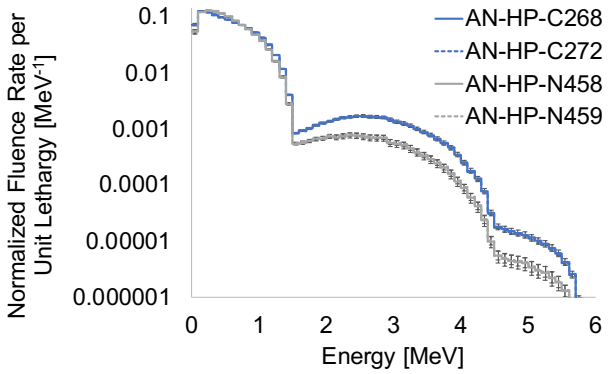

(b) Semi-logarithmic Scale

Figure 6.25: Averaged solution spectra from MAXED and GRAVEL for each AmLi source. Error bars represent standard deviation from the averaged MAXED and GRAVEL solution spectra.

A general spectrum for the ^{7}Li(α, n) reaction from AmLi sources was created by averaging the solution spectra from all AmLi sources to average out the affects from differing source compositions mainly due to differences in the ^{17,18}O content. The general iBSS AmLi (α, n) spectrum is shown in Fig. 6.26 and compared to Geiger and van der Zwan [2], Tagziria [3], and SOURCES-4C. The general spectrum had good relative agreement with Geiger and van der Zwan, which was determined via calculations that accounted for α-decay from ^{241}Am, (α, n) cross sections, and α stopping powers. Tagziria [3] had a peak at the soft end of the spectrum that

was not observed in the iBSS spectrum. The AmLi spectrum in Tagziria [3] was determined using three different neutron spectrometry methods for a single AmLi source. Although all of the methods agreed, Tagziria [3] suggested and confirmed via MCNP simulations that the peak was from H in the source. Later work from Tagziria (2012) [12] proposed an ideal AmLi spectrum based on measurements and simulations that agrees well with Geiger and van der Zwan [2]. This collection of work suggests that SOURCES-4C is underpredicting the ^{7}Li(α n) neutron energy spectrum for AmLi and should be updated to reflect the growing body of literature that experimentally confirms the spectrum proposed by Geiger and van der Zwan [2].

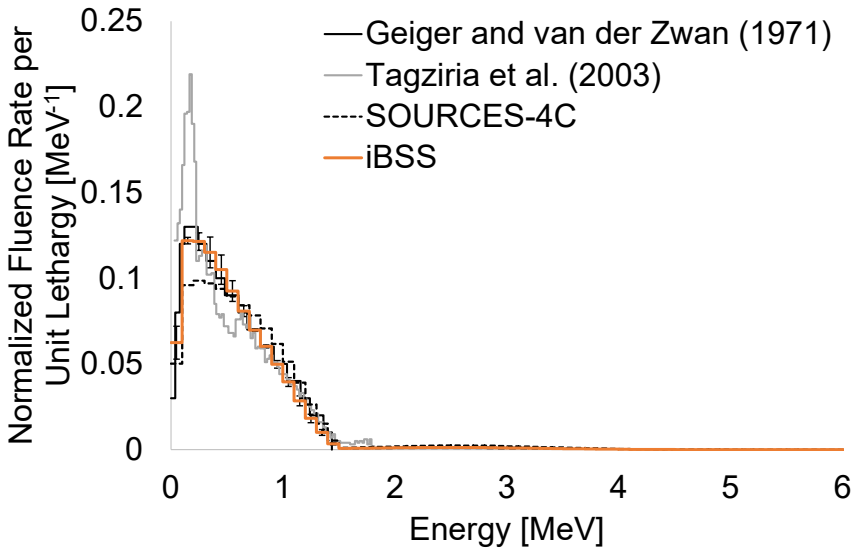

Figure 6.26: General AmLi spectrum measured using the iBSS and compared to Geiger and van der Zwan [2], Tagziria [3], and SOURCES-4C. Error bars on the iBSS spectrum represent standard deviation from the averaged MAXED and GRAVEL solution spectra.

6.3.4 AmBe

The ^{9}Be(α,n) neutron energy spectrum was benchmarked using experimental data for PuBe and PoBe in SOURCES-4C. However, the data used for these studies

were outdated and only agreed with experimental data to 18% [9, 102]. Additionally, the SOURCES-4C spectrum has not been benchmarked to experimental results specifically for the AmBe (α,n) reaction.

The iBSS was used to measure an AmBe source and provide an experimental comparison to the SOURCES-4C spectrum. The response functions used for the unfolding are illustrated in Fig. 6.27. The solution spectra produced by MAXED and GRAVEL for each measurement had good agreement with the measured count rate data. The χ^2/ν values were within the desired critical value range of 0.40–1.92 for 23 degrees of freedom. The calculated-to-measured ratios were also within 1-σ of unity for all count rate data, further confirming the excellent agreement between the solution spectrum and measured data. The solution spectra for MAXED and GRAVEL were indifferentiable and thus averaged and standard deviation calculated to create a general iBSS spectrum for the AmBe source measured here. The general iBSS solution spectrum is shown in Fig. 6.29 alongside the SOURCES-4C spectrum and a high-resolution AmBe spectrum experimentally measured by Marsh [4] for comparison. The general shape of the iBSS, Marsh [4], and SOURCES-4C spectra are similar, but the magnitudes of each spectrum do not agree across the full energy range. The most notable discrepancy occurred at the soft end of the spectrum, where the iBSS and Marsh [4] suggested the peak at approximately 1 MeV has a magnitude three times larger than predicted by SOURCES-4C. Additionally, Marsh [4] resolved a peak at approximately 10 MeV that was not present in either the iBSS or SOURCES-4C spectrum. The benchmark study described here involved only a single AmBe source. Although the iBSS solution spectra did not agree with the SOURCES-4C spectrum, it does not mean that the SOURCES-4C spectrum is incorrect, because the iBSS also did not agree across the full energy with Marsh [4], another experimentally measured AmBe spectrum. The AmBe spectra illustrated in Fig. 6.29 simply show that the

SOURCES-4C spectrum did not agree with this AmBe source or the AmBe source measured by Marsh [4]. A more robust benchmarking study involving additional AmBe sources needs to be conducted. Ultimately, the SOURCES-4C AmBe neutron energy spectrum cannot be confirmed to align with experimental data, but it's not clear what the true spectrum is for the AmBe (α, n) reaction.

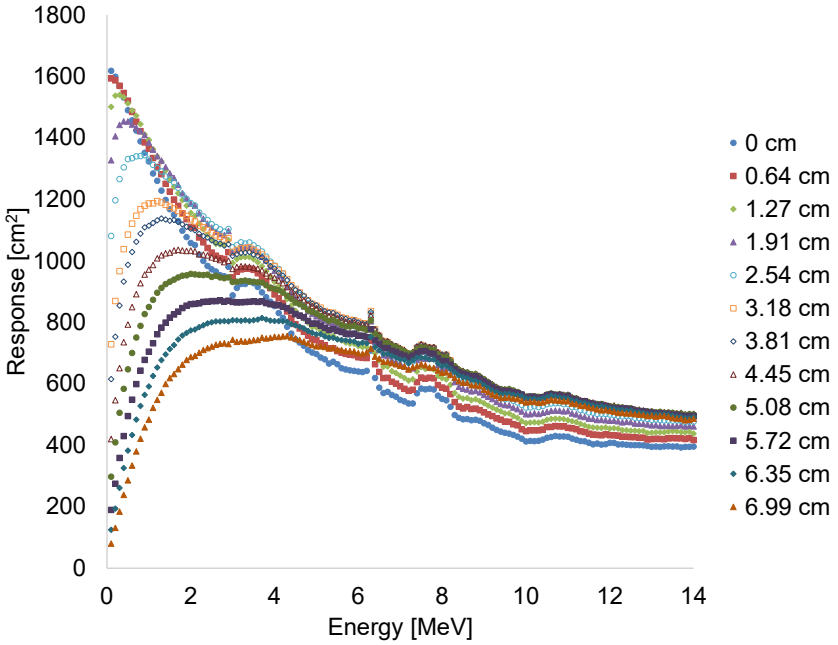

(a) Inner Ring

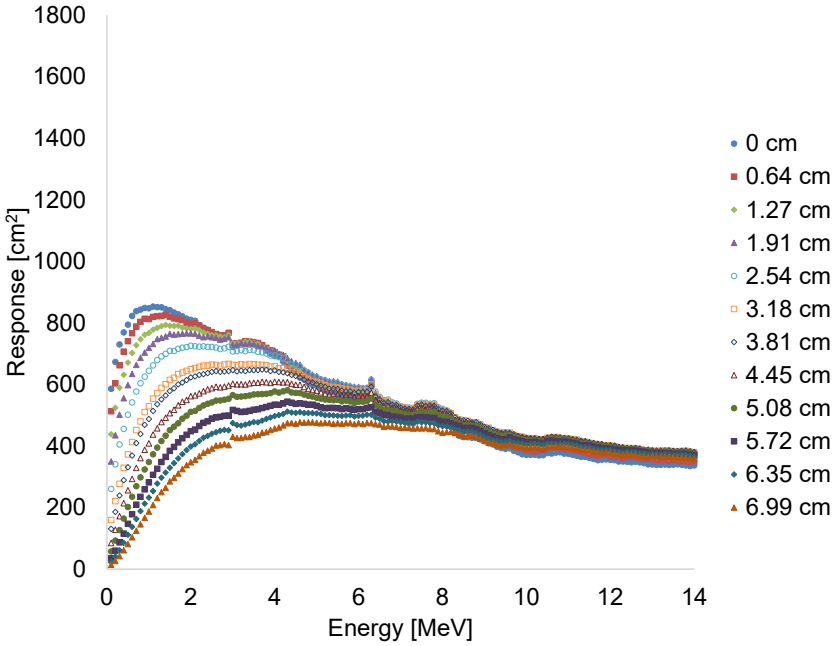

(b) Outer Ring

Figure 6.27: Response functions for AmBe neutron sources for different HDPE moderator wall thicknesses

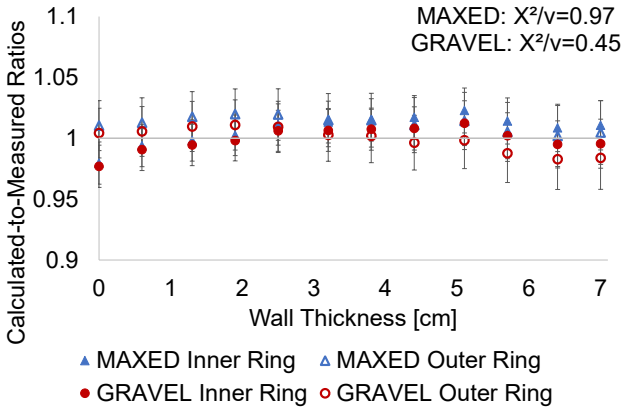

(a) Measurement 1

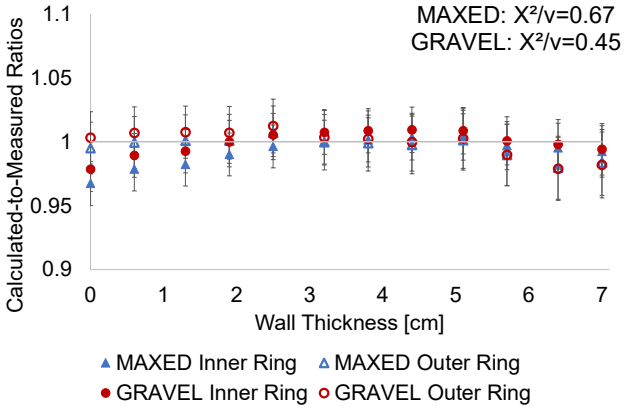

(b) Measurement 2

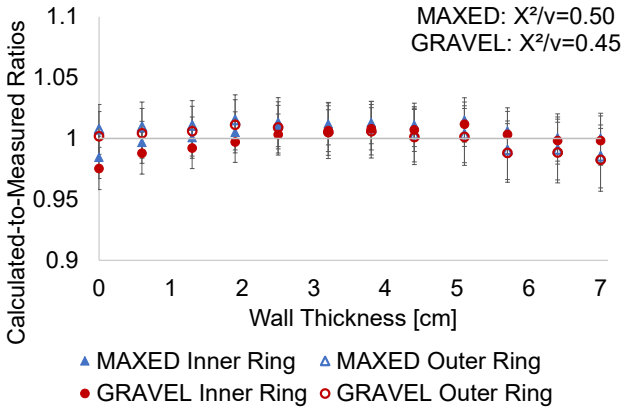

(c) Measurement 3

Figure 6.28: MAXED and GRAVEL calculated-to-measured ratios and χ^2/ν for triplicate measurement of the AmBe source

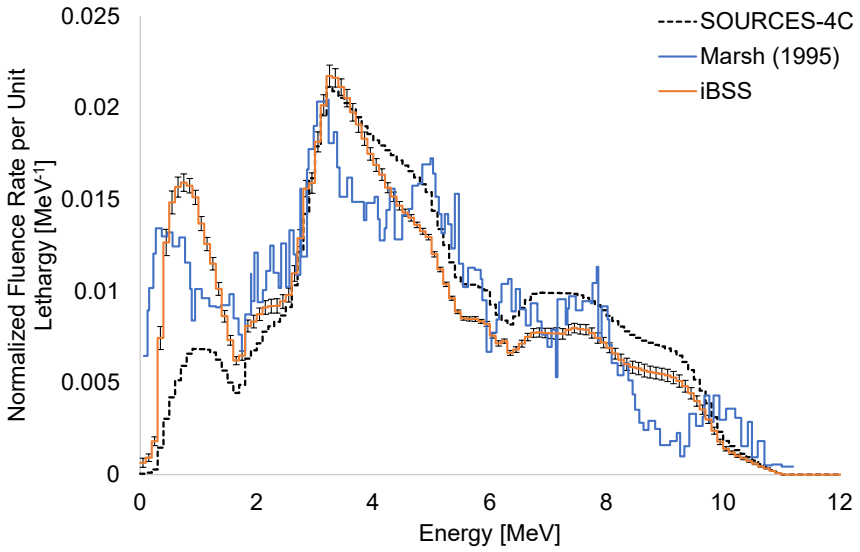

Figure 6.29: Averaged spectrum measured by the iBSS for the AmBe (α, n) reaction and compared to SOURCES-4C and Marsh [4]. Error bars on the iBSS spectrum represent standard deviation from the averaged MAXED and GRAVEL solution spectra.

6.4 Conclusions

The iBSS has the potential to be a verification tool for experimentally determining neutron energy spectra in SOURCES-4C. Solution spectra measured using the iBSS for ^{252}Cf and $^{240}PuO_2$ agreed to within 1-σ of the expected spectrum, indicating that the iBSS can accurately unfold neutron energy spectra and can thus be used as a verification tool. The agreement between the iBSS and SOURCES-4C for PuO_2 confirms that the iBSS can be used to verify neutron energy spectra in SOURCES-4C using experimental data.

AmLi and AmBe did not, however, agree with the SOURCES-4C neutron energy spectra. Neither spectra in SOURCES-4C has been previously been benchmarked to experimental data. The general AmLi spectrum measured by the iBSS aligned more closely with the spectrum proposed by Geiger and van der Zwan [2]

than SOURCES-4C. Other experimental works [3, 10, 12] also agree with Geiger and van der Zwan [2], suggesting that SOURCES-4C should be updated to reflect experimental data. The current experimentally-determined AmBe spectra by the iBSS and Marsh [4] do not agree with each other or with SOURCES-4C. A more robust benchmark study with additional AmBe sources should be conducted to establish an accepted AmBe (α, n) neutron energy spectrum prior to suggesting SOURCES-4C be updated.

Chapter 7

Conclusions & Future Work

The accuracy of neutron measurements in international safeguards is dependent on the knowledge of the significant sources of neutron emissions. The neutron energy spectrum of (α, n) reactions are often times not well known. A novel neutron spectrometer using the inverse Bonner sphere concept was developed to experimentally establish neutron energy spectra for neutron emitters commonly encountered in international safeguards. The key elements of this process included confirming technical data sheet information for ^{252}Cf sources to be used in experimental verification of the iBSS using high-resolution gamma-ray spectroscopy, demonstrating proof-of-concept and performing sensitivity analyses using MCNP simulations, and experimentally measuring neutron energy spectra using the iBSS method.

Development of the iBSS was dependent on well-characterized ^{252}Cf, because it has a well-known fissioning system and can be approximated to a point. However, a discrepancy was noted between the doubles-to-singles ratio for a newly purchased ^{252}Cf calibration source. A methodology was developed using high-resolution gamma-ray spectroscopy to confirm the source age and isotopic ratios on the technical data sheets. The spontaneous fission product gamma-ray lines and Bateman equations

were used to estimate the source age. Previous work [80] developed a similar methodology, but only accounted for ^{252}Cf in the calculation. This work expanded upon the previous work by including contributions to the spontaneous fission product gamma-ray lines from ^{250}Cf and ^{248}Cm–two spontaneous fission isotopes that are inevitably present in ^{252}Cf sources. Additionally, the odd-numbered Cf isotopes were used to confirm the isotopic ratios on the technical data sheet. Only source age and isotopic ratios on the technical data sheet for one ^{252}Cf source could be confirmed using this methodology. The discrepancies revealed regarding source age and isotopic ratio did not, however, explain the discrepancy between the doubles-to-singles ratios of ^{252}Cf sources used at ORNL for calibrating neutron counters for international safeguards. The estimated source age would not change the neutron energy spectrum significantly and could thus still be used for this work. Experimental measurement of these three ^{252}Cf sources in Chapter 6 confirmed that the neutron energy spectrum had good relative agreement with the ^{252}Cf Watt fission spectrum. However, the cause of the different doubles-to-singles ratios was not determined and needs to be studied further.

MCNP simulations were used to demonstrate proof-of-concept and perform sensitivity analyses. The proof-of-concept was demonstrated using an ideal scenario where the response functions perfectly mirrored the geometry and the input guess spectrum was the correct solution. In the ideal scenario, MAXED and GRAVEL, the unfolding algorithms, successfully unfolded the ^{252}Cf spontaneous fission spectrum, AmBe (α,n) spectrum, and AmLi (α,n) spectrum using the iBSS. Sensitivity studies compared the response from the ideal scenario to less-than-ideal scenarios, including response functions that did not match the exact geometry of the system and input guess spectra with limited *a priori* information. In both cases, the solution spectra had a larger relative error than the ideal scenario, indicating that the quality of the solution spectra measured using the iBSS has a strong dependence on the quality of

the response functions and input guess spectrum. Neutron measurements in international safeguards are typically verification measurements, so the dependence on a well-characterized system makes the iBSS uniquely suited to international safeguards measurements. The iBSS ultimately has the potential to have a broad impact on international safeguards for verification measurements. Additional sensitivity studies should be performed to study how small of an anomaly in an item can be detected by the iBSS. The purpose of verification measurements in international safeguards is to confirm that State declarations for nuclear operations and SNM are correct. The sensitivity of the iBSS to detect anomalies will determine how effective the spectrometer will be for verification measurements.

Application of the iBSS was then presented as a tool for experimentally verifying neutron energy spectra in SOURCES-4C. Using lessons from the MCNP simulations, the iBSS was used to experimentally unfold neutron energy spectra of sources with well-known geometry. Experimental proof-of-concept was demonstrated using three ^{252}Cf sources, which agreed to within 1-σ of the established ^{252}Cf Watt spontaneous fission spectrum. The iBSS was then benchmarked to SOURCES-4C, which has been extensively benchmarked to PuO_2 items, using a high-purity $^{240}PuO_2$ source. The solution spectrum had strong agreement with the SOURCES-4C spectrum, which included the ^{240}Pu spontaneous fission spectrum and ^{17,18}O(α, n) spectrum. However, the iBSS solution spectra for AmLi and AmBe did not agree with the SOURCES-4C spectra, neither of which have been benchmarked to experimental data prior to this study. It is recommended that SOURCES-4C be benchmarked and updated to include these iBSS results. Additional studies should include a robust study using multiple AmBe sources to establish an accepted neutron neutron energy spectrum. An iBSS system should also be designed for measuring the UF_6 (α, n) neutron energy spectrum for various U enrichments. The neutron rate from the UF_6 (α, n) reaction

is critical for confirming ^{235}U enrichment in enrichment facilities.

Appendices

Appendix A Supplementary Data for Chapter 4

Table A.1: Net count rate data for the ^{249}Cf 388 keV gamma-ray and the ^{251}Cf 177 keV gamma-ray

Source	Net Count Rate [cps]	
	^{249}Cf	^{251}Cf
A	0.5263±0.0046	0.3800±0.0078
B	13.43±0.01	5.354±0.014
C	383.5±0.1	51.36±0.03
D	525.5±0.1	64.78±0.02
E	981.7±0.1	769.9±0.1

Table A.2: Net count rate data for ^{252}Cf spontaneous fission products used for estimating source age

Isotope	Net Count Rate [cps]				
	Source A	Source B	Source C	Source D	Source E
^{137}Cs	0.6736±0.0030	3.878±0.0070	16.62±0.01	17.80±0.01	370.1±1.1
^{138}Cs	0.0868±0.0020	0.3453±0.0033	0.1447±0.0021	0.03880±0.00106	0.3535±0.0033
^{136}I	0.1046±0.0025	0.3343±0.0039	0.1393±0.0023	0.04074±0.00288	0.3716±0.0037
^{140}La	0.1110±0.0049	0.4199±0.0074	0.1783±0.0045	0.04627±0.00101	0.4180±0.0069
^{132}I	0.2156±0.0031	0.6151±0.0129	0.2547±0.0082	0.09822±0.00164	0.6908±0.0054

Appendix B Supplementary Data for Chapter 5

Table B.1: LVAWCC inner and outer ring simulated counts for ^{252}Cf Watt spontaneous fission spectrum for 10^6 neutron histories per simulation. Wall thickness refers to the thickness of moderator surrounding each neutron source. Uncertainty was the reported uncertainty from the F4 tally multiplier in MCNP.

Wall Thickness [cm]	Simulated Counts	
	Inner Ring	Outer Ring
0	204462.1±452.2	140855.0±375.3
1	215325.2±464.0	135693.9±368.4
2	217725.7±466.6	125652.1±354.5
3	206913.1±454.9	112027.0±334.7
4	186058.1±431.3	97196.3±311.8
5	159885.3±399.9	82506.5±287.2
6	133886.2±365.9	68198.2±261.1
7	110147.4±331.9	56465.2±237.6
8	88970.0±298.3	46370.6±215.3
9	71765.8±267.9	37372.6±193.3
10	57367.2±239.5	30282.8±174.0
11	45873.8±214.2	24529.8±156.6
12	36583.0±191.3	19993.7±141.4

Table B.2: LVAWCC inner and outer ring simulated counts for AmBe (α, n) spectrum generated in SOURCES-4C for 10^6 neutron histories per simulation. Wall thickness refers to the thickness of moderator surrounding each neutron source. Uncertainty was the reported uncertainty from the F4 tally multiplier in MCNP.

Wall Thickness [cm]	Simulated Counts	
	Inner Ring	Outer Ring
0	140013.1±294.0	112728.7±484.7
1	150880.4±452.6	113733.6±398.1
2	159098.2±461.4	112715.9±394.5
3	161630.4±468.7	108773.9±380.7
4	158106.8±458.5	102161.0±378.0
5	149124.7±447.4	94600.8±359.5
6	137829.6±441.1	86053.5±344.2
7	124506.3±410.9	77228.0±332.1
8	110632.8±398.3	68173.5±306.8
9	96677.5±367.4	59983.6±293.9
10	84482.1±346.4	52356.2±272.3
11	72587.8±319.4	45594.6±255.3
12	62330.0±299.2	39588.0±241.5

Table B.3: LVAWCC inner and outer ring simulated data for AmLi (α, n) spectrum generated in SOURCES-4C for 10^6 neutron histories per simulation. Wall thickness refers to the thickness of moderator surrounding each neutron source. Uncertainty was the reported uncertainty from the F4 tally multiplier in MCNP.

Wall Thickness [cm]	Simulated Counts	
	Inner Ring	Outer Ring
0	262967.9±578.5	134691.1±431.0
1	255718.7±562.6	114514.3±400.8
2	222764.4±534.6	89387.7±348.6
3	176162.2±493.3	66405.2±305.5
4	131092.9±419.5	47537.0±261.5
5	92410.2±360.4	32888.3±217.1
6	64171.5±301.6	22812.0±182.5
7	43451.6±252.0	15521.5±150.6
8	29470.8±209.2	10287.0±122.4
9	19377.0±170.5	7073.3±102.6
10	12960.6±140.0	4860.2±84.6
11	8690.0±114.7	3281.4±69.2

Appendix C Supplementary Data for Chapter 6

Physical HDPE Cylinder Dimensions

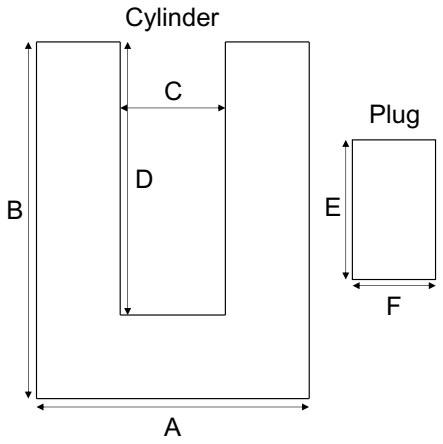

Figure C.1: Cross section of the HDPE cylinders.

Table C.1: HDPE cylinder dimensions for main set of cylinders

HDPE Wall Thickness [cm]	Measurement [mm]					
	A	B	C	D	E	F
0.64	44.35	70.37	32.39	64.27	6.37	31.78
1.27	57.39	82.69	32.54	69.81	12.94	32.34
1.91	76.58	95.61	32.50	76.31	19.26	32.22
2.54	82.58	107.99	32.48	82.90	25.48	31.67
3.18	96.19	120.67	32.46	89.70	31.59	32.19
3.81	107.63	131.53	32.34	95.62	37.34	32.23
4.45	121.54	146.50	32.62	101.77	45.07	32.21
5.08	133.31	158.33	32.44	108.39	50.82	31.86
5.72	146.11	171.37	32.74	114.52	56.95	31.65

Table C.2: HDPE cylinder dimensions for ^{252}Cf insert and additional cylinders

HDPE Wall Thickness [cm]	Measurement [mm]					
	A	B	C	D	E	F
0.64	19.01	25.19	6.53	19.45	6.25	5.95
1.27	31.68	38.26	6.50	25.48	12.56	6.17
1.26 (Insert)	31.80	57.23	6.54	35.29	22.13	6.42

Table C.3: HDPE cylinder dimensions for AmBe insert and additional cylinders

HDPE Wall Thickness [cm]	Measurement [mm]					
	A	B	C	D	E	F
0.64	20.66	22.52	8.03	15.63	6.25	7.85
1.27	33.84	35.15	8.15	22.59	16.58	7.79
1.28 (Insert)	31.75	57.11	8.31	32.99	23.44	7.96

^{252}Cf Supplementary Data

FTC-Cf-1830

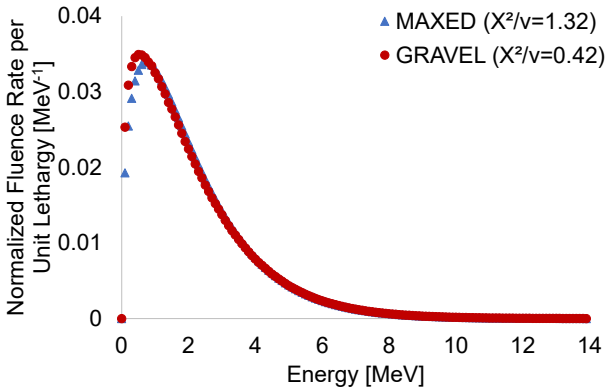

(a) Measurement 1

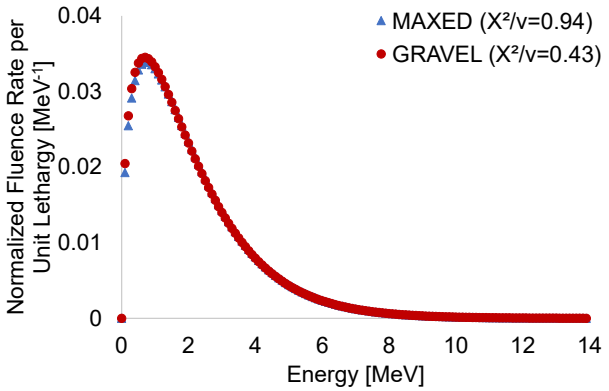

(b) Measurement 2

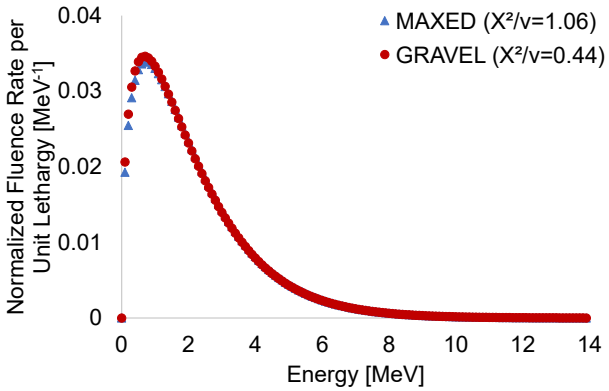

(c) Measurement 3

Figure C.2: MAXED and GRAVEL solution spectra for FTC-Cf-1830

Table C.4: LVAWCC net count rate data [cps] of the inner and outer ring for FTC-Cf-1830

Wall Thickness [cm]	Measurement 1		Measurement 2		Measurement 3	
	Inner Ring	Outer Ring	Inner Ring	Outer Ring	Inner Ring	Outer Ring
0	27361.2±12.5	18446.8±9.3	27360.0±11.6	18440.4±5.3	27340.1±12.8	18435.5±10.4
0.64	28333.3±14.2	18076.±10.6	28315.5±11.8	18051.7±9.6	28325.3±11.9	18064.7±10.7
1.27	28971.0±9.8	17423.2±8.7	28939.0±17.0	17427.3±10.9	28926.5±9.4	17418.2±10.8
1.91	29022.8±12.8	16468.6±8.9	28965.8±11.9	16445.3±9.4	28980.6±11.5	16432.5±9.2
2.54	28048.8±7.2	15253.9±9.4	28028.0±16.7	15259.1±9.1	28016.6±13.5	15245.4±7.9
3.18	25736.2±9.7	13430.3±7.2	25726.2±6.2	13433.8±6.1	25718.1±12.5	13403.2±8.1
3.81	24593.2±12.0	12445.7±7.2	24568.0±15.0	12695.3±9.7	24564.9±15.2	12697.9±8.6
4.45	22193.0±11.1	11319.3±4.3	22209.6±9.0	11318.0±6.2	22177.5±8.2	11290.5±7.4
5.08	19961.3±11.4	10091.0±6.6	19955.1±10.2	10087.1±7.7	19903.4±9.5	10064.6±6.2
5.72	17679.7±7.1	8920.2±5.9	17684.7±13.8	8927.8±7.0	17674.3±11.0	8903.9±5.6
6.35	15713.2±11.0	7921.1±5.2	15676.0±7.9	7901.3±7.0	15665.3±8.0	7898.9±5.7
6.99	13720.6±6.6	6946.6±4.3	13718.2±8.0	6923.8±6.4	13680.3±9.5	6911.4±3.7

FTC-Cf-3010

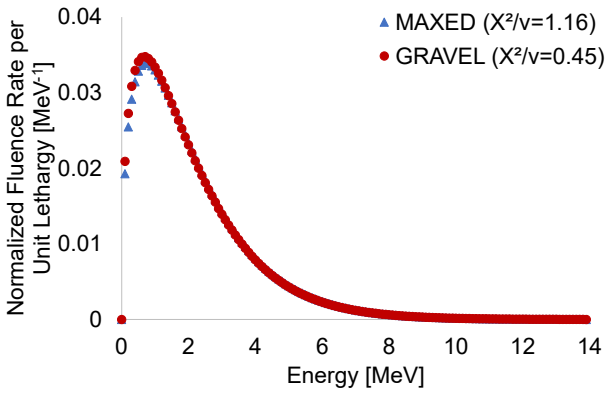

(a) Measurement 1

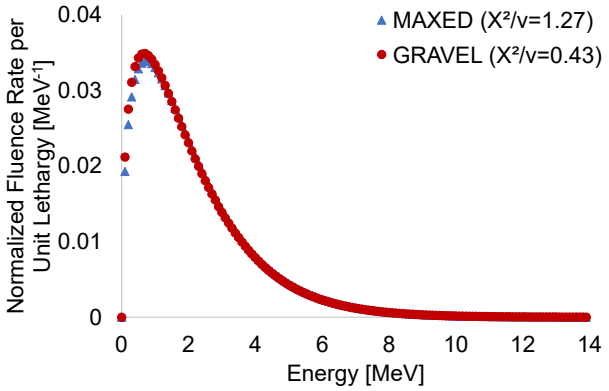

(b) Measurement 2

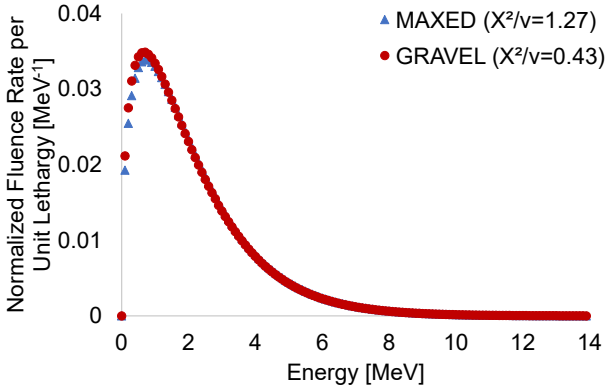

(c) Measurement 3

Figure C.3: MAXED and GRAVEL solution spectra for FTC-Cf-3010

Table C.5: LVAWCC net count rate data [cps] of the inner and outer ring for FTC-Cf-3010

Wall Thickness [cm]	Measurement 1		Measurement 2		Measurement 3	
	Inner Ring	Outer Ring	Inner Ring	Outer Ring	Inner Ring	Outer Ring
0	13559.7±10.2	9112.8±9.1	13568.5±10.2	9111.1±9.4	13558.8±8.0	9101.7±7.1
0.64	14055.1±9.8	8916.5±7.0	14068.3±10.7	8913.7±6.8	14041.5±9.1	8911.4±6.9
1.27	14362.1±2.9	8604.8±4.1	14342.9±11.0	8610.7±3.9	14362.7±10.8	8601.4±6.8
1.91	14371.±7.4	8129.5±5.3	14386.3±6.4	8108.5±4.5	14381.±8.8	8123.1±7.1
2.54	13899.9±7.2	7537.0±9.0	13889.6±5.8	7527.2±4.1	13909.1±7.8	7529.6±4.7
3.18	12756.7±7.6	6624.6±5.9	12748.5±7.2	6634.1±4.2	12749.6±8.0	6610.3±6.6
3.81	12178.1±6.6	6268.0±6.0	12161.2±6.5	6263.8±3.0	12187.2±5.3	6259.8±5.2
4.45	11003.2±6.0	5567.3±4.3	10992.9±5.6	5584.3±5.2	10989.4±4.9	5572.3±4.6
5.08	9874.2±5.8	4957.9±5.6	9875.1±6.8	4971.5±5.7	9877.8±7.2	4970.1±2.7
5.72	8742.3±7.5	4388.3±5.1	8736.0±5.7	4399.3±3.5	8744.1±6.3	4393.0±2.6
6.35	7766.2±5.6	3900.6±3.6	7751.3±4.9	3890.6±2.8	7758.4±8.5	3902.4±2.8
6.99	6766.6±6.1	3413.3±4.2	6768.2±3.0	3409.0±3.6	6768.6±3.7	3407.3±2.8

EZ Q9-304

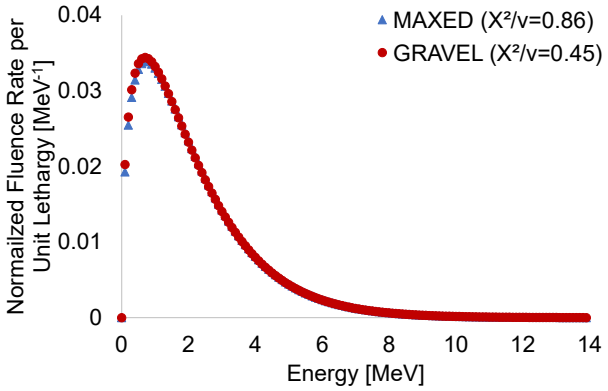

(a) Measurement 1

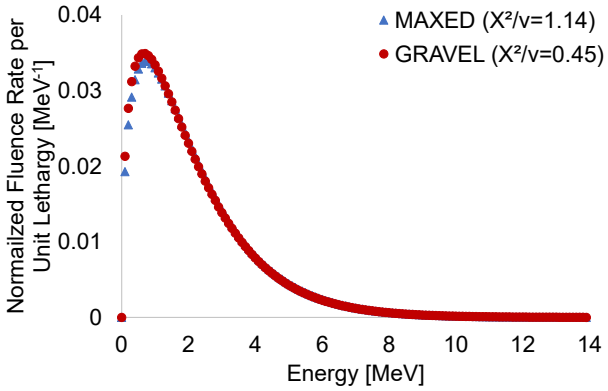

(b) Measurement 2

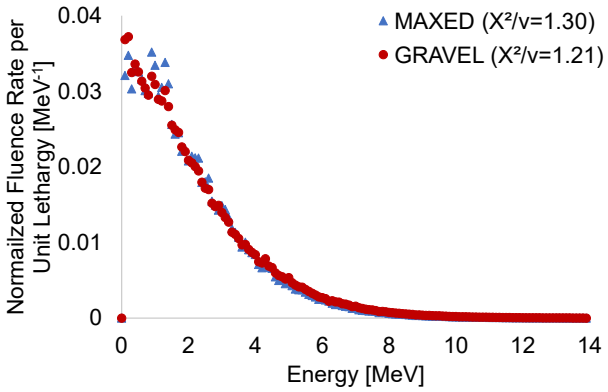

(c) Measurement 3

Figure C.4: MAXED and GRAVEL solution spectra for EZ Q9-304

Table C.6: LVAWCC count rate data [cps] of the inner and outer ring for EZ Q9-304

Wall Thickness [cm]	Measurement 1		Measurement 2		Measurement 3	
	Inner Ring	Outer Ring	Inner Ring	Outer Ring	Inner Ring	Outer Ring
0	31245.7±13.5	21098.3±12.0	31249.7±11.5	21111.6±11.5	31241.8±11.0	21099.3±6.3
0.64	32317.0±10.0	20653.8±11.3	32333.5±14.4	20655.8±13.9	32330.2±15.5	20664.5±6.9
1.27	33053.0±10.7	19924.7±8.6	33044.7±10.3	19921.0±6.7	33049.7±10.5	18843.7±7.6
1.91	33083.3±11.8	18815.7±11.0	33078.7±12.9	18826.0±10.3	33087.6±12.5	18845.5±10.2
2.54	32029.0±16.2	17445.2±6.4	32035.5±19.0	17464.4±5.8	32041.4±9.4	17443.7±8.0
3.18	29412.5±12.4	15350.2±12.4	29399.6±17.6	15361.5±8.6	29412.1±12.8	15359.3±7.1
3.81	28096.5±10.3	14543.±10.4	28080.9±11.8	14539.1±6.9	28051.4±10.7	14533.2±8.0
4.45	25392.4±14.7	12926.9±8.0	25405.0±12.6	12666.3±7.6	25389.0±9.7	12953.3±5.1
5.08	22820.7±10.2	11544.6±7.5	22817.3±17.9	11538.1±9.4	22797.4±14.1	11530.3±5.5
5.72	20223.2±13.0	10196.0±8.6	20243.8±6.7	10204.0±5.9	20233.1±7.3	10199.9±5.8
6.35	17965.0±3.7	9065.7±5.2	17984.1±7.8	9075.2±5.2	17956.1±11.8	9046.9±3.4
6.99	15684.6±8.4	7916.2±3.1	15671.8±6.3	7926.5±4.3	15685.1±10.4	7929.1±5.0

$^{240}PuO_2$ Supplementary Data

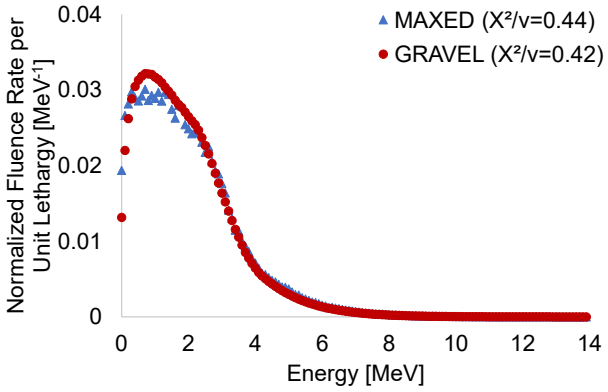

(a) Measurement 1

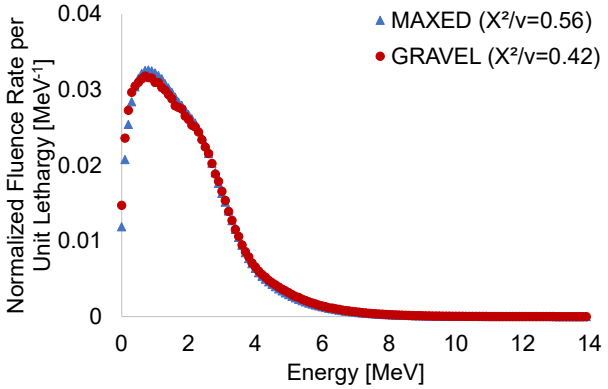

(b) Measurement 2

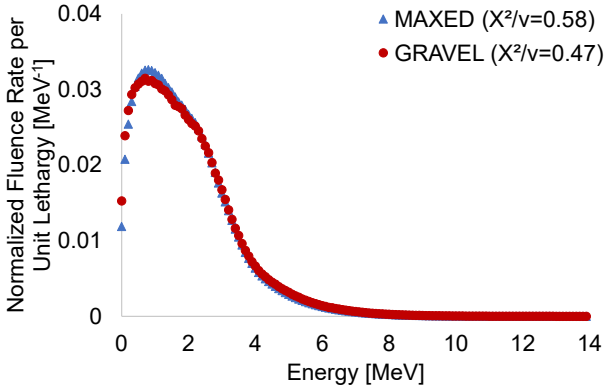

(c) Measurement 3

Figure C.5: MAXED and GRAVEL solution spectra for the high-purity $^{240}PuO_2$ source

Table C.7: LVAWCC count rate data [cps] of the inner and outer ring for $^{240}PuO_2$

Wall Thickness [cm]	Measurement 1		Measurement 2		Measurement 3	
	Inner Ring	Outer Ring	Inner Ring	Outer Ring	Inner Ring	Outer Ring
0	3611.5±2.2	2435.2±2.3	3602.2±2.3	2431.9±1.8	3605.3±2.0	2433.2±1.7
0.64	3723.1±2.3	2365.2±1.6	3721.7±2.7	2364.9±2.0	3722.7±1.8	2363.3±1.9
1.27	3764.4±2.2	2246.9±1.7	3760.0±2.2	2244.3±2.0	3757.9±2.2	2243.9±2.1
1.91	3626.6±2.7	2030.6±1.5	3627.2±2.2	2025.9±1.8	3624.8±2.1	2028.1±1.2
2.54	3524.8±2.2	1936.3±1.5	3524.1±1.8	1934.3±1.2	3527.4±2.2	1931.3±1.4
3.18	3277.1±2.1	1750.0±1.2	3269.8±2.1	1743.4±1.5	3266.4±2.5	1739.0±1.3
3.81	3003.8±1.6	1568.9±1.7	2996.1±2.3	1542.8±1.2	3000.7±2.2	1569.5±1.0
4.45	2702.1±2.0	1393.3±1.3	2698.1±2.2	1392.7±1.1	2697.9±1.9	1392.9±1.2
5.08	2423.2±1.4	1241.4±1.2	2423.2±1.8	1242.7±1.1	2424.5±1.5	1240.4±1.1
5.72	2137.2±1.7	1092.4±1.5	2134.3±1.8	1087.6±1.2	2133.9±1.8	1087.5±1.1

AmLi Supplementary Data

AN-HP-C268

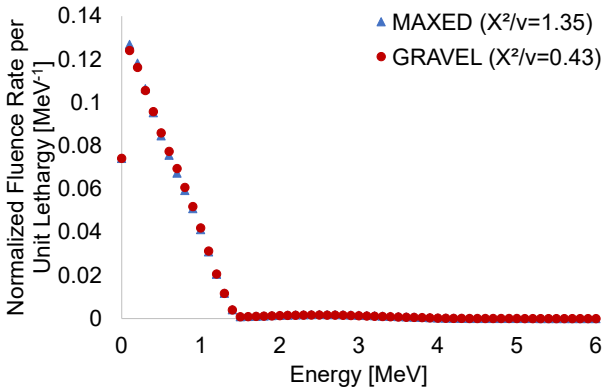

(a) Measurement 1

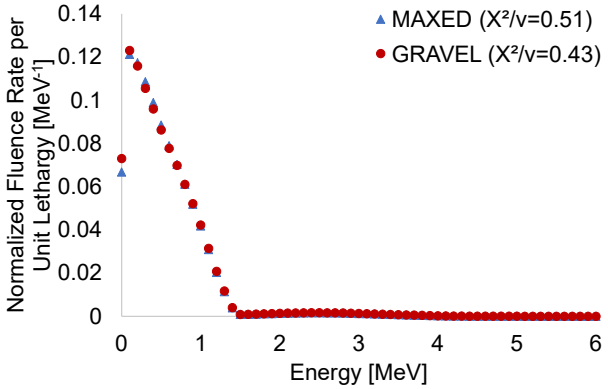

(b) Measurement 2

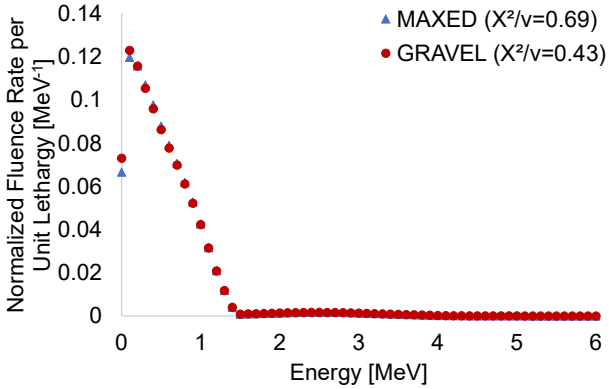

(c) Measurement 3

Figure C.6: MAXED and GRAVEL solution spectra for AN-HP-C268

Table C.8: LVAWCC count rate data [cps] of the inner and outer ring for AmLi-C268

Wall Thickness [cm]	Measurement 1		Measurement 2		Measurement 3	
	Inner Ring	Outer Ring	Inner Ring	Outer Ring	Inner Ring	Outer Ring
0	9244.2±43.0	4553.5±30.4	9238.7±43.0	4565.4±30.4	9240.4±43.0	4562.2±30.4
0.64	9217.2±43.0	4158.3±28.9	9211.9±42.9	4161.8±28.9	9212.6±42.9	4159.0±28.9
1.27	8716.4±41.8	3622.4±27.0	8712.8±41.8	3617.4±27.0	8722.7±41.8	3628.4±27.0
1.91	7486.7±38.7	2855.1±24.0	7491.3±38.7	2845.2±24.0	7472.3±38.7	2843.3±23.9
2.54	6892.7±37.2	2564.9±22.8	6890.8±37.1	2566.6±22.8	6893.1±37.2	2568.1±22.8
3.18	5731.9±33.9	2064.3±20.4	5733.6±33.9	2059.9±20.4	5726.7±33.9	2061.8±20.4
3.81	4710.2±30.7	1657.5±18.3	4707.1±30.7	1655.5±18.3	4711.8±30.7	1660.3±18.4
4.45	3786.7±27.6	1316.2±16.4	3781.7±27.5	1315.4±16.4	3774.8±27.5	1318.9±16.4
5.08	3036.0±24.7	1057.1±14.7	3036.2±24.7	1055.3±14.7	3033.9±24.7	1056.2±14.7
5.72	2362.0±21.8	827.4±13.1	2365.9±21.8	825.2±13.0	2366.7±21.8	823.6±13.0

AN-HP-C272

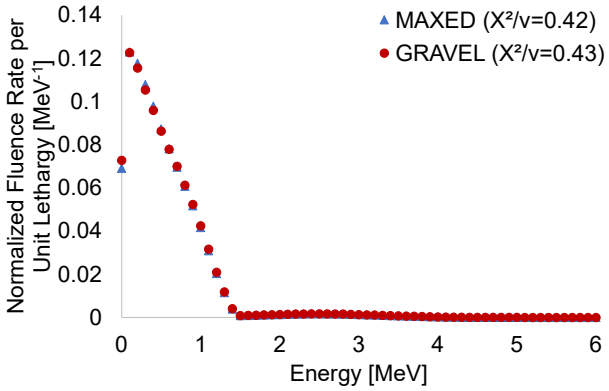

(a) Measurement 1

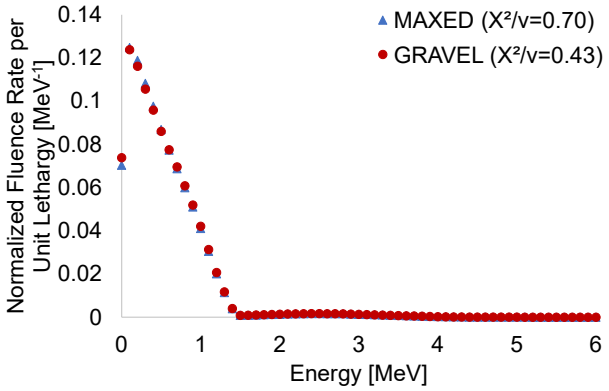

(b) Measurement 2

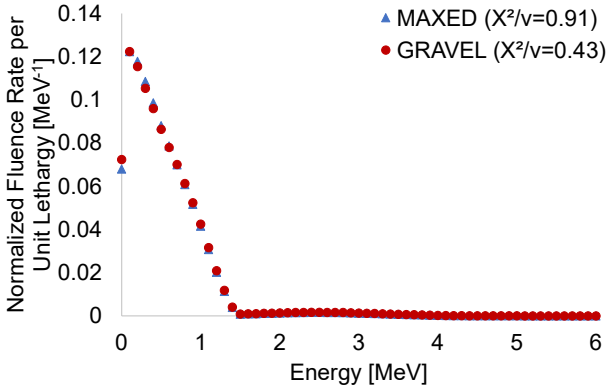

(c) Measurement 3

Figure C.7: MAXED and GRAVEL solution spectra for AN-HP-C272

Table C.9: LVAWCC count rate data [cps] of the inner and outer ring for AmLi-C272

Wall Thickness [cm]	Measurement 1		Measurement 2		Measurement 3	
	Inner Ring	Outer Ring	Inner Ring	Outer Ring	Inner Ring	Outer Ring
0	9301.2±43.2	4592.3±30.5	9296.2±43.2	4592.0±30.5	9297.5±43.2	4590.5±30.5
0.64	9265.6±43.1	4194.9±29.0	9269.1±43.1	4191.7±29.0	9268.6±43.1	4187.5±29.0
1.27	8771.6±41.9	3648.7±27.1	8784.5±41.9	3646.5±27.1	8775.4±41.9	3653.4±27.1
1.91	7526.8±38.8	2866.9±24.0	7536.0±38.8	2869.7±24.1	7523.7±38.8	2872.8±24.1
2.54	6944.5±37.3	2588.4±22.9	6938.0±37.3	2581.5±22.8	6943.2±37.3	2588.0±22.9
3.18	5760.4±34.0	2072.8±20.5	5779.1±34.0	2076.2±20.5	5775.4±34.0	2084.0±20.5
3.81	4743.9±30.8	1675.2±18.4	4743.0±30.8	1670.2±18.4	4748.0±0.8	1675.3±18.4
4.45	3801.5±27.6	1329.1±16.4	3805.4±27.6	1330.0±16.5	3804.5±27.6	1326.5±16.4
5.08	3056.9±24.8	1063.3±14.7	3059.5±24.8	1064.8±14.8	3055.4±24.8	1064.2±14.8
5.72	2388.5±21.9	833.5±13.1	2377.6±21.8	832.2±13.1	2380.0±21.9	830.8±13.1

AN-HP-N458

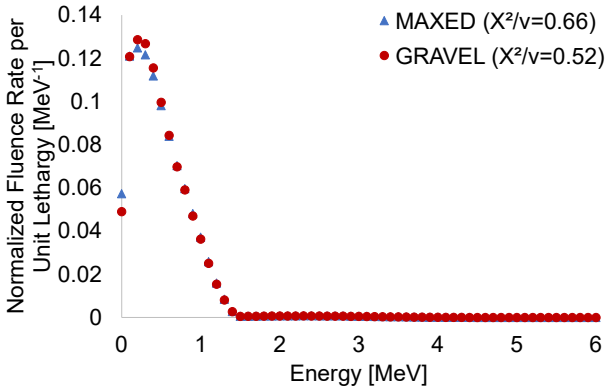

(a) Measurement 1

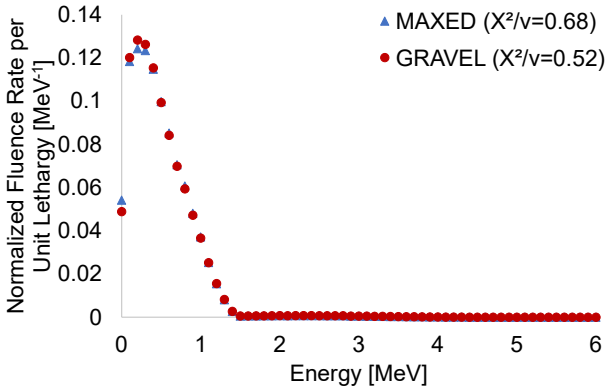

(b) Measurement 2

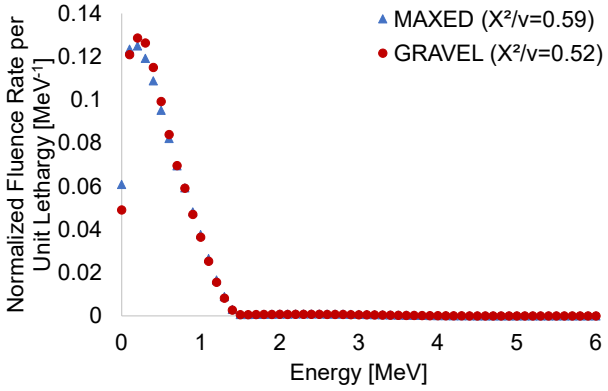

(c) Measurement 3

Figure C.8: MAXED and GRAVEL solution spectra for AN-HP-N458

Table C.10: LVAWCC count rate data [cps] of the inner and outer ring for AmLi-N458

Wall Thickness [cm]	Measurement 1		Measurement 2		Measurement 3	
	Inner Ring	Outer Ring	Inner Ring	Outer Ring	Inner Ring	Outer Ring
0	12978.1±1.0	6423.9±35.9	12969.0±50.9	6428.2±35.9	12957.5±50.9	6422.4±35.9
0.64	12956.4±50.9	5829.7±34.2	12943.0±50.9	5843.1±34.2	12951.3±50.9	5841.7±34.2
1.27	12289.6±49.6	5076.5±31.9	12285.0±49.6	5071.5±31.9	12289.4±49.6	5071.9±31.9
1.91	10569.3±46.0	3978.4±28.2	10574.1±46.0	3977.6±28.2	10566.3±46.0	3975.5±28.2
2.54	9734.6±44.1	3575.8±26.8	9746.8±44.2	3574.9±26.8	9737.3±44.1	3568.3±26.7
3.18	8099.1±40.3	2842.6±23.9	8097.1±40.2	2845.5±23.9	8098.9±40.3	2843.0±23.9
3.81	6651.3±36.5	2264.8±21.3	6651.4±36.5	2276.9±21.4	6653.7±36.5	2265.1±21.3
4.45	5312.4±32.6	1774.9±18.9	5310.1±32.6	1779.1±18.9	5310.2±32.6	1782.4±18.9
5.08	4252.0±29.2	1402.8±16.8	4253.3±29.2	1410.4±16.8	4245.8±29.2	1405.5±16.8
5.72	3284.2±25.6	1076.4±14.7	3282.8±25.6	1075.9±14.7	3288.4±25.7	1078.9±14.7

AN-HP-N459

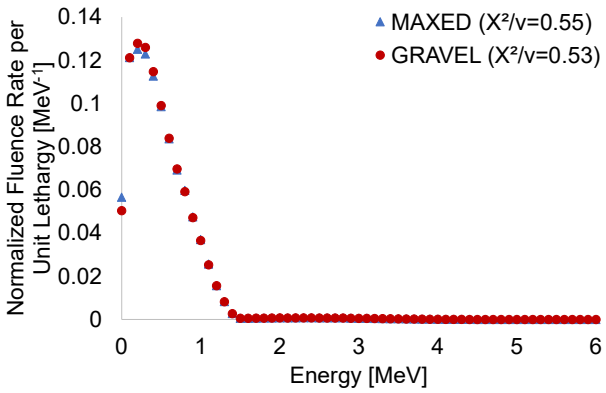

(a) Measurement 1

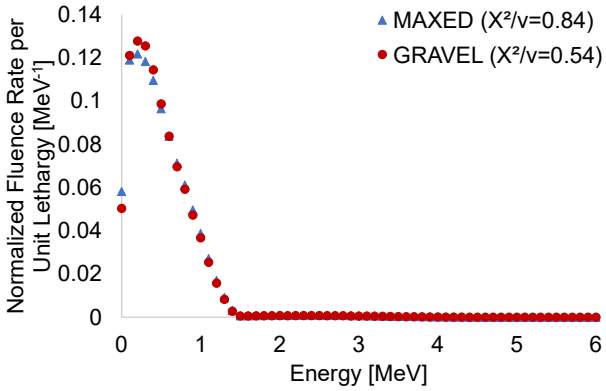

(b) Measurement 2

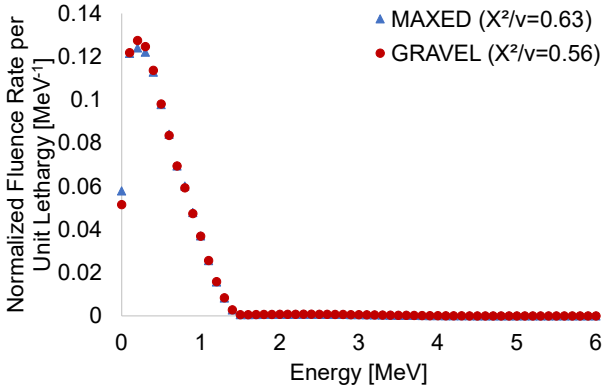

(c) Measurement 3

Figure C.9: MAXED and GRAVEL solution spectra for AN-HP-N459

Table C.11: LVAWCC count rate data [cps] of the inner and outer ring for AmLi-N459

Wall Thickness [cm]	Measurement 1		Measurement 2		Measurement 3	
	Inner Ring	Outer Ring	Inner Ring	Outer Ring	Inner Ring	Outer Ring
0	13273.3±51.5	6558.3±36.2	13265.0±51.5	6566.2±36.3	13270.2±51.5	6558.0±36.2
0.64	13226.9±51.4	5957.3±34.5	13234.0±51.5	5961.7±34.5	13243.0±51.5	5967.5±34.6
1.27	12550.9±50.1	5183.3±32.2	12557.7±50.1	5184.2±32.2	12555.8±50.1	5192.3±32.2
1.91	10791.2±46.5	4057.8±28.5	10798.4±46.5	4059.6±28.5	10804.3±46.5	4071.4±28.6
2.54	9947.2±44.6	3647.4±27.0	9943.3±44.6	3652.6±27.0	9940.7±44.6	3643.7±27.0
3.18	8271.5±40.7	2911.0±24.1	8275.±40.7	2909.5±24.1	8273.2±40.7	2906.9±24.1
3.81	6794.6±36.9	2314.5±21.5	6798.0±36.9	2322.7±21.6	6796.0±36.9	2324.3±21.6
4.45	5425.9±33.0	1817.1±19.1	5430.7±33.0	1816.7±19.1	5432.7±33.0	1819.0±19.1
5.08	4342.2±29.5	1437.2±17.0	4348.9±29.5	1435.7±17.0	4347.5±29.5	1442.1±17.0
5.72	3359.7±25.9	1099.1±14.9	3358.7±25.9	1104.4±14.9	3359.6±25.9	1104.±14.9

AmBe Supplementary Data

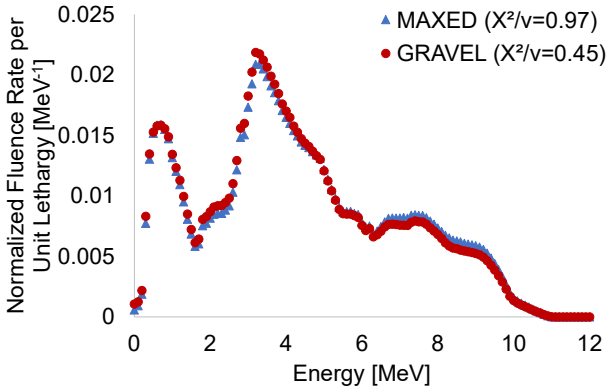

(a) Measurement 1

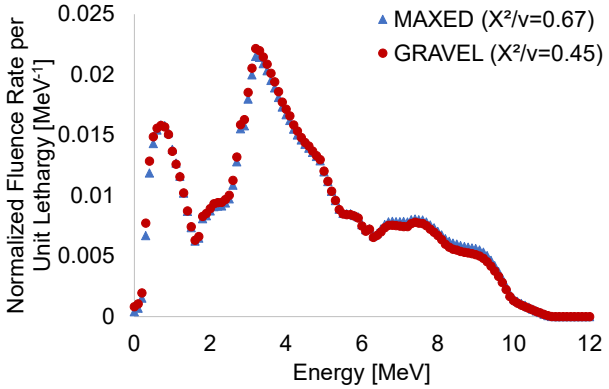

(b) Measurement 2

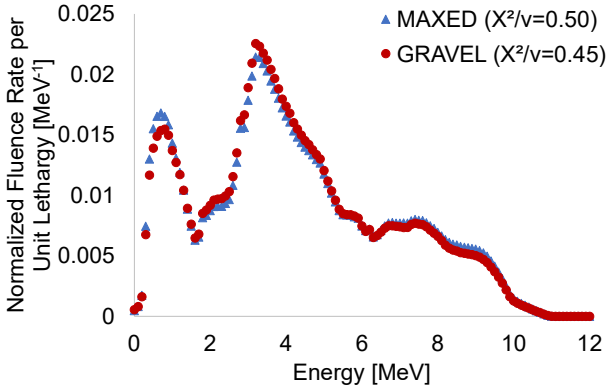

(c) Measurement 3

Figure C.10: MAXED and GRAVEL solution spectra for K560/18

Table C.12: LVAWCC count rate data [cps] of the inner and outer ring for K560/18

Wall Thickness [cm]	Measurement 1		Measurement 2		Measurement 3	
	Inner Ring	Outer Ring	Inner Ring	Outer Ring	Inner Ring	Outer Ring
0	1303.0±16.2	977.5±14.1	1300.2±16.2	978.9±14.1	1299.5±16.2	979.1±14.1
0.64	1351.6±16.5	979.2±14.1	1352.9±16.5	978.2±14.1	1350.4±16.5	980.0±14.1
1.27	1399.1±16.8	967.9±14.0	1400.6±16.8	970.3±14.0	1396.6±16.8	971.4±14.0
1.91	1431.6±17.0	957.7±13.9	1428.9±16.9	961.8±13.9	1429.2±16.9	957.9±13.9
2.54	1424.7±16.9	927.1±13.7	1426.2±16.9	924.8±13.7	1425.9±16.9	928.2±13.7
3.18	1383.7±16.7	870.9±13.3	1382.7±16.7	870.7±13.3	1382.9±16.7	870.0±13.3
3.81	1355.7±16.5	847.9±13.1	1354.9±16.5	847.9±13.1	1355.1±16.5	845.7±13.1
4.45	1289.5±16.1	798.5±12.7	1287.9±16.1	795.9±12.7	1291.2±16.1	795.8±12.7
5.08	1217.7±15.6	749.2±12.3	1222.7±15.7	746.0±12.3	1219.6±15.7	748.0±12.3
5.72	1142.5±15.2	698.8±11.9	1144.3±15.2	697.0±11.9	1141.7±15.2	699.2±11.9
6.35	1071.6±14.7	652.5±11.5	1069.1±14.7	654.6±11.5	1069.6±14.7	649.2±11.5
6.99	988.2±14.1	601.1±11.1	989.6±14.1	601.6±11.1	986.9±14.1	602.2±11.1

Appendix D Technical Data Sheets for Neutron Sources

Technical data sheets were included for ^{252}Cf sources FTC-Cf-1830, FTC-Cf-3010, and EZ Q9-304 and AmLi sources AN-HP-N458 and AN-HP-N459. The technical data sheets are presented in the order that they were listed. Note that the batch information from the Radiochemical Engineering Development Center for the FTC sources was included, as that is what was provided with the source. FTC-Cf-1830 was reported to be associated with batch SR-Cf-1349 and FTC-Cf-3010 was reported to be associated with SR-Cf-1371.

INFORMATION SHEET

^{252}Cf NEUTRON SOURCE
SPECIAL FORM RADIOACTIVE MATERIALS
CERTIFICATE NO. USA/0065/S, Rev. 7

Source Identification Number: SR-Cf-1349

Shipped To: Frontier Technology Corp., 1641 Burnett Drive, Xenia, OH 45385

Shipping Capsule Dwg. No.: M-12541-CP-099 E-1, Items 1a, 1b, 1c, and 1d

Closure Date: 2/11/2002

Decontamination and Closure Tests

Method: After closure, capsule surfaces were decontaminated until all exterior surfaces were free of contamination (≤9 d/m alpha and <100 d/m beta-gamma) as determined by a wipe test. The assembly was immersed in a helium atmosphere at a pressure of 300 pounds per square inch for a period of 30 minutes, then transferred to a helium leak detector. The leak detector has a minimum sensitivity of 1.0×10^{-8} standard cubic centimeters of helium per second.

Tests: The finished capsule was found free of detectable leakage and free of transferrable contamination on 2/11/2002.

Californium Content

Isotopic Composition: The californium stock material used to prepare the Pd-Cf_2O_3 composite wires in the special form shipping capsule SR-Cf-1349 is identified by Batch Code CXCF-669. The isotopic mass distribution of this lot of material is listed in Table 1. The date for the last separation of ^{248}Cm decay product from this material was 4/3/2001.

Wire Form: The californium, in the form of Pd-Cf_2O_3 composite, has been heated to 1600°C for 60 minutes to melt the palladium and homogenize the mixture. The resulting melted pellets were rolled to wires having nearly oval cross-sections. The resulting wires, Pd-Cf-164 and Pd-Cf-166, were measured to be ≤0.050 inches and ≤0.054, respectively, across the long width of the oval.

Source Strength: The neutron emission rate of the finished assembly SR-Cf-1349 was determined by comparing its strength to that of NSD-119, a reference ^{252}Cf source traceable to the national reference radium-beryllium source, NS-1, at the National Institute of Standards and Technology. The comparison was made by inserting the capsule assembly into a moderator containing an array of fission counters and measuring the subsequent induced electric current by a picoammeter. The total neutron emission rate of this assembly was found to be 1.0419×10^{10} neutrons per second with a relative standard error of ±0.60 % as of 2/11/2002.

Cf-252 Content: The ^{252}Cf content of this assembly has been inferred from the measured neutron emission rate by correcting the gross emission rate by a factor of 0.99796, the fraction of the spontaneous fission neutrons emanating from the isotope ^{252}Cf, and by dividing by 2.31434×10^6 neutrons per second per microgram. These values may be calculated from the isotopic compositions listed in Table 1, the relative quantities listed in the accompanying letter, and from the nuclear data listed in Table 2. The

equivalent ^{252}Cf content on the assay date, 2/11/2002, was computed to be 4,492.5 µg with a relative standard error of ±0.60 %. Due to propagation of errors along the chain of traceability and also to non-random errors, including variations in source geometry, the overall accuracy of the assay is estimated to be ±3% limit of error.

The radiation intensity one meter from a ^{252}Cf source in air at standard atmospheric conditions and without contributions from scattering media is nominally 2210 mrem/h fast neutrons plus 190 mR/h gamma for each milligram of ^{252}Cf in the capsule.

Table 1. Isotopic Mass Analyses

Cf Batch Code	CXCF-669
Mass Analysis Date	3/8/01
Nuclide	Isotopic Composition (atom %)
^{249}Cf	1.87
^{250}Cf	9.10
^{251}Cf	2.78
^{252}Cf	86.13
^{253}Cf	0.0005
^{254}Cf	0.008

Table 2. Assumed Nuclear Parameters

Nuclide	Half-Life	Alpha branching ratio	Spont. fission branching ratio	ν
^{249}Cf	351 y	~1.0	5.2×10^{-9}	3.4
^{250}Cf	13.20 y	0.99921	0.00079	3.53
^{251}Cf	898 y	~1.0	9.0×10^{-6}	3.7
^{252}Cf	2.645 y	0.96904	0.03096	3.768
^{253}Cf	17.81 d	0.0031		
^{254}Cf	61.9 d	0.00299	0.99701	3.93

Attested J.B. Knauer Date 2/12/2002

INFORMATION SHEET

^{252}Cf NEUTRON SOURCE
SPECIAL FORM RADIOACTIVE MATERIALS
CERTIFICATE NO. USA/0065/S, Rev. 8

Source Identification Number: SR-Cf-1371

Shipped To: Frontier Technology Corp., 1641 Burnett Drive, Xenia, OH 45385

Shipping Capsule Dwg. No.: M-12541-CP-099 E-1, Items 1a, 1b, 1c, and 1d

Closure Date: 09/26/06

Decontamination and Closure Tests

Method: After closure, capsule surfaces were decontaminated until all exterior surfaces were free of contamination (< 20 d/m alpha and < 200 d/m beta-gamma) as determined by a wipe test. The assembly was immersed in a helium atmosphere at a pressure of 300 pounds per square inch for a period of 30 minutes, and then was transferred to a helium leak detector. The leak detector has a minimum sensitivity of 1.0×10^{-8} standard cubic centimeters of helium per second.

Tests: The finished capsule was found free of detectable leaks and free of transferable contamination on 09/26/2006.

Californium Content

Isotopic Composition: The californium used to prepare the Pd-Cf_2O_3 composite wires in the special form shipping capsule SR-Cf-1371 is identified by Batch Code CXCF-708. The isotopic mass distribution of this lot of material is listed in Table 1. The ^{248}Cm decay product was last separated on 05/17/2005.

Wire Form: The californium, in the form of Pd-Cf_2O_3 composite, has been heated to 1600°C for 60 minutes to melt the palladium and homogenize the mixture. The resulting melted pellets and wires were rolled having a nearly oval cross-section. The width across the long side of the wire cross-sections was measured to be <0.054-in. for each wire.

Source Strength: The neutron emission rate of the finished assembly SR-Cf-1371 was determined by comparing its strength to that of SR-Cf-3022, a reference ^{252}Cf source traceable to the national reference radium-beryllium source, NS-1, at the National Institute of Standards and Technology. The comparison was made by inserting the capsule assembly into a moderator containing an array of fission counters and measuring the subsequent induced electric current by a picoammeter. The total neutron emission rate of this assembly was found to be 1.1193×10^{10} neutrons per second with a relative standard error of ±0.67 % as of 09/26/2006.

Cf-252 Content: The ^{252}Cf content of this assembly has been inferred from the measured neutron emission rate by correcting the gross emission rate by a factor of 0.99902, the fraction of the spontaneous fission neutrons emanating from the isotope ^{252}Cf, and by dividing by 2.31434×10^6 neutrons per second per microgram. These values may be calculated from the isotopic composition listed in Table 3 the relative quantities listed in the accompanying letter, and from the nuclear data listed in Table 4. The equivalent ^{252}Cf content on the assay date, 09/26/2006, was computed to be 4.832 µg with a relative standard error of ±0.67 %. Due to propagation of errors along the chain of traceability and also to non-random errors, including variations in source geometry, the overall accuracy of the assay is estimated to be ±3% limit of error.

The radiation intensity one meter from a ^{252}Cf source in air at standard atmospheric conditions and without contributions from scattering media is nominally 2210 mrem/h fast neutrons plus 190 mR/h gamma for each milligram of ^{252}Cf in the capsule.

Table 1. Isotopic Mass Analyses

Cf Batch Code	CXCF-708
Mass Analysis Date	06/09/2003

Nuclide	Isotopic Composition (wt %)
^{249}Cf	3.411
^{250}Cf	8.702
^{251}Cf	2.600
^{252}Cf	85.273
^{253}Cf	0.004
^{254}Cf	0.010

Table 2. Assumed Nuclear Parameters

Nuclide	Half-Life	Alpha branching ratio	Spont. fission branching ratio	ν
^{249}Cf	351 y	~1.0	5.2×10^{-9}	3.4
^{250}Cf	13.20 y	0.99921	0.00079	3.53
^{251}Cf	898 y	~1.0	9.0×10^{-6}	3.7
^{252}Cf	2.645 y	0.96904	0.03096	3.768
^{253}Cf	17.81 d	0.0031		
^{254}Cf	61.9 d	0.00299	0.99701	3.93

Attested _____ Date 9/26/2006

Eckert & Ziegler
Isotope Products

24937 Avenue Tibbitts
Valencia, California 91355

Tel 661·309·1010
Fax 661·257·8303

NOMINAL SOURCE CERTIFICATE

Customer: UT-Battelle LLC
Purchase Order No.: 4000165595
Model No.: HEG-252
Catalog No.: CF230230050U
Capsule Type: A3023
Active Diameter: 0.125" (3.18 mm)
Cover: Stainless Steel
Backing: Stainless Steel

Certificate Date: 2018-10-23
Quantity: 1
SS&DR No.: CA0406S122S
ISO/ANSI Classification: ANSI 77C63333
Special Form No.: USA/0356/S-96 Rev 13
Nuclide Half Life: 2.645 ± 0.008 years
Recommended Working Life: 15 years

Nuclide	Source No.	Activity	Radiation Output	Reference Date
Cf-252	Q9-304	1850 kBq (50 µCi)	Not Applicable	2018-11-01

Impurities: See Technical Data Sheet

Leak Test Information is on Reverse Side:

Remarks:
- This document uses the numerical convention where 1.000 = 1 and 1,000 = 10^3.
- This document uses the date convention YYYY-MM-DD in accordance with ISO 8601.
- Nuclear data were taken from "Table of Radioactive Isotopes", edited by Virginia Shirley, 1986.
- ANSI classification is equivalent to ISO2919.

Matt Dey — 2018-10-23
Name — **Signature** — **Date**

Notebook Page: 2020-39

Eckert & Ziegler
Isotope Products

24937 Avenue Tibbitts
Valencia, California 91355

Tel 661·309·1010
Fax 661·257·8303

www.ezag.com

Cf-252 Technical Data

The Cf-252 used to prepare your order of source Q9-304 was taken from Eckert & Ziegler Isotope Products Laboratories Lot #6023006. It had the following composition as of 2018-08-01.

Nuclide	Mass %	Activity %	
Cf-249	8.268	0.0823	.4115 μCi
Cf-250	13.237	3.504	1.752 μCi
Cf-251	4.489	0.0173	.00865 μCi
Cf-252	74.006	96.396	48.198 μCi

The Cm-248 decay product was last separated on 2017-09-16.

Isotopic composition provided by Oak Ridge National Laboratory

If you have any questions, please contact Eckert & Ziegler Isotope Products Technical Service: 661-309-1010

Res Nino Lazatin, Chemist — 2018-10-23

name, title **signature** **date**

IPL Form055-2 Rev. A

GAMMATRON INC.

P.O. BOX 34042 • HOUSTON, TEXAS 77034 • AREA CODE 713/641-0391

SEALED SOURCE CERTIFICATE

1. PURCHASER CANBERRA INDUSTRIES P.O.# 68561
2. MANUFACTURER GAMMATRON, INC.
3. MODEL AN-HP SERIAL # N-458
4. ACTIVE MATERIAL Am-241Li

   MAXIMUM CONTENT 1.25 Ci

   MINIMUM CONTENT 1.15 Ci

   ACTUAL CONTENT BASED ON WEIGHT INPUT AND CI/GRAM AS SUPPLIED BY ORNL ± 1% 1.20 Ci

   YIELD:

   STD N/A

   GAMMATRON STD 3.2 X 10E+4 NPS

   SERIAL # N-458=5.5 X 10E+4 NPS +/-10%
5. THIS IS TO CERTIFY THAT THIS SOURCE MEETS THE REQUIREMENTS FOR SPECIAL FORM AS DEFINED IN DOT TITLE 49 (173.403[Z]) AND THE REQUIREMENTS OF:

   ANSI CLASSIFICATION 77C44434 SIGNATURE

   TEXAS REGULATIONS PART 36.108 N/A SIGNATURE
6. MATERIAL OF CONSTRUCTION 17-4SS
7. WIPE TEST:

   INNER CAPSULE <0.005 uCi

   OUTER CAPSULE <.0001 uCi DATE 04/16/98

   BY
8. HELIUM TEST NEG INNER NEG. OUTER
9. PRESSURE TEST N/A WT. FINAL OUT
10. CONTAINER WIPE TEST <0.0001 uCi
11. TYPE 7A SERIAL # NON RETURNABLE
12. SURFACE 2mRem/HR INDEX 0.1 LABEL YELLOW II

GAMMATRON INC.

P.O. BOX 34042 • HOUSTON, TEXAS 77034 • AREA CODE 713/641-0391

SEALED SOURCE CERTIFICATE

1. PURCHASER CANBERRA INDUSTRIES P.O.# 68561
2. MANUFACTURER GAMMATRON, INC.
3. MODEL AN-HP SERIAL # N-459
4. ACTIVE MATERIAL Am-241Li

   MAXIMUM CONTENT 1.25 Ci

   MINIMUM CONTENT 1.15 Ci

   ACTUAL CONTENT BASED ON WEIGHT INPUT AND CI/GRAM AS SUPPLIED BY ORNL ± 1% 1.20 Ci

   YIELD:

   STD N/A

   GAMMATRON STD 3.2 X 10E+4 NPS

   SERIAL # N-459=5.5 X 10E+4 NPS +/-10%
5. THIS IS TO CERTIFY THAT THIS SOURCE MEETS THE REQUIREMENTS FOR SPECIAL FORM AS DEFINED IN DOT TITLE 49 (173.403[Z]) AND THE REQUIREMENTS OF:

   ANSI CLASSIFICATION 77C44434 SIGNATURE

   TEXAS REGULATIONS PART 36.108 N/A SIGNATURE
6. MATERIAL OF CONSTRUCTION 17-4SS
7. WIPE TEST:

   INNER CAPSULE <0.005 uCi

   OUTER CAPSULE <.0001 uCi DATE 04/16/98

   BY
8. HELIUM TEST NEG INNER NEG. OUTER
9. PRESSURE TEST N/A WT. FINAL OUT
10. CONTAINER WIPE TEST <0.0001 uCi
11. TYPE 7A SERIAL # NON RETURNABLE
12. SURFACE 2mRem/HR INDEX 0.1 LABEL YELLOW II

References

[1] M. Chadwick, M. Herman, P. Obložinský, M. Dunn, Y. Danon, A. Kahler, D. Smith, B. Pritychenko, G. Arbanas, R. Arcilla, R. Brewer, D. Brown, R. Capote, A. Carlson, Y. Cho, H. Derrien, K. Guber, G. Hale, S. Hoblit, S. Holloway, T. Johnson, T. Kawano, B. Kiedrowski, H. Kim, S. Kunieda, N. Larson, L. Leal, J. Lestone, R. Little, E. McCutchan, R. MacFarlane, M. MacInnes, C. Mattoon, R. McKnight, S. Mughabghab, G. Nobre, G. Palmiotti, A. Palumbo, M. Pigni, V. Pronyaev, R. Sayer, A. Sonzogni, N. Summers, P. Talou, I. Thompson, A. Trkov, R. Vogt, S. van der Marck, A. Wallner, M. White, D. Wiarda, P. Young, ENDF/B-VII.1 Nuclear Data for Science and Technology: Cross Sections, Covariances, Fission Product Yields and Decay Data, Nuclear Data Sheets 112 (2011) 2887–2996. doi:10.1016/j.nds.2011.11.002.

[2] K. Geiger, L. Van der Zwan, The neutron spectra and the resulting fluence-kerma conversions for ^{241}Am-Li(α, n) and ^{210}Po-Li(α, n) sources, Health Physics 21 (1) (1971) 120–123.

[3] H. Tagziria, N. Roberts, D. Thomas, Measurement of the ^{241}Am–Li radionuclide neutron source spectrum, Nuclear Instruments and Methods in Physics Research Section A: Accelerators, Spectrometers, Detectors and Associated Equipment 510 (3) (2003) 346–356. doi:10.1016/S0168-9002(03)01825-4.

[4] J. W. Marsh, D. J. Thomas, M. Burke, High resolution measurements of neutron energy spectrom from Am-Be and Am-B neutron sources, Nuclear Instruments and Methods in Physics Research Section A: Accelerators, Spectrometers, Detectors and Associated Equipment 366 (1995) 340–348.

[5] Treaty on the Non-Proliferation of Nuclear Weapons (5 March 1970).

[6] International Atomic Energy Agency, Model Protocol Additional to the Agreements Between States and the International Atomic Energy Agency for the Application of Safeguards (1997).

[7] International Atomic Energy Agency, Safeguards Techniques and Equipment: 2011 Edition, International Verification Series No. 1 (Rev. 2), Tech. Rep.

IAEA/NVS/1/2011, International Atomic Energy Agency, Vienna, Austria (2011).

[8] E. F. Shores, SOURCES 4C: A Code for Calculating (α, n), Spontaneous Fission, and Delayed Neutron Sources and Spectra, Tech. Rep. LA-UR-02-1839, Los Alamos National Laboratory, Los Alamos, New Mexico (2002).

[9] W. B. Wilson, R. T. Perry, W. S. Charlton, T. A. Parish, SOURCES: A code for calculation (α, n), spontaneous fission, and delayed neutron sources and spectra, Progress in Nuclear Energy 51 (2009) 608–613. doi:10.1016/j.pnucene.2008.11.007.

[10] H. Tagziria, B. Wiegel, H. Klein, K. Knauf, J. Wittstock, A. Zimbal, Measurement and Monte Carlo modelling of the JRC ^{241}Am-Li(α,n) source spectrum, Radiation Protection Dosimetry 110 (1-4) (2004) 129–134. doi:10.1093/rpd/nch189.

[11] R. Weinmann-Smith, D. Beddingfield, A. Enqvist, M. T. Swinhoe, Variations in AmLi source spectra and their estimation utilizing the 5 Ring Multiplicity Counter, Nuclear Instruments and Methods in Physics Research Section A: Accelerators, Spectrometers, Detectors and Associated Equipment 856 (2017) 17–25. doi:10.1016/j.nima.2017.02.083.

[12] H. Tagziria, M. Looman, The ideal neutron energy spectrum of ^{241}AmLi(α, n)^{10}B sources, Applied Radiation and Isotopes 70 (10) (2012) 2395–2402. doi:10.1016/j.apradiso.2012.07.008.

[13] A. Favalli, D. P. Broughton, S. Croft, M. S. Grund, R. D. McElroy, G. Renha, Strengthening Technical Safeguards of Fresh Fuel Through International Cooperation, Tech. Rep. LA-UR-19-31408, Los Alamos National Laboratory (2019).

[14] R. L. Bramblett, R. I. Ewing, T. Bonner, A new type of neutron spectrometer, Nuclear Instruments and Methods 9 (1) (1960) 1–12. doi:10.1016/0029-554X(60)90043-4.

[15] E. Tiesinga, P. J. Mohr, D. B. Newell, B. N. Taylor, The 2018 codata recommended values of the fundamental physical constants (web version 8.0), Database developed by J. Baker, M. Douma, and S. Kotochigova, National Institute of Standards and Technology, Gaithersburg, MD (2018).

[16] K. H. Beckurts, K. Wirtz, Neutron Physics, Springer-Verlag, New York, 1964.

[17] B. Singh, Nuclear Data Sheets for A=1, Nuclear Data Sheets 106 (4) (2005) 601–618. doi:10.1016/j.nds.2005.11.004.

[18] J. J. Duderstadt, L. J. Hamilton, Nuclear Reactor Analysis, John Wiley & Sons, Inc., New York, 1976.

[19] K. S. Krane, Introductory Nuclear Physics, John Wiley & Sons, Inc., New Yrok, 1988.

[20] D. Reilly, N. Ensslin, H. Smith, Jr., S. Kreiner, Passive Nondestructive Assay of Nuclear Materials, Tech. Rep. LA-UR-90-732, Los Alamos National Laboratory (1991).

[21] R. Kapsimalis, D. Glasgow, B. Anderson, S. Landsberger, The simultaneous determination of ^{235}U and ^{239}Pu using delayed neutron activation analysis, Journal of Radioanalytical and Nuclear Chemistry 298 (3) (2013) 1721–1726. doi:10.1007/s10967-013-2745-y.

[22] J. E. Swansen, P. R. Collinsworth, M. S. Krick, Shift-register coincidence electronics system for thermal neutron counters, Nuclear Instruments and Methods 176 (3) (1980) 555–565. doi:10.1016/0029-554X(80)90386-9.

[23] S. Croft, A. Favalli, G. A. Fugate, I. Gauld, R. D. McElroy, A. Simone, M. T. Swinhoe, R. Venkataraman, The specific (α, n) production rate for ^{234}U in UF_6, Nuclear Instruments and Methods in Physics Research Section A: Accelerators, Spectrometers, Detectors and Associated Equipmentdoi:10.1016/j.nima.2018.11.067.

[24] D. Shahbazi-Gahrouei, M. Gholami, S. Setayandeh, A review on natural background radiation, Advanced Biomedical Research 2 (1) (2013) 65. doi:10.4103/2277-9175.115821.

[25] T. K. Gaisser, R. Engel, E. Resconi, Cosmic rays, in: Cosmic Rays and Particle Physics, Cambridge University Press, Cambridge, 2016, pp. 1–11. doi:10.1017/CBO9781139192194.003.

[26] G. F. Knoll, Radiation Detection and Measurement, 4th Edition, John Wiley & Sons, New York, 2010.

[27] X-5 Monte Carlo Team, MCNP - A General N-Particle Transport Code, Version 5 Volume I: Overview and Theory, Tech. Rep. LA-UR-03-1987, Los Alamos National Laboratory (2003).

[28] C. J. Werner, J. S. Bull, C. J. Solomon, F. B. Brown, G. W. Mckinney, M. E. Rising, D. A. Dixon, R. L. Martz, H. G. Hughes, L. J. Cox, A. J. Zukaitis, J. C. Armstrong, R. A. Forster, L. Casswell, MCNP 6.2 Release Notes, Tech. Rep. LA-UR-18-20808, Los Alamos National Laboratory (2018).

[29] A. Sood, The Monte Carlo Method and MCNP - A Brief Review of Our 40 Year History, in: International Topical Meeting on Industrial Radiation and Radioisotope Measurement Applications Conference, no. LA-UR-17-26533, 2017.

[30] J. C. Wagner, J. E. Sisolak, G. W. McKinney, MCNP: Criticality Safety Benchmark Problems, Tech. Rep. LA-12415, Los Alamos National Laboratory.

[31] A. Sood, R. A. Forster, D. K. Parsons, Analytical Benchmark Test Set for Criticality Code Verification, Tech. Rep. LA-13511, Los Alamos National Laboratory (1999).

[32] D. J. Whalen, D. A. Cardon, J. L. Uhle, J. S. Hendricks, MCNP: Neutron Benchmark Problems, Tech. Rep. LA-12212, Los Alamos National Laboratory (1991).

[33] S. C. Frankle, A Suite of Criticality Benchmarks for Validating Nuclear Data, Tech. Rep. LA-13594, Los Alamos National Laboratory (1999).

[34] S. C. Frankle, Criticality Benchmark Results Using Various MCNP Data Libraries, Tech. Rep. LA-13627, Los Alamos National Laboratory (1999).

[35] M. E. Abhold, M. C. Baker, MCNP-REN: a Monte Carlo tool for neutron detector design, Nuclear Instruments and Methods in Physics Research Section A: Accelerators, Spectrometers, Detectors and Associated Equipment 485 (2002) 576–584.

[36] I. Levi, A. C. Trahan, K. Ben-Meir, O. Ozeri, A. Krakovich, A. Pesach, O. Rivin, C. D. Rael, M. T. Swinhoe, H. O. Menlove, N. Hazenshprung, J. B. Marlow, I. Neder, Nondestructive measurements of residual ^{235}U mass of Israeli Research Reactor-1 fuel using the Advanced Experimental Fuel Counter, Nuclear Instruments and Methods in Physics Research Section A: Accelerators, Spectrometers, Detectors and Associated Equipment 964 (2020) 163797. doi:10.1016/j.nima.2020.163797.

[37] J. P. Joshi, Comparison of ^{252}Cf time correlated induced fission with AmLi induced fission on fresh MTR research reactor fuel, Thesis, Missouri University of Science and Technology (2017).

[38] W. Wilson, R. Perry, W. Charlton, T. Parish, G. Estes, T. Brown, E. Arthur, M. Bozoian, T. England, D. Madland, J. Stewart, SOURCES 4A: A Code for Calculating (α, n), Spontaneous Fission, and Delayed Neutron Sources and Spectra, Tech. Rep. LA-13639-MS, Los Alamos National Laboratory (1999).

[39] E. F. Shores, Plutonium oxide benchmark problems for the SOURCES code, Applied Radiation and Isotopes 62 (5) (2005) 699–704. doi:10.1016/j.apradiso.2004.12.002.

[40] A. V. Alevra, D. J. Thomas, Neutron spectrometry in mixed fields: multisphere spectrometers, Radiation Protection Dosimetry 107 (1-3) (2003) 37–72.

[41] D. Thomas, A. Alevra, Bonner sphere spectrometers–a critical review, Nuclear Instruments and Methods in Physics Research Section A: Accelerators, Spectrometers, Detectors and Associated Equipment 476 (1-2) (2002) 12–20. doi:10.1016/S0168-9002(01)01379-1.

[42] G. J. H. Jacobs, R. L. P. van den Bosch, Calibration measurements with the multisphere method and neutron spectrum analyses using the SAND-II program, Nuclear Instruments and Methods 175 (1980) 483–489.

[43] N. E. Hertel, J. W. Davidson, The response of Bonner spheres to neutrons from thermal energies to 17.3 MeV, Nuclear Instruments and Methods in Physics Research Section A: Accelerators, Spectrometers, Detectors and Associated Equipment 238 (1985) 509–516.

[44] A. V. Alevra, M. Cosack, J. B. Hunt, D. J. Thomas, H. Schraube, Experimental determination of the response of four Bonner sphere sets to monoenergetic neutrons (II), Radiation Protection Dosimetry 40 (2) (1992) 91–102.

[45] J. Liu, F. Hajnal, C. Sims, J. Kuiper, Neutron Spectral Measurements at ORNL, Radiation Protection Dosimetry 30 (3) (1990) 169–178. doi:10.1093/oxfordjournals.rpd.a080615.

[46] W. F. Harvey, F. Hajnal, Multisphere Neutron Spectroscopy Measurements at the Los Alamos National Laboratory Plutonium Facility, Radiation Protection Dosimetry 50 (1) (1993) 13–30. doi:10.1093/oxfordjournals.rpd.a082060.

[47] P. Thomas, K. Harrison, M. Scott, A multisphere neutron spectrometer using a central ^{3}He detector, Nuclear Instruments and Methods in Physics Research 224 (1-2) (1984) 225–232. doi:10.1016/0167-5087(84)90471-X.

[48] A. Alevra, M. Cosack, J. Hunt, D. Thomas, H. Schraube, Experimental Determination of the Response of Four Bonner Sphere sets to Monoenergetic Neutrons, Radiation Protection Dosimetry 23 (1-4) (1988) 293–296. doi:10.1093/oxfordjournals.rpd.a080181.

[49] D. Thomas, A. Alevra, J. Hunt, H. Schraube, Experimental Determination of the Response of Four Bonner Sphere Sets to Thermal Neutrons, Radiation Protection Dosimetry 54 (1) (1994) 25–31. doi:10.1093/oxfordjournals.rpd.a082312.

[50] H. Schuhmacher, H. J. Brede, V. Dangendorf, M. Kuhfuss, J. P. Meulders, W. D. Newhauser, R. Nolte, Quasi-monoenergetic neutron beams with energies from

25-70 MeV, Nuclear Instruments and Methods in Physics Research Section A: Accelerators, Spectrometers, Detectors and Associated Equipment 421 (1999) 284–295.

[51] W. W. Engle, User manual for ANISN, a one dimensional discrete ordinates transport code with anisotropic scattering, AEC Research and Development Report K 1693 (available from RSIC, NEA Data Bank, etc. Package code CCC-254) (1967).

[52] G. Hehn, M. Schweizer, K. Haas, New calculations of neutron response functions of Bonner spheres with helium-3 detectors, Kerntechnik 57 (1992) 251–254.

[53] V. Mares, G. Schraube, H. Schraube, Calculated neutron response of a Bonner sphere spectrometer with ^{3}He counter, Nuclear Instruments and Methods in Physics Research Section A: Accelerators, Spectrometers, Detectors and Associated Equipment 307 (1991) 398–412.

[54] B. Wiegel, A. V. Alevra, B. R. L. Siebert, Calculations of the response functions of Bonner spheres with a spherical ^{3}He proportional counter using realistic detector model, Tech. Rep. Report PTB-N-21, Physikalisch-Technische Bundesanstalt (1994).

[55] M. Kralik, A. Aroua, M. Grecescu, V. Mares, T. Novotny, H. Schraube, B. Wiegel, Specification of Bonner Sphere Systems for Neutron Spectrometry, Radiation Protection Dosimetry 70 (1-4) (1997) 279–284.

[56] V. Lacoste, V. Gressier, J.-L. Pochat, F. Fernandez, M. Bakali, T. Bouassoule, Characterization of Bonner sphere systems at monoenergetic and thermal neutron fields, Radiation Protection Dosimetry 110 (1-4) (2004) 529–532.

[57] W. Rühm, V. Mares, C. Pioch, S. Agosteo, A. Endo, M. Ferrarini, I. Rakhno, S. Rollet, D. Satoh, H. Vincke, Comparison of Bonner sphere responses calculated by different Monte Carlo codes at energies between 1 MeV and 1 GeV–Potential impact on neutron dosimetry at energies higher than 20 MeV, Radiation Measurements 67 (2014) 24–34.

[58] Z. M. Hu, Y. H. Zheng, T. S. Fan, Z. Q. Cui, J. Chen, H. Zhang, G. Gorini, Q. Zhao, Experimental evaluation of the Geant4-calculated response functions of a Bonner sphere spectrometer on monoenergetic neutron sources, Nuclear Instruments and Methods in Physics Research Section A: Accelerators, Spectrometers, Detectors and Associated Equipment 965 (2020) 163836. doi:10.1016/j.nima.2020.163836.

[59] P. J. Griffin, J. G. Kelly, J. W. VanDenBurg, User's manual for SNL-SAND-II Code, Tech. Rep. SAND93-3957, Sandia National Laboratory (1994).

[60] M. Reginatto, The "Few-Channel" Unfolding Programs in the UMG Package: MXD_FC33, GRV_FC33 and IQU_FC333, Tech. rep., Physikalisch-Technische Bundesanstalt (PTB), Braunschweig, Germany (2004).

[61] M. Reginatto, P. Goldhagen, MAXED, a computer code for the deconvolution of multisphere neutron spectrometer data using the maximum entropy method, Tech. Rep. EML-595, Dept. of Energy, Environmental Measurements Lab, New York, NY (1998).

[62] D. W. Freeman, D. R. Edwards, A. E. Bolon, Genetic algorithms – A new technique for solving the neutron spectrum unfolding problem, Nuclear Instruments and Methods in Physics Research Section A: Accelerators, Spectrometers, Detectors and Associated Equipment 425 (3) (1999) 549–576.

[63] B. Mukherjee, BONDI-97: A novel neutron energy spectrum unfolding tool using a genetic algorithm, Nuclear Instruments and Methods in Physics Research Section A: Accelerators, Spectrometers, Detectors and Associated Equipment 432 (2-3) (1999) 305–312.

[64] J. M. Ortiz-Rodriguez, A. Reyes Alfaro, A. Reyes-Haro, J. M. Cervantes Viramontes, H. R. Vega-Carillo, A neutron spectrum unfolding computer code based on artificial neural networks, Radiation Physics and Chemistry 95 (2014) 428–431. doi:10.1016/j.radphyschem.2013.05.007.

[65] J. Wang, Y. Zhou, Z. Guo, L. Haifeng, Neutron spectrum unfolding using three artificial intelligence optimization methods, Applied Radiation and Isotopes 147 (2019) 136–143.

[66] M. Reginatto, P. Goldhagen, S. Neumann, Spectrum unfolding, sensitivity analysis and propagation of uncertainties with the maximum entropy deconvolution code MAXED, Nuclear Instruments and Methods in Physics Research Section A: Accelerators, Spectrometers, Detectors and Associated Equipment 476 (2002) 242–246.

[67] F. G. Perey, Least Squares Dosimetry Unfolding: The Program STAY'SL, Tech. Rep. ORNL/TM-6062, Oak Ridge National Laboratory (1977).

[68] R. Bedogni, C. Domingo, A. Esposito, F. Fernandez, FRUIT: An operational tool for multisphere neutron spectrometry in workplaces, Nuclear Instruments and Methods in Physics Research Section A: Accelerators, Spectrometers, Detectors and Associated Equipment 580 (2007) 1301–1309. doi:10.1016/j.nima.2007.07.033.

[69] W. L. Goffe, G. D. Ferrier, J. Rogers, Global optimization of statistical functions with simulated annealing, Econometrics 60 (1-2) (1994) 65–99.

[70] D. R. Weaver, J. G. Owen, J. Walker, The neutron spectrum from a 5 Ci Am/Li neutron source, Nuclear Instruments and Methods 198 (1982) 599–602.

[71] M. M. Watson, R. Venkataraman, S. Croft, Characterization of ^{252}Cf Sources Using High-Resolution Gamma Spectroscopy, Applied Radiation and Isotopes 169 (2021) 109531. doi:doi.org/10.1016/j.apradiso.2020.109531.

[72] N. Ensslin, W. C. Harker, M. S. Krick, D. G. Langner, M. M. Pickrell, J. E. Stewart, Application Guide to Neutron Multiplicity Counting, Tech. Rep. LA-13422-M, Los Alamos National Laboratory (1998).

[73] M. J. Martin, Nuclear Data Sheets for A=248, Nuclear Data Sheets 122 (2014) 377–409.

[74] N. Roberts, L. Jones, The content of ^{250}Cf and ^{248}Cm in ^{252}Cf neutron sources and the effect on the neutron emission rate, Radiation Protection Dosimetry 126 (1-4) (2007) 83–88. doi:10.1093/rpd/ncm017.

[75] E. Browne, J. K. Tuli, Nuclear Data Sheets for A=246, Nuclear Data Sheets 112 (7) (2011) 1833–1873.

[76] C. D. Nesaraja, Nuclear Data Sheets for A=244, Nuclear Data Sheets2 146 (2017) 387–510. doi:10.1016/j.nds.2017.11.002.

[77] S. Croft, D. Henzlova, Determining ^{252}Cf source strength by absolute passive neutron correlation counting, Nuclear Instruments and Methods in Physics Research Section A: Accelerators, Spectrometers, Detectors and Associated Equipment 714 (2013) 5–12. doi:10.1016/j.nima.2013.02.002.

[78] D. Henzlova, A. Favalli, S. Croft, In-depth evaluation of ^{252}Cf absolute calibration by passive neutron correlation counting method, Metrologia 56 (1) (2019) 015017. doi:10.1088/1681-7575/aaf5a4.

[79] H. O. Menlove, Description and Operation Manual for the Active Well Coincidence Counter, Tech. Rep. LA-7823-M, Los Alamos Scientific Laboratory, Los Alamos, New Mexico (1979).

[80] R. J. Gehrke, R. Aryaeinejad, J. K. Hartwell, W. Y. Yoon, E. Reber, J. R. Davidson, The gamma-ray spectrum of ^{252}Cf and the information contained within it, Nuclear Instruments and Methods in Physics Research, Section B: Beam Interactions with Materials and Atoms 213 (2004) 10–21. doi:10.1016/S0168-583X(03)01526-X.

[81] A. Apostol, J. Zsigrai, J. Bagi, M. Brandis, J. Nikolov, K. Mayer, Characterization of californium sources by gamma spectrometry: relevance for nuclear forensics, Journal of Radioanalytical and Nuclear Chemistry 321 (2019) 405–412. doi:10.1007/s10967-019-06628-0.

[82] E. Browne, J. K. Tuli, Nuclear Data Sheets for A=137, Nuclear Data Sheets 108 (10) (2007) 2173–2318. doi:10.1016/j.nds.2007.09.002.

[83] H. Bateman, The solution of a system of differential equations occurring in the theory of radioactive transformations, in: Proceedings of the Cambridge Philosophical Society, Mathematical and physical sciences, 1910, pp. 423–427.

[84] R. H. Pehl, N. W. Madden, J. H. Elliott, T. W. Raudorf, R. C. Trammell, L. S. Darken, Radiation Damage Resistance of Reverse Electrode GE Coaxial Detectors, IEEE Transactions on Nuclear Science 26 (1) (1979) 321–323. doi:10.1109/TNS.1979.4329652.

[85] Los Alamos National Laboratory, PeakEasy 4.98.1, Computer software (2018).

[86] Mirion Technologies (Canberra), Inc., Genie 2000 Spectroscopy Software (V3.4.1), Computer software (2016).

[87] C. J. Orth, The Average Number of Neutrons Emitted in the Spontaneous Fission of Some Even-Even Heavy Nuclides, Nuclear Science and Engineering 43 (1) (1971) 54–57. doi:10.13182/NSE71-A21245.

[88] Y. Khazov, A. Rodionov, S. Sakharov, B. Singh, Nuclear Data Sheets for A=132, Nuclear Data Sheets 104 (3) (2005) 497–790. doi:10.1016/J.NDS.2005.03.001.

[89] A. Sonzogni, Nuclear Data Sheets for A=136, Nuclear Data Sheets 95 (4) (2002) 837–994. doi:10.1006/ndsh.2002.0008.

[90] J. Chen, Nuclear Data Sheets for A=138, Nuclear Data Sheets 146 (2017) 1–386. doi:10.1016/j.nds.2017.11.001.

[91] N. Nica, Nuclear Data Sheets for A=140, Nuclear Data Sheets 108 (7) (2007) 1287–1582. doi:10.1016/j.nds.2007.06.001.

[92] P. R. Bevington, D. K. Robinson, Data Reduction and Error Analysis for the Physical Sciences, 3rd Edition, McGraw Hill Education, New York, NY, 2002.

[93] J. Ezhold, personal communication (2018).

[94] G. Savard, A. Levand, B. Zabransky, The CARIBU gas catcher, Nuclear Instruments and Methods in Physics Research Section B: Beam Interactions with Materials and Atoms 376 (2016) 246–250. doi:10.1016/j.nimb.2016.02.050.

[95] J. Dubeau, S. S. Hakmana Witharana, J. Atanackovic, A. Yonkeu, J. P. Archambault, A neutron spectrometer using nested moderators, Radiation Protection Dosimetry 150 (2) (2012) 217–222. doi:10.1093/rpd/ncr381.

[96] J. Sommers, M. Jimenez, M. Adamic, J. Giglio, K. Carney, Characterization of a sealed Americium–Beryllium (AmBe) source by inductively coupled plasma mass spectrometry, Journal of Radioanalytical and Nuclear Chemistry 282 (3) (2009) 929–932. doi:10.1007/s10967-009-0189-1.

[97] A. Didi, A. Dadouch, O. Jaï, J. Tajmouati, H. El Bekkouri, Neutron activation analysis: Modelling studies to improve the neutron flux of Americium–Beryllium source, Nuclear Engineering and Technology 49 (4) (2017) 787–791. doi:10.1016/j.net.2017.02.002.

[98] H. R. Trellue, R. C. Little, M. C. White, R. E. MacFarlane, A. C. Kahler, ENDF70: A Continuous-Energy MCNP Neutron Data Library Based on ENDF/B-VII.0, Nuclear Technology 168 (3) (2009) 832–836. doi:10.13182/NT09-2.

[99] A. Ravazzani, R. Jaime, M. Looman, B. Pedersen, P. Peerani, P. Schillebeeckx, M. Thornton, V. Foglio Para, V. Maiorov, Characterization of Neutron Sources by NDA, in: Proceedings of 23rd Annual Symposium on Safeguards and Nuclear Material Management, Brugues, Belgium, 2001.

[100] M. M. Watson, R. Venkataraman, S. Croft, A. Favalli, R. D. McElroy, T. A. DeVol, Unfolding Neutron Energy Spectra Using the Inverse Bonner Sphere Concept, In preparation to Nuclear Instruments and Methods in Physics Research Section A: Accelerators, Spectrometers, Detectors and Associated Equipment.

[101] B. Harker, M. Krick, INCC Software Users Manual, Tech. Rep. LA-UR-99-1291, Los Alamos National Laboratory (1998).

[102] W. Charlton, R. Perry, W. Wilson, Benchmarking of the Los Alamos neutron production rate code SOURCES-3A, Nuclear Instruments and Methods in Physics Research Section B: Beam Interactions with Materials and Atoms 140 (1-2) (1998) 1–8. doi:10.1016/S0168-583X(98)00012-3.